Advances in OptoElectronics

Progress in Domain-Engineered Photonics Materials

Guest Editors: Yalin Lu, Hiroshi Murata, and Chang-Qing Xu

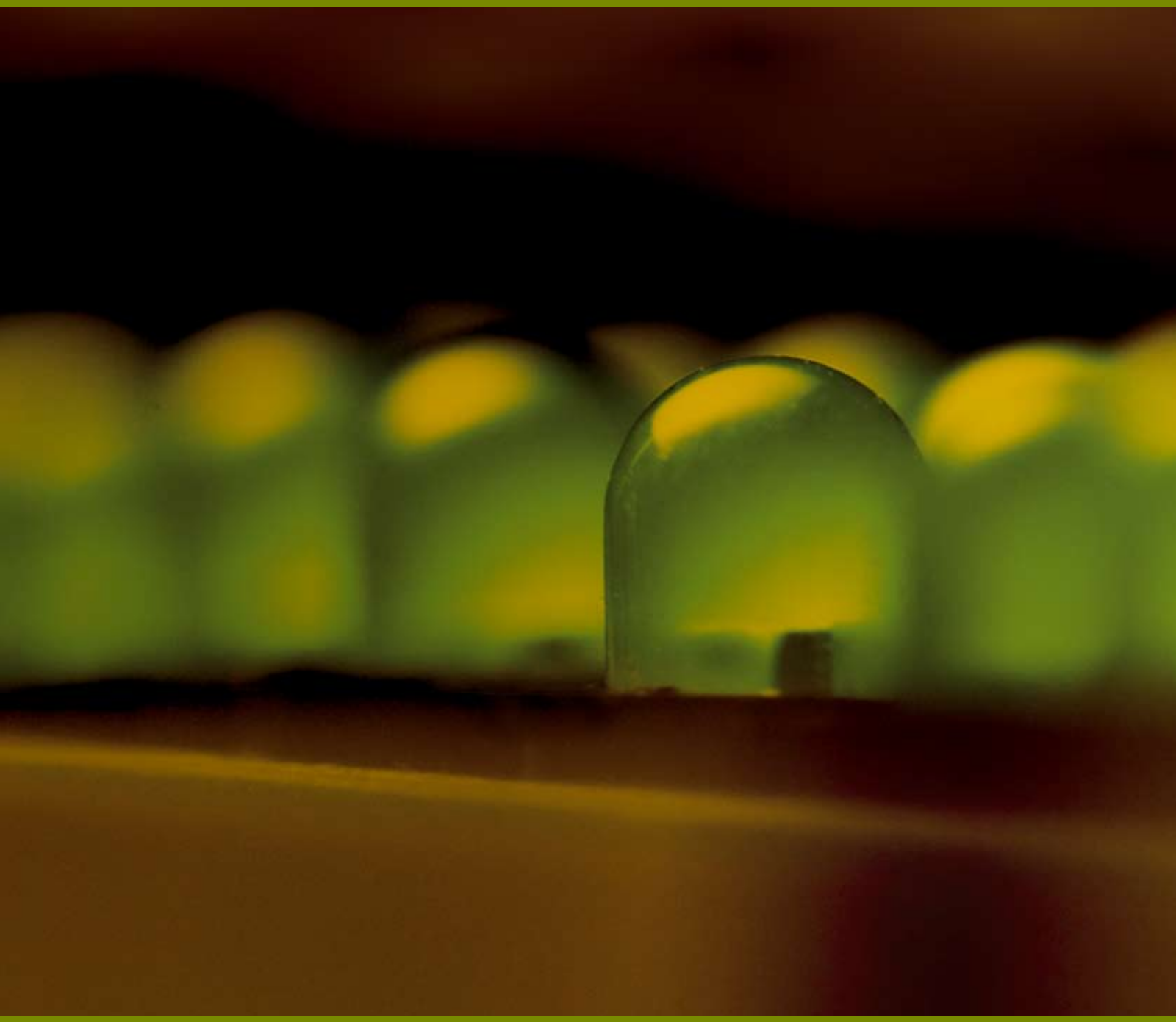

Progress in Domain-Engineered Photonics Materials

Advances in OptoElectronics

Progress in Domain-Engineered Photonics Materials

Guest Editors: Yalin Lu, Hiroshi Murata, and Chang-Qing Xu

Contents

Hindawi Publishing Corporation
Advances in OptoElectronics
Volume 2008, Article ID 467145, 2 pages
doi:10.1155/2008/467145

Editorial

Progress in Domain-Engineered Photonics Materials

Yalin Lu,[1] Hiroshi Murata,[2] and Chang-Qing Xu[3]

[1] *Department of Physics, United States Air Force Academy, Colorado Springs, CO 80840, USA*
[2] *Division of Advanced Electronics and Optical Science, Department of Systems Innovation, Graduate School of Engineering Science, Osaka University, 1-3 Machikaneyama, Toyonaka, Osaka 560-8531, Japan*
[3] *Department of Engineering Physics, McMaster University, Hamilton, ON, Canada L8S 4L7*

Correspondence should be addressed to Yalin Lu, yalin.lu@usafa.edu

Received 9 November 2008; Accepted 9 November 2008

Artificially engineering ferroelectric and ferromagnetic oxide materials' domain structures provide many potential opportunities to explore such materials' extraordinary nonlinear optic, electrooptic (EO), and magnetooptic (MO) effects, to build unique photonic bandgap structures, and to generate phonon-photon-coupled polaritons. Domain engineering can be applied onto such materials, either one-dimensinally or two-dimensionally, can be patterned on the above materials periodically, quasiperiodically, or aperiodically, or can be aligned along different crystalline orientations or by using complicated cascaded structures. Those commonly involved photonic materials can be versatile including ferroelectric-ferromagnetic oxide crystals, semicondcutors, electrooptic polymers, and so on, in either bulk, thin film, or waveguide forms. Implementation of such domain engineering can be very versatile too, and it may follow direct crystal growth, superlattice growth, overgrowth on an already patterned structure, electrical field poling, E-beam writing, and so on. Potential applications of such domain-engineered materials for photonics are very widespread, including nonlinear frequency conversion, EO modulation, optical bistability, acoustics, ultrasonic transducers, terahertz (THz) generation, fiber optics, left-hand materials, and so on.

A remarkable example of past researches in this area is the realization of the quasi-phase-matched (QPM) nonlinear frequency conversions using periodically poled crystals. Recently, development of new photonic and optoelectronic components using such advanced domain-engineered materials, covering a broad range of operation frequencies and having unique optical functions, has become very attractive. However, the effort toward this direction has been crucially relying on the availability of new optical materials, new physical mechanisms, and new device designs. In this special issue focusing on exploring such new aspects, we invited a few papers that address the major issues in the area, summarized some of those recent progresses, and discussed those emerging opportunities of applications.

The first two papers of this special issue are related to the realization of such domain-engineered structures. The first article from M. Fujimura and T. Suhara is the specially invited one, which reports a new formation method for making domain-inverted gratings in MgO:$LiNbO_3$ crystal at room temperature via applying an electric field to the crystal under the irradiation of UV light. The results support the unique way to use a photoconductive cladding layer to suppress the excessive lateral expansion of the domain-inverted regions. The formation process does not require the use of photolithography processing and allows a full room temperature operation. Therefore, it is simple and productive. The second article describes the fabrication of proton-exchanged (PE) waveguides on domain-inverted stoichiometric $LiTaO_3$ (SLT) crystals for guided-wave EO modulation applications. The extraordinary index change in SLT via PE with a coefficient of 0.25×10^{-12} cm^2/s was found to be 0.017, which is comparable to that from the congruent $LiTaO_3$ crystal. Guided-wave EO modulation using such waveguides was also demonstrated.

The following four papers are discussing various issues in a few different nonlinear frequency conversion processes including second harmonic generation (SHG) and difference frequency generation (DFG). Among them is the fifth article by Y. Wong et al. which is also a specially invited one. The third paper by S. Chu et al. reports an ~1W continueous-wave green light generation in a bulk periodically poled

$MgO:LiNbO_3$ crystal, using the intracavity QPM design andexcited by a diode-pumped $Nd:YO_4$ laser. The paper that follows actually describes the SHG in an MgO-doped periodically poled congruent $LiNbO_3$ crystal and pumped by an efficient all-fiber Q-switched Yb-doped fiber laser which delivers high-output power and long-pulse width. The conversion efficiency reaches 4.2% that agrees well with the theoretical simulation. The specially invited article by Y. Wang et al. touches a very unique side in the SHG process by studying the noise characteristics of both harmonic and fundamental waves at relatively higher-power levels, through analyzing their time-domain and frequency-domain characteristics. Understanding the noise characteristics has strong impacts on many applications including coherent detection, spectroscopy, free-space telecommunication, and so on. The fourth paper in this group expands the scope of the interest to detect an optical signal by transferring the signal from the optical frequencies to microwave frequencies via the second-order susceptibility-based DFG process. This frequency-transition method not only offers the potential of a major detection efficiency improvement, but also works well for both intensity-modulated and frequency/phase-modulated optical signals. The study impact to improve the modulation bandwidth in optical fiber telecommunication will be deep.

The seventh and eighth articles in this special issue are directly focusing on EO modulators made from domain-engineered ferroelectric crystals. The seventh paper by H. V. Pham et al. discusses a new method to design traveling-wave EO modulators with fully controlled frequency responses, using nonperiodically domain-reversed structures. Frequency responses of both magnitude and phase of modulation index will be artificially controllable using such new nonperiodical designs. In this paper, several EO modulators for advanced modulation formats such as duobinary modulation and wideband single-sideband modulation are proposed. The eighth article actually discusses the estimation of the phase velocity of a modulation microwave in a quasi-velocity-matched (QVM) EO phase modulator, using the unique EO sampling method that should be very accurate and the most reliable for measuring voltage waveforms on modulator electrodes.

Moving forward from the above discussions on frequency conversion and EO modulation, the last two papers of this special issue actually touch the terahertz (THz) wave generation in a specially designed nonlinear optical fiber, and, even further, the realization of negative optical refraction in a multilayered structure that modulated both tunable dielectric and magnetic behaviors. For avoiding the common absorption problem in current nonlinear optical materials, a multicladding fiber design having a periodically poled $LiNbO_3$ fiber as the maincore was proposed. The generated THz waves via DFG will instantly be coupled to the outer cladding made from those polymeric materials having low absorption over a broad range of THz frequencies, and the optical beam will be maintained inside the main $LiNbO_3$ fiber core. The last article proposes a new theory of realizing negative refraction by frequency-tuning to concurrence of both dielectric layer and the magnetic layer inside a multilayered structure. Negative refractive index will appear after the concurrence frequency. This theory is significant, since the anticipated negative index metamaterials will be flexible in fabrication, and have strong impacts on emerging areas such as superlens, optical cloaking, and sensing.

Yalin Lu
Hiroshi Murata
Chang-Qing Xu

Hindawi Publishing Corporation
Advances in OptoElectronics
Volume 2008, Article ID 421054, 5 pages
doi:10.1155/2008/421054

Research Article

Formation of $MgO:LiNbO_3$ Domain-Inverted Gratings by Voltage Application under UV Light Irradiation at Room Temperature

Masatoshi Fujimura and Toshiaki Suhara

Graduate School of Engineering, Osaka University, 2-1 Yamada-Oka, Suita 565-0871, Japan

Correspondence should be addressed to Masatoshi Fujimura, fujimura@eei.eng.osaka-u.ac.jp

Received 27 February 2008; Accepted 27 May 2008

Recommended by Yalin Lu

$MgO:LiNbO_3$ is an attractive nonlinear-optic crystal for quasiphasematched (QPM) nonlinear-optic devices. This paper reports a new formation method of domain-inverted gratings for QPM in $MgO:LiNbO_3$. Domain inversion of $MgO:LiNbO_3$ by voltage application under UV light was characterized, and reduction of the voltage required for inversion was demonstrated. Results of voltage application under periodic UV light suggested that suppression of excess lateral expansion of the domain inverted regions on $-Z$ surface was crucial for domain-inverted grating formation. Voltage application to a crystal with a photoconductive cladding layer under periodic UV light was proposed. The cladding layer suppressed the expansion, and the domain-inverted gratings with period of 18 μm and area of 25×5 mm^2 were obtained. The formation method does not require the photolithography process and allows the formation by voltage application at room temperature, and therefore, is quite simple and productive.

1. Introduction

There has been a great interest in quasiphasematched (QPM) nonlinear-optic devices for applications in variety of fields including optical memory, optical communication, display, and quantum optics, because they can provide efficient wavelength conversion through the largest nonlinear-optic tensor element at any wavelength in the transparency range [1]. Ferroelectric-domain-inverted grating in nonlinear optic crystals is the mostly used structure to accomplish QPM. Formation technique of the grating by voltage application through periodic electrodes has been established for $LiNbO_3$ crystal [2–4], and a lot of QPM devices have been demonstrated in $LiNbO_3$ [1]. However, applications of the devices may be limited due to the photorefractive damage caused by intense short wavelength optical waves. The devices are often kept at high temperature during the experiments to avoid the damage.

MgO-doped $LiNbO_3$ has large nonlinear-optic coefficients comparable to those of the nondoped $LiNbO_3$ and higher resistance to the photorefractive damage [5], and therefore, it is an attractive nonlinear-optic crystal for QPM devices. Domain-inversion characteristics of $MgO:LiNbO_3$ are quite different from those of the nondoped $LiNbO_3$ [6–8]. Formation of domain-inverted gratings in $MgO:LiNbO_3$ has been studied extensively, and several methods have been reported [9–13]. These methods require photolithography process for fabrication of periodic electrodes and also special treatments for voltage application, such as corona discharge, crystal heating, insulation layer cladding, and/or vacuum environment. Simpler and more productive methods are preferable for practical application.

We recently found reduction of voltage required for $MgO:LiNbO_3$ domain inversion by ultraviolet (UV) light irradiation and showed possibility of grating formation at room temperature by a simple method without photolithography process [14]. The reduction was confirmed also by another research group [15].

In this paper, we report the characteristics of the domain inversion under UV in detail, and demonstrate formation of domain-inverted gratings in $MgO:LiNbO_3$.

2. Reduction of Inversion Voltage by UV Irradiation

We characterized domain inversion of Z-cut MgO(5mol%):$LiNbO_3$ by voltage application under UV light irradiation

using a setup shown in Figure 1. On the $+Z$ face of a $MgO:LiNbO_3$ crystal of 0.5 mm thickness a NESA glass plate was settled, and LiCl aqueous solution filled the gap between the plate and the crystal. The solution served as a liquid electrode. The $-Z$ face was grounded through a liquid electrode and a series capacitor for monitoring the transferred charge. The area of the electrodes was about 4 mm^2. An ultra-high-pressure mercury lamp was used to irradiate the crystal through the NESA. The intensity of the light was ~0.1 W/cm^2 on the NESA. Voltage of a single cycle symmetric triangular waveform was applied to the crystal at room temperature. The amplitude was ~3 kV and the period was 10 seconds. Recording the transferred charge during the voltage application, we obtained a hysteresis loop as shown in Figure 2(a), which implies domain inversion. Voltage application was stopped at point A in Figure 2, and the crystal was etched in $HF:HNO_3$ mixture to visualize the domain structure. Inversion of domain was confirmed. For application of the identical voltage without the UV irradiation, the charge transfer was much smaller, as shown in Figure 2(b), and no domain inversion took place. The results indicated that UV light irradiation reduces the voltage required for domain inversion.

By application of a voltage of −2 kV for 4 seconds to the $-Z$ surface with irradiating the UV light of ~0.1 W/cm^2 intensity from $-Z$ side, domain-inverted region was obtained only on $-Z$ surface. By application of a voltage of +2 kV for 4 seconds to $+Z$ surface with irradiating from $+Z$ side, inverted region was not obtained on $+Z$ surface but on $-Z$ surface. This result suggests that domain inversion nucleates only on $-Z$ face under the UV irradiation. It is quite different from the other methods, where inversion nucleates on $+Z$ face.

The light from the high-pressure mercury lamp consists of many emission lines, and they include the emissions at 289, 313, 334, and 365 nm wavelengths. Each wavelength component was extracted by a wavelength filter, and used for the domain inversion experiments to clarify the wavelength components effective to the reduction of the inversion voltage. The inversion took place for UV irradiation at 289 or 313 nm wavelength, which is in the absorption wavelength range of $MgO:LiNbO_3$ crystal. The mechanism of the UV-assisted domain inversion is not clear yet. It may be related to local field due to migration of free electrons caused by UV light absorption.

3. Domain Inversion by Voltage Application under Periodic UV Light

We considered that voltage application under UV light with spatially periodic intensity modulation would result in formation of $MgO:LiNbO_3$ domain-inverted grating. We made an apparatus for the voltage application at room temperature under periodic UV light. On the $-Z$ surface of a $MgO:LiNbO_3$, a Cr photomask with grating pattern is settled. A UV light from an ultra-high-pressure mercury lamp goes through the photomask, and periodic intensity distribution of UV light is formed in the crystal. LiCl aqueous solution fills the gaps on both surfaces of the crystal. A negative high voltage is applied to the $-Z$ surface at room temperature through the uniform liquid electrode. Domain

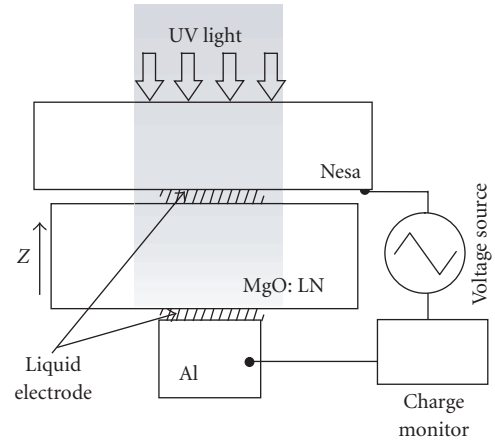

Figure 1: Setup for characterization of domain inversion under UV irradiation.

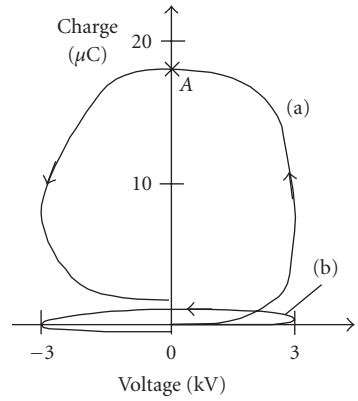

Figure 2: Hysteresis loop of $MgO:LiNbO_3$ crystal at room temperature (a) under UV irradiation and (b) without UV irradiation.

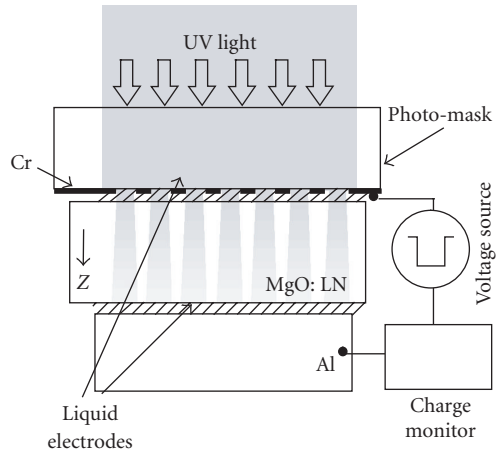

Figure 3: Setup for voltage application under spatially periodic UV light at room temperature.

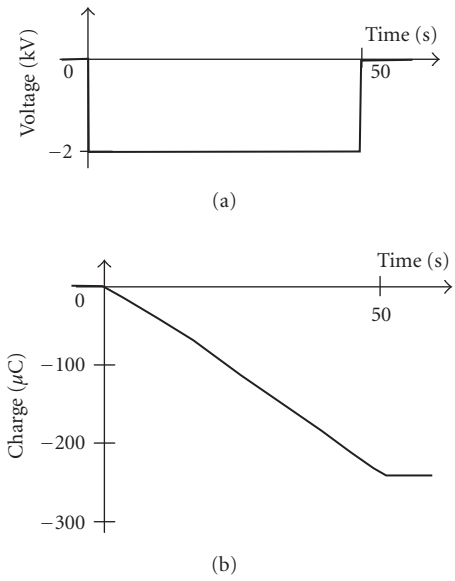

Figure 4: Typical waveforms of the applied voltage and the accumulated inversion charge.

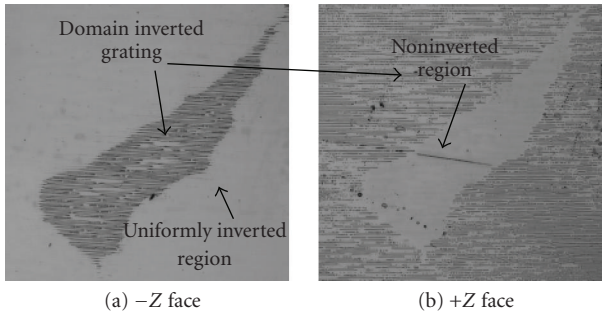

Figure 5: Typical domain structure formed by voltage application under periodic UV irradiation.

inversion takes place in the UV irradiated region, while no inversion takes place in the nonirradiated region. Therefore domain-inverted gratings are formed.

Voltages were applied under UV light of 0.1 W/cm^2 from $-Z$ side, and the resultant domain structures were examined after etching. The crystal thickness was 0.5 mm, and the period of the Cr pattern was 15.4 μm. The applied voltages ranged from -0.2 to -4 kV, and the durations ranged from 10 to 90 seconds. Typical waveforms of the applied voltage and the accumulated inversion charge are shown in Figure 4 for electrode area of 50 mm^2. The charge increased almost proportionally. Typical result is shown in Figure 5. In a part (central part of Figures 5(a) and 5(b)), grating was obtained on $-Z$ face, but inverted region was not obtained on $+Z$ face yet. In the surrounding part, inverted regions had expanded laterally and merged one another on $-Z$ face. Only in such part, inverted regions were obtained on +Z. Nucleation and evolution of domain-inverted regions on the $-Z$ surfaces and on the cross sections in the vicinity of the $-Z$ surfaces were examined and are shown in Figure 6. At first domain-inverted regions nucleated at the $-Z$ surface (Figures 6(a) and 6(b)). The initially-domain-inverted regions expanded for higher and longer voltage application, and a domain-inverted grating was formed on the $-Z$ surface (Figure 6(c)). The inverted region was limited in the vicinity of $-Z$ surface. The depth of the inverted region was a few microns (Figure 6(d)). The regions laterally expanded at the $-Z$ surface and formed a very thin domain-inverted layer (Figures 6(e) and 6(f)). The thickness of the layer was $\sim$0.5 μm. Besides, next the initially-inverted regions started expansion toward $+Z$ surface to form immediately a domain-inverted grating with inverted regions continuing in the whole crystal thickness (Figures 6(g) and 6(h)). Further voltage application resulted in a uniformly inverted structure without grating. The domain inversion took place in the same way under UV irradiation of higher optical intensity up to 2 W/cm^2. Suppression of excess lateral expansion of domain-inverted region on $-Z$ surface is crucial for forming domain-inverted gratings applicable to QPM devices.

4. Formation of Domain-Inverted Gratings

We modified the method to suppress the excess lateral expansion. Voltage pulse was applied to a crystal with photoconductive cladding layer on $-Z$ surface under UV. The application setup was similar to Figure 3 except that a photoconductive layer was deposited on the $-Z$ surface. In the UV-irradiated region, the photoconductive layer serves as a (semi-)conductor, allows charge transfer associated with domain inversion, and therefore, does not prevent domain inversion. On the other hand, in the nonirradiated region, it serves as an insulator and prevents inversion. Therefore, excess lateral expansion of the inverted region can be suppressed, and the grating structure can be maintained on $-Z$ surface until the inverted regions reach $+Z$ surface.

We noticed that a commercially available photoresist (Clariant, AZ-P4620) can be used as a photoconductive material for this purpose. The resistivity of the film was measured. It was initially $\sim 6 \times 10^{15}$ (Ωcm), and dropped down to $\sim 1 \times 10^{12}$ (Ωcm) by irradiation of UV light with intensity of 1 W/cm^2.

The photoresist was spin-coated on $-Z$ surface of MgO:LiNbO$_3$ crystal of 0.5 mm thickness, and voltage pulses were applied under various conditions. The thickness of the photoconductive layer, intensity of the UV light, duration of the voltage application, and the voltage were chosen within ranges of 7–10 μm, 0.05–0.5 W/cm^2, 50–1000 seconds, and 3.3–3.9 kV, respectively. The resultant domain structure was examined after etching. When the thickness was too thin and/or the intensity was too high, suppression of the lateral expansion was not sufficient. When the thickness was too thick and/or the intensity was too low, the width of the inverted region was too narrow. When the duration was too short and/or the voltage was too low, the inverted region did not reach to $+Z$ face. When the duration was too long and/or the voltage was too high, damages took place in the crystal. A domain-inverted grating fabricated for the photoconductive layer thickness of 10 μm, the UV intensity of 0.07 W/cm^2, the duration of 900 seconds, and the voltage of 3.5 kV, are

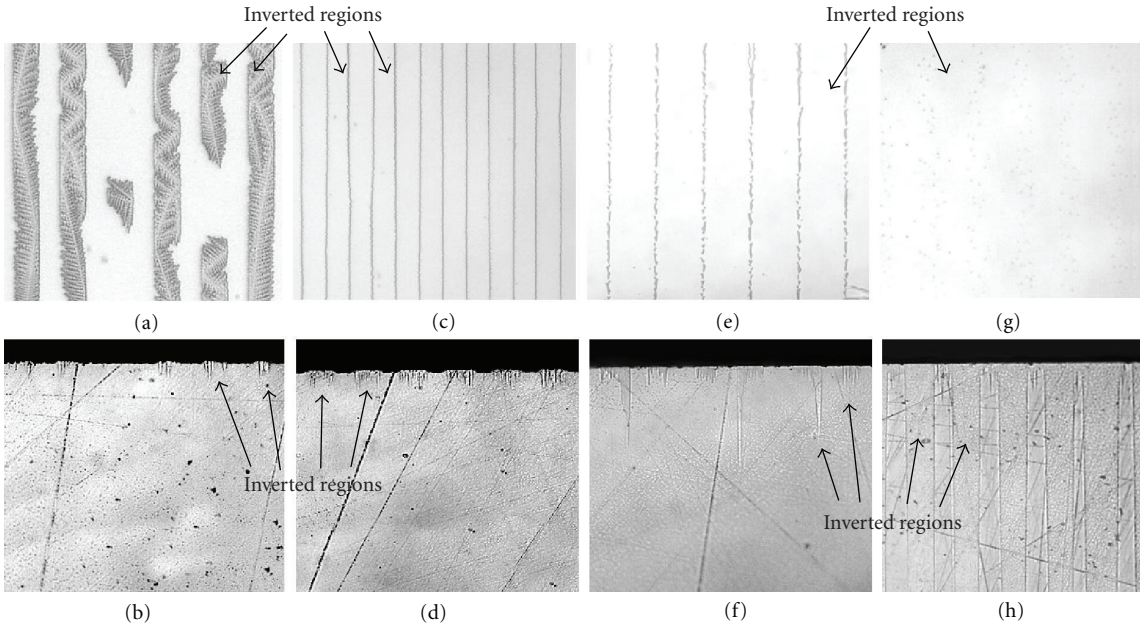

FIGURE 6: Nucleation and evolution of domain-inverted regions (a), (c), (e), (g) on $-Z$ surfaces and (b), (d), (f), (h) in the cross sections. Inverted regions evolved as ((a), (b))→((c), (d)) →((e), (f)) →((g), (h)). The period of the grating pattern was 15.4 μm.

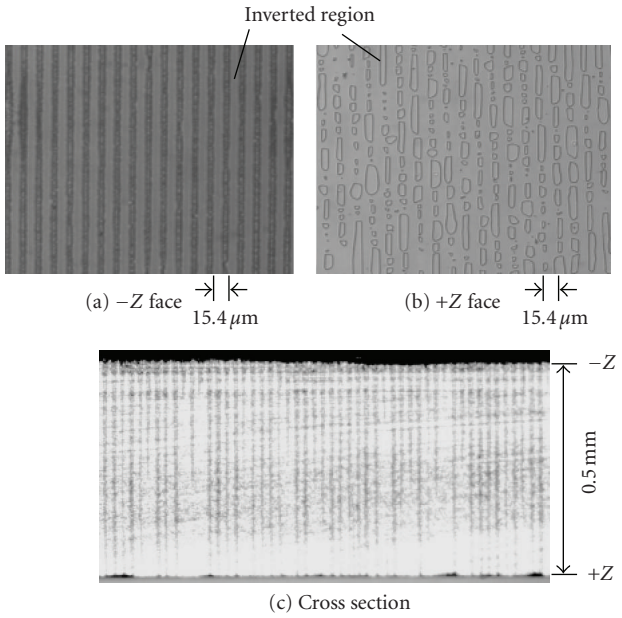

FIGURE 7: Domain-inverted grating formed by voltage application to crystals with photoconductive cladding under UV irradiation.

shown in Figure 7. The grating period was 15.4 μm and the area was $10 \times 5\,\text{mm}^2$. Grating structure was obtained on both $-Z$ face (Figure 7(a)) and $+Z$ face (Figure 7(b)) in the same part. The crystal was cut by a dicing saw and etched again to examine the domain structure on the cross section. The inverted regions continued through the whole crystal thickness (Figure 7(c)). However, there are some points to be improved further. They include that the width of the grating line on $-Z$ was somewhat wide, and that the grating lines on $+Z$ were not continuous lines but segmented lines.

Fabrication of domain-inverted gratings in larger area was carried out. A grating with period of 18 μm and area of $25 \times 5\,\text{mm}^2$ was obtained. In a simple bulk SHG experiment using the crystal, a QPM SH wave was obtained for a pump wavelength at 1549.5 nm. It agrees well with theoretical prediction based on a reported Sellmeier equation [1]. The SHG performance will be characterized in detail and reported elsewhere.

5. Conclusion

Domain inversion of MgO:$LiNbO_3$ by voltage application under UV light was characterized, and reduction of the inversion voltage was shown. Voltage application under UV light with spatial periodic intensity modulation suggested that it was crucial to suppress excess lateral expansion on $-Z$ surface for domain-inverted grating formation. Application of photoconductive cladding layer on the crystal was proposed and successfully suppressed the expansion. Domain-inverted gratings with period of 18 μm and area of $25 \times 5\,\text{mm}^2$ were obtained. The formation method does not require the photo-lithography process and allows voltage application at room temperature; and therefore it is quite simple and productive. Experimental work is being continued for higher-quality grating formation and for application of the gratings to QPM nonlinear-optic devices.

Acknowledgment

This work was supported by Grant-in-aid for Scientific Research from MEXT.

References

[1] T. Suhara and M. Fujimura, *Waveguide Nonlinear-Optic Devices*, Springer, Berlin, Germany, 2003.

[2] M. Yamada, N. Nada, M. Saitoh, and K. Watanabe, "First-order quasi-phase matched $LiNbO_3$ waveguide periodically poled by applying an external field for efficient blue second-harmonic generation," *Applied Physics Letters*, vol. 62, no. 5, pp. 435–436, 1993.

[3] L. E. Myers, R. C. Eckardt, M. M. Fejer, R. L. Byer, W. R. Bosenberg, and J. W. Pierce, "Quasi-phase-matched optical parametric oscillators in bulk periodically poled $LiNbO_3$," *Journal of the Optical Society of America B*, vol. 12, no. 11, pp. 2102–2116, 2005.

[4] K. Kintaka, M. Fujimura, T. Suhara, and H. Nishihara, "High-efficiency $LiNbO_3$ waveguide second-harmonic generation devices with ferroelectric-domain-inverted gratings fabricated by applying voltage," *Journal of Lightwave Technology*, vol. 14, no. 3, pp. 462–468, 1996.

[5] D. A. Bryan, R. Gerson, and H. E. Tomaschke, "Increased optical damage resistance in lithium niobate," *Applied Physics Letters*, vol. 44, no. 9, pp. 847–849, 1984.

[6] S. Sonoda, I. Tsuruma, and M. Hatori, "Second harmonic generation in electric poled *X*-cut MgO-doped $LiNbO_3$ waveguides," *Applied Physics Letters*, vol. 70, no. 23, pp. 3078–3080, 1997.

[7] K. Nakamura, J. Kurz, K. Parameswaran, and M. M. Fejer, "Periodic poling of magnesium-oxide-doped lithium niobate," *Journal of Applied Physics*, vol. 91, no. 7, pp. 4528–4534, 2002.

[8] K. Mizuuchi, A. Morikawa, T. Sugita, and K. Yamamoto, "Polarisation-switching-induced resistance change in ferroelectric Mg-doped $LiNbO_3$ single crystals," *Electronics Letters*, vol. 40, no. 13, pp. 819–820, 2004.

[9] A. Harada and Y. Nihei, "Bulk periodically poled MgO-$LiNbO_3$ by corona discharge method," *Applied Physics Letters*, vol. 69, no. 18, pp. 2629–2631, 1996.

[10] T. Sugita, K. Mizuuchi, Y. Kitaoka, and K. Yamamoto, "31%-efficiency blue second-harmonic generation in a periodically poled MgO:$LiNbO_3$ waveguide by frequency doubling of an AlGaAs laser diode," *Optics Letters*, vol. 24, no. 22, pp. 1590–1592, 1999.

[11] Y. L. Lee, H. Suche, G. Schreiber, R. Ricken, V. Quiring, and W. Sohler, "Periodical domain inversion in singlemode Ti:MgO:$LiNbO_3$ channel waveguides," *Electronics Letters*, vol. 38, no. 15, pp. 812–813, 2002.

[12] H. Ishizuki, T. Taira, S. Kurimura, J. H. Ro, and M. Cha, "Periodic poling in 3-mm-thick MgO:$LiNbO_3$ crystals," *Japanese Journal of Applied Physics*, vol. 42, part 2, no. 2A, pp. L108–L110, 2003.

[13] N. Horikawa, T. Tsubouchi, M. Fujimura, and T. Suhara, "Formation of domain-inverted grating in MgO:$LiNbO_3$ by voltage application with insulation layer cladding," *Japanese Journal of Applied Physics*, vol. 46, part 1, no. 8A, pp. 5178–5180, 2007.

[14] M. Fujimura, T. Sohmura, and T. Suhara, "Fabrication of domain-inverted gratings in MgO:$LiNbO_3$ by applying voltage under ultraviolet irradiation through photomask at room temperature," *Electronics Letters*, vol. 39, no. 9, pp. 719–721, 2003.

[15] M. C. Wengler, B. Fassbender, E. Soergel, and K. Buse, "Impact of ultraviolet light on coercive field, poling dynamics and poling quality of various lithium niobate crystals from different sources," *Journal of Applied Physics*, vol. 96, no. 5, pp. 2816–2820, 2004.

Hindawi Publishing Corporation
Advances in OptoElectronics
Volume 2008, Article ID 654280, 4 pages
doi:10.1155/2008/654280

Research Article

Fabrication of Proton-Exchange Waveguide Using Stoichiometric $LiTaO_3$ for Guided Wave Electrooptic Modulators with Polarization-Reversed Structure

Hiroshi Murata and Yasuyuki Okamura

Graduate School of Engineering Science, Osaka University, 1-3 Machikaneyama, Toyonaka, Osaka 560-8531, Japan

Correspondence should be addressed to Hiroshi Murata, murata@ee.es.osaka-u.ac.jp

Received 2 July 2008; Accepted 2 September 2008

Recommended by Chang-qing Xu

Optical waveguides were fabricated on z-cut stoichiometric $LiTaO_3$ (SLT) by using the proton-exchange method. The surface index change for the extraordinary ray on the SLT substrate resulting from the proton exchange was 0.017, which coincided well with congruent $LiTaO_3$ substrates. The proton exchange coefficient in the SLT was 0.25×10^{-12} cm^2/s. The application of the SLT waveguide to a quasi-velocity-matched travelling-wave electrooptic modulator with periodically polarization-reversed structure is also reported.

1. Introduction

Recently, optical-quality stoichiometric $LiNbO_3$ (SLN) and stoichiometric $LiTaO_3$ (SLT) crystals have been attracting a lot of interest due to their excellent characteristics as a material for optical functional devices; small coercive electric field for polarization reversal, excellent nonlinear optic (NLO) and electrooptic (EO) characteristics, and small defect density [1–5]. Several studies on the optical wavelength conversion devices using NLO effects in SLN and SLT have been reported, however, there are few reports on their applications to EO devices. In particular, a guided-wave optical modulator based on SLT has not been yet reported, as far as we know. One main reason, we believe, is that waveguide fabrication methods have not been established for SLT. SLT exhibits a large tolerance for optical damage and small birefringence which can be controlled precisely. These features are attractive for applications to advanced NLO and EO devices.

In this report, we present the fabrication of proton exchange waveguides in z-cut SLT substrates. The measured surface refractive index change for an extraordinary ray, Δn_e, was $\Delta n_e = 0.017$, which was in good agreement with the reported value in congruent $LiTaO_3$ [6]. The application to high-speed traveling-wave EO modulators using SLT with periodic polarization reversal for quasi-velocity-matching is also reported.

2. Waveguide Fabrication

Z-cut stoichiometric $LiTaO_3$ (SLT) wafers from Oxide Corporation were used in this study. For the fabrication of the proton exchange waveguides, the standard exchange technique using melted benzoic acid was used [6]. The temperature of the melted benzoic acid for the proton exchange was set at 240 degrees centigrade. During the proton exchange process, the temperature of the melted benzoic acid was kept within 240 ± 0.1 degrees centigrade by use of a proportional-integral-derivative (PID) temperature controller. Several slab waveguides were fabricated using SLT with three different proton exchange times set at 4, 9, and 24 hours.

The effective indices of the TM-guided modes in the fabricated slab waveguides were measured by using the prism coupling method with a standard rutile prism coupler at a wavelength of 633 nm. The measured results are plotted in Figure 1 with the dispersion curves of TM-guided modes. Figure 2 shows the relationship between the proton exchange

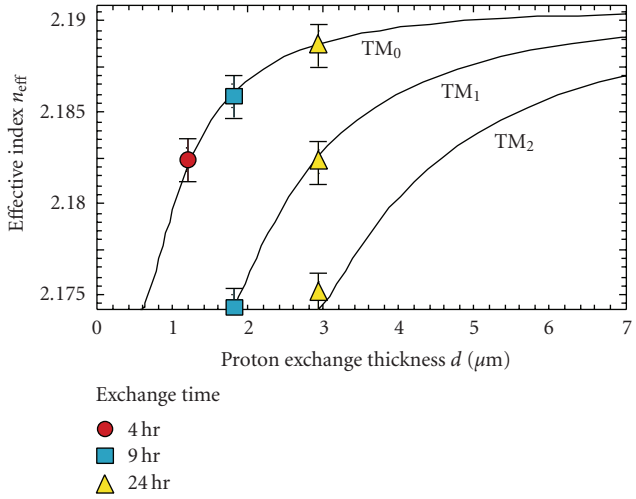

Figure 1: Measured effective index values with TM-guided wave mode dispersion curves.

thickness and the square root of the exchange time. From the measurement results, we obtained the surface index change, Δn_e, for the extraordinary ray and the exchange coefficient, D_{ex}, in the SLT by the proton exchange with benzoic acid at 240 degrees centigrade. We defined the exchange coefficient D_{ex} by use of the depth d of the proton-exchanged layer from the surface and the proton exchange time t_{ex} as the following equation:

$$d = 2\sqrt{D_{ex} t_{ex}}. \quad (1)$$

The obtained results are summarized in Table 1. For comparison, the reported surface index change value and exchange coefficient in CLT [6] are also shown in Table 1. The surface index change value in SLT coincided with the reported one of CLT by the proton exchange with benzoic acid at 249 degrees centigrade [6]. On the other hand, the exchange coefficient in SLT at 240 degrees centigrade was about 30% larger than that in CLT at 249 degrees centigrade. In other words, the velocity of the proton exchange in SLT was slightly faster compared with CLT. This might come from the small defect density of SLT. From the measured surface refractive index change and the depth of the exchanged layer, we can derive the proton exchange condition for SLT in order to obtain a single-mode channel optical waveguide at a designed wavelength.

3. Fabrication of Quasi-Velocity-Matched Electrooptic Modulator

Utilizing the proton exchange single-mode optical waveguide of SLT, we tried to fabricate the quasi-velocity-matched (QVM) electrooptic (EO) modulators with traveling-wave electrodes and periodically polarization-reversed structure [7]. The basic structure of the device is shown in Figure 3. It consists of a single-mode channel waveguide formed by the proton exchange method and traveling-wave coplanar electrodes fabricated on a z-cut SLT substrate with an SiO_2 buffer layer. A periodically polarization-reversed structure is also fabricated through the substrate for the quasi-velocity-matching between the lightwaves propagating in the optical waveguide and the modulation microwave traveling along the coplanar electrodes.

Table 1: The surface refractive index change Δn_e and the exchange coefficient D_{ex} in the proton exchange slab waveguides of SLT and CLT.

	Δn_e	$D_{ex}(10^{-12}$ cm^2/s)
Stoichiometric $LiTaO_3$ (benzoic acid, 240 degrees)	0.017	0.25
Congruent $LiTaO_3$ [6] (benzoic acid, 249 degrees)	0.017	0.184

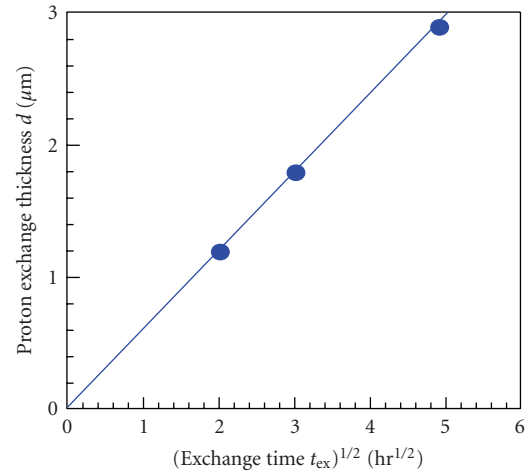

Figure 2: Proton exchange thickness as a function of the square root of exchange time in the measured samples.

In the device design, we set the peak modulation frequency as 15 GHz and the operational light wavelength as 633 nm for the prototype device. The required length for each polarization-reversed and nonreversed region L for the quasi-velocity-matching is given by the following equation [7]:

$$L = \frac{c}{2f_m (n_m - n_g)}, \quad (2)$$

where n_g is the group index of the lightwaves propagating in the waveguide, n_m is the effective index of the modulation microwave traveling along the electrodes, and c is the lightwave velocity in vacuum. In order to obtain a single-mode channel waveguide at 633 nm, we designed the waveguide core width as 3 μm and the waveguide core depth as 0.7 μm. From the reported wavelength dispersion characteristics of the refractive index of SLT [4] and calculated waveguide dispersion characteristics, we obtained the group index value of the lightwaves propagating in the waveguide as $n_g = 2.30$ at a wavelength of 633 nm. The effective index of the modulation microwave was also calculated as $n_m = 4.55$ from the dielectric constants of SLT and the structure of the coplanar asymmetric electrodes with a hot electrode of 14 μm in width and an electrode separation of 33 μm. As a result,

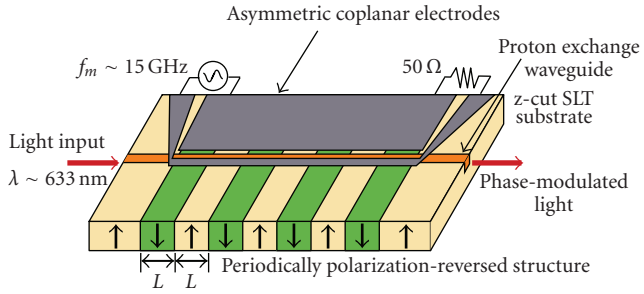

FIGURE 3: Structure of QVM EO modulator with periodically polarization-reversed structure.

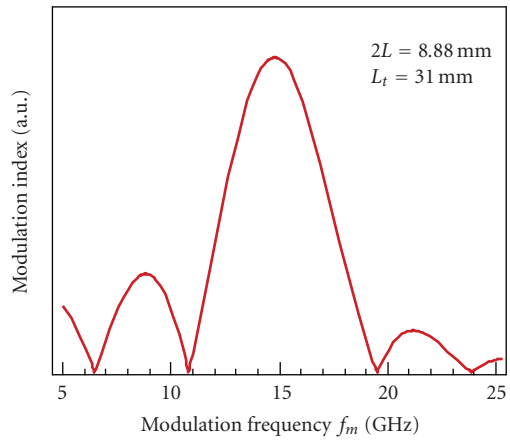

FIGURE 4: Calculated modulation frequency dependence of the QVM modulator when the polarization reversal period is $2L = 8.88$ mm and the total electrode length is $L_t = 31$ mm.

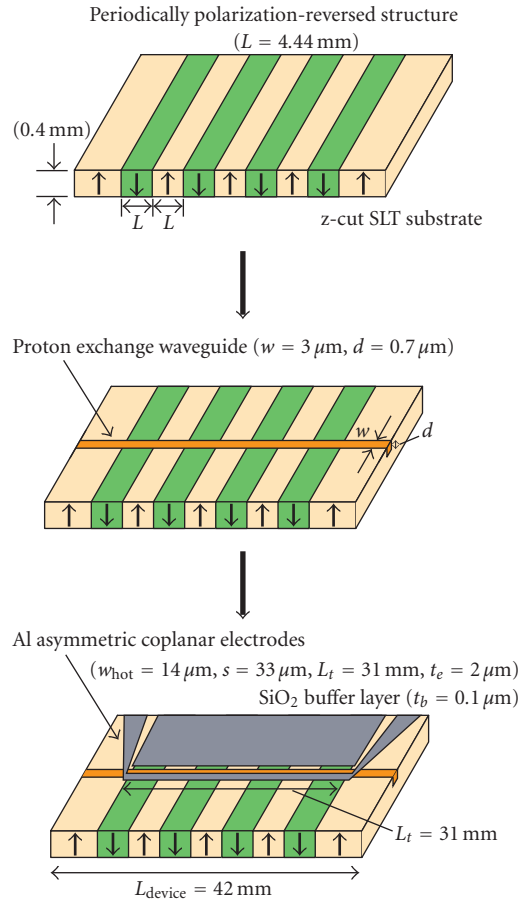

FIGURE 5: Fabrication sequence of the QVM EO modulator.

the length for the polarization-reversed and nonreversed region for the quasi-velocity-matching was obtained as $L = 4.44$ mm for the peak modulation frequency at 15 GHz from (2). The calculated frequency response of the QVM modulator is shown in Figure 4 when the electrode length for modulation L_t is set as 7 times that of L ($L_t = 31$ mm).

The designed device was fabricated using z-cut SLT as shown in Figure 5. Firstly, the periodic polarization reversal pattern with a period of $2L = 8.88$ mm was fabricated on a 0.4 mm thick z-cut SLT substrate by use of the pulse voltage applying method. The electric field required for the polarization reversal was rather small (~3.3 kV/mm) compared with standard CLT substrates (~22 kV/mm). Next, the single-mode channel waveguide was fabricated on the periodically poled SLT by using the proton exchange method. The waveguide core width was 3 μm and the core depth was set as 0.7 μm. The periodically-poled Cr-masked SLT substrate for the fabrication of the channel waveguide with a width of 3 μm was immersed into the melted benzoic acid at 240 degree centigrade for 90 minutes. After the removal of the Cr film, a 0.1 μm thick SiO_2 buffer layer was deposited on the waveguide by sputtering. Finally, 2 μm thick Al asymmetric coplanar electrodes were fabricated onto the waveguide by use of EB deposition and a standard photolithography technique. The hot electrode width was set as 14 μm and the electrodes separation was set as 33 μm, where the intrinsic impedance of the electrodes became 50 Ω. The electrode length for modulation L_t was 31 mm, which corresponded with 3.5 times the polarization reversal period $2L$.

Both ends of the waveguides were cut and polished for light-beam coupling. The total device length was 42 mm and the optical insertion loss of the device was about 25 dB including the coupling losses at both ends. We believe that the relatively large optical loss will be reduced by a thermal annealing process as with the proton exchange CLT waveguides (annealed proton exchange process). Microwave characteristics of the fabricated electrodes were measured by use of a network analyzer and good microwave responses of SLT (almost the same as CLT) were confirmed.

The optical spectrum of the modulated lightwave from the fabricated device was measured by use of a scanning Fabry-Perot interferometer. The measured modulation frequency dependence of the fabricated QVM EO modulator is shown in Figure 6. The band modulation characteristic was confirmed. The peak modulation frequency was in good agreement with the designed frequency of 15 GHz. We think that the dip in the modulation index at 14 GHz in Figure 5

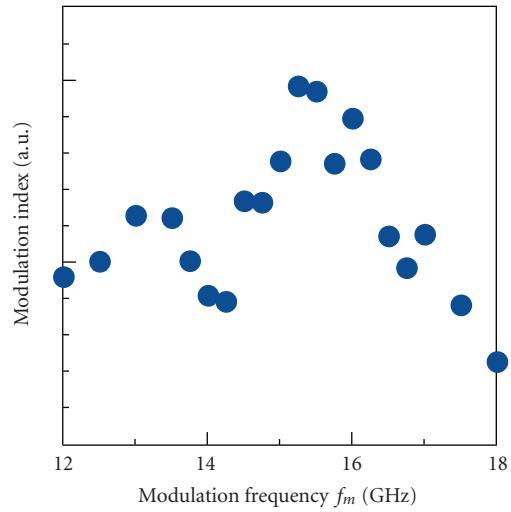

Figure 6: Measured modulation frequency dependence of the fabricated modulator.

was due to the effect of the substrate resonance mode, which could be reduced by changing the size of the substrate and the coupling of the microwave signal to the electrodes.

4. Discussion and Conclusion

Basic characteristics of the proton exchange waveguide in SLT and the fabrication condition of a single-mode waveguide were obtained. However, the optical loss in the fabricated waveguide was large (~25 dB in the 42 mm waveguide with coupling loss). In addition, it is well known that the proton exchange process might degrade the Pockels effect. Thermal annealing is rather effective in reducing the optical loss and recovering the Pockels effect. We have also tried to do the thermal annealing of the fabricated proton exchange SLT waveguides with the standard annealing condition for the proton exchange CLT waveguides (250~400 degrees centigrade, ~1 hour). However, after annealing, the guiding characteristics became poor and the output beam spot from the end of the waveguide could not be oberved. It might come from the large diffusion velocity, and some specific techniques like rapid thermal annealing might be necessary to realize good annealing conditions.

In conclusion, we fabricated the proton-exchanged waveguide on z-cut stoichiometric SLT. The measured surface index change for the extraordinary ray was $\Delta n_e = 0.017$, which coincided well with congruent $LiTaO_3$ substrates. The proton exchange coefficient in SLT was $D_{ex} = 0.25 \times 10^{-12}$ cm^2/s. Some interesting applications include EO modulators with advanced functions using the polarization reversal and optical waveguide technologies.

Acknowledgments

The authors thank Dr. Atsushi Ishikawa for his help with the experiments. This work was supported in part by the Grants-in-Aid for Scientific Research from the Ministry of Education, Science, Sports, and Culture, Japan .

References

[1] T. Fujiwara, M. Takahashi, M. Ohama, A. J. Ikushima, Y. Furukawa, and K. Kitamura, "Comparison of electro-optic effect between stoichiometric and congruent $LiNbO_3$," *Electronics Letters*, vol. 35, no. 6, pp. 499–501, 1999.

[2] T. Hatanaka, K. Nakamura, T. Taniuchi, H. Ito, Y. Furukawa, and K. Kitamura, "Quasi-phase-matched optical parametric oscillation with periodically poled stoichiometric $LiTaO_3$," *Optics Letters*, vol. 25, no. 9, pp. 651–653, 2000.

[3] M. Nakamura, S. Higuchi, S. Takekawa, K. Terabe, Y. Furukawa, and K. Kitamura, "Optical damage resistance and refractive indices in near-stoichiometric MgO-doped $LiNbO_3$," *Japanese Journal of Applied Physics*, vol. 41, part 2, no. 1A/B, pp. L49–L51, 2002.

[4] M. Nakamura, S. Higuchi, S. Takekawa, K. Terabe, Y. Furukawa, and K. Kitamura, "Refractive indices in undoped and MgO-doped near-stoichiometric $LiTaO_3$ crystals," *Japanese Journal of Applied Physics*, vol. 41, part 2, no. 4B, pp. L465–L467, 2002.

[5] W. B. Cho, K. Kim, H. Lim, J. Lee, S. Kurimura, and F. Rotermund, "Multikilohertz optical parametric chirped pulse amplification in periodically poled stoichiometric $LiTaO_3$ at 1235 nm," *Optics Letters*, vol. 32, no. 19, pp. 2828–2830, 2007.

[6] K. Tada, T. Murai, T. Nakabayashi, T. Iwashima, and T. Ishlkawa, "Fabrication of $LiTaO_3$ optical waveguide by H^+ exchange method," *Japanese Journal of Applied Physics*, vol. 26, part 1, no. 3, pp. 503–504, 1987.

[7] H. Murata, A. Morimoto, T. Kobayashi, and S. Yamamoto, "Optical pulse generation by electrooptic-modulation method and its application to integrated ultrashort pulse generators," *IEEE Journal of Selected Topics in Quantum Electronics*, vol. 6, no. 6, pp. 1325–1331, 2000.

Hindawi Publishing Corporation
Advances in OptoElectronics
Volume 2008, Article ID 151487, 4 pages
doi:10.1155/2008/151487

Research Article

High-Efficiency Intracavity Continuous-Wave Green-Light Generation by Quasiphase Matching in a Bulk Periodically Poled MgO:$LiNbO_3$ Crystal

Shaowei Chu,[1,2] Ying Zhang,[3] Bin Wang,[1] and Yong Bi[1]

[1] *Division of Opto-Electronics System, Academy of Opto-Electronics, Chinese Academy of Sciences, Beijing 100085, China*
[2] *Graduate University of Chinese Academy of Sciences (GUCAS), Beijing 100080, China*
[3] *R&D Department, Phoebus Vision Opto-Electronics Technology Ltd., Beijing 100094, China*

Correspondence should be addressed to Yong Bi, biyong@aoe.ac.cn

Received 29 March 2008; Accepted 18 August 2008

Recommended by Yalin Lu

908 mW of green light at 532 nm were generated by intracavity quasiphase matching in a bulk periodically poled MgO:$LiNbO_3$ (PPMgLN) crystal. A maximum optical-to-optical conversion efficiency of 33.5% was obtained from a 0.5 mm thick, 10 mm long, and 5 mol% MgO:$LiNbO_3$ crystal with an end-pump power of 2.7 W at 808 nm. The temperature bandwidth between the intracavity and single-pass frequency doubling was found to be different for the PPMgLN. Reliability and stability of the green laser were evaluated. It was found that for continuous operation of 100 hours, the output stability was better than 97.5% and no optical damage was observed.

1. Introduction

Compact and efficient green laser light sources have numerous applications such as laser displays, material processing, biological investigations, and optical communications. There are many methods to achieve coherent green light; however, second harmonic generation (SHG) by the quasi-phase-matching (QPM) technique has been an attractive method to obtain compact and high-efficiency laser [1]. The QPM technique based on periodically poled lithium niobate (PPLN) has significant advantages including phase matching of an arbitrary wavelength by the use of an appropriate period of polarization inversion and a higher nonlinear coefficient than KTP, LBO, and BIBO.

So far, the single-pass SHG scheme is a popular solution for achieving CW green laser light. However, this scheme requires a high nonlinear coefficient and a long interaction length to achieve high conversion efficiency, which can be satisfied by employing PPLN crystals. CW green power of 2.7 W has been obtained in a 50 mm long PPLN single-pass crystal pumped by a 6.5 W Nd:YAG laser [2]. Due to its higher photorefractive damage threshold and lower green-induced infrared absorption as compared with PPLN [3], periodically poled MgO:$LiNbO_3$ (PPMgLN) has replaced the PPLN. A maximum power of 1.18 W at 531 nm with 16.8% conversion efficiency has been obtained from a 2 mm thick, 25 mm long PPMgLN single-pass crystal pumped by a 7 W Nd:$GdVO_4$ laser [4]. Periodically poled Mg-doped stoichiometric lithium tantalate (PPMgSLT) is usually used as an alternative material for high-power generation. 7 W of SHG green light with 35.4% conversion efficiency in a 2 cm long PPMgSLT single-pass crystal pumped by a 19.6 W, 1084 nm Yb-doped fiber laser have recently been reported [5].

Intracavity second harmonic generation (ISHG) of Nd-doped lasers has always been an attractive method for producing green light [6]. Second harmonic generation in a bulk PPLN crystal was demonstrated using the intracavity scheme for the first time in 1995 [7]. In a later experiment, 53 μW of green ISHG at 541 nm were generated with a pump power of 300 mW, indicating 0.02% optical-to-optical conversion efficiency in 1997 [8]. A maximum output power of 740 mW of blue light has also been generated with an optical-to-optical efficiency of 5.7% at a pump power of 13.5 W [9].

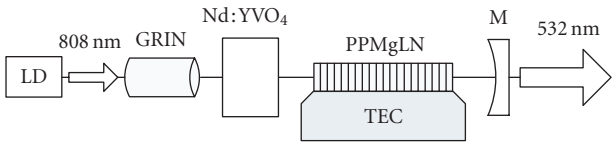

Figure 1: Experimental setup used for ISHG.

In this paper, we report highly efficient continuous-wave green-light generation based on intracavity frequency doubling, in a quasi-phase-matched PPMgLN bulk crystal. With an end-pump power of 2.7 W at 808 nm, a maximum green output power of 908 mW at 532 nm is achieved with a high optical-to-optical conversion efficiency of 33.5%.

2. Experiments

The experimental setup of a high-efficiency CW, laser-diode (LD), and end-pumped green laser with an intracavity SHG scheme is shown schematically in Figure 1. YVO_4 doped with 1% Nd with a size of $3 \times 3 \times 3\,\text{mm}^3$ was used as the gain medium. A 0.5 mm thick, 10 mm long, 2 mm wide, and 5 mol% PPMgLN crystal provided by the C2C Link Corporation, Canada, was used as a frequency doubler. Both sides of the PPMgLN crystal were antireflective (AR), coated at 532 nm and 1064 nm. Temperature of the PPMgLN was controlled by a thermoelectric cooler (TEC).

The laser cavity consisted of a high-reflection (HR) coating at 1064 nm and AR coating at 808 nm on the pumping side of the Nd:YVO_4 crystal, as well as a 50 mm radius of curvature mirror (M) with HR coating at 1064 nm and AR coating at 532 nm, which were used, respectively, for folding the fundamental laser beam and for the second harmonic output. The other side of the Nd:YVO_4 crystal was AR-coated at 1064 nm and HR-coated at 532 nm. The optical end-pump was a CW-2.7 W-laser diode whose end-face was imaged into the pump side of the Nd:YVO_4 crystal by a graded index lens (GRIN). The GRIN with a size of $1.8 \times 5\,(R \times L)\,\text{mm}^3$ was AR-coated at 808 nm.

3. Experimental Results

The CW green laser output power versus the pump power is shown in Figure 2. To obtain the data, the 808 nm pump LD power was varied by changing the injection current of the LD. When the pump power was up to 2.7 W, the green laser delivered 908 mW with 33.5% optical-to-optical conversion efficiency at 35.2°C. To the best of our knowledge, this is the highest optical-to-optical conversion efficiency reported to date for a green laser at low pump power (<5 W). This conversion efficiency is even higher than that obtained for CW single-pass SHG in a bulk PPMgLN with a 1064 nm pump power of 7 W [4]. It is worth noting that the AR coating of the PPMgLN crystal has not been optimized since multiple beam spots were observed in the far-filed pattern of the green laser. We believe that the efficiency can further be enhanced by optimizing the AR coating conditions.

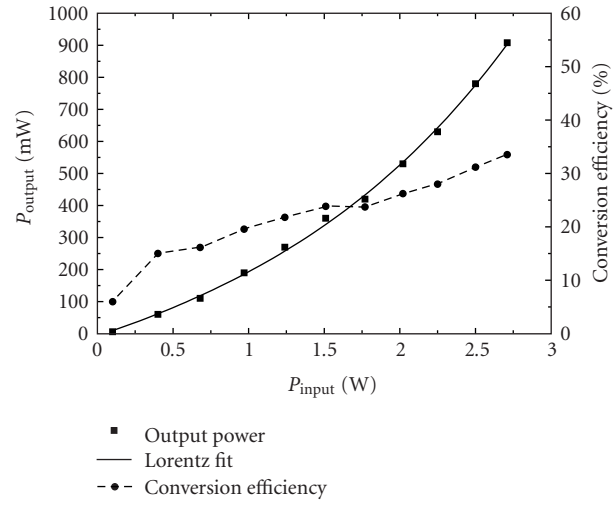

Figure 2: 532 nm green output power and the optical-to-optical conversion efficiency versus 808 nm input power at phase-matching temperature.

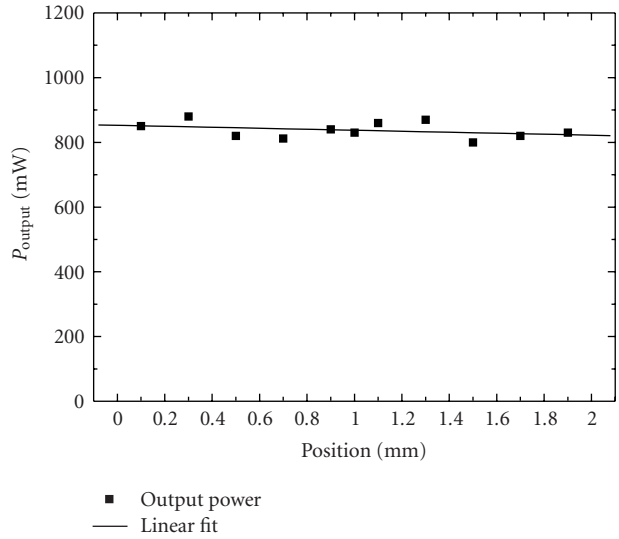

Figure 3: 532 nm output power versus transverse position of PPMgLN crystal at an optical input power of 2.7 W.

In order to measure the uniformity of the PPMgLN crystal at different transverse positions , we shifted the PPMgLN crystal transversely when the temperature was set at the phase-matching temperature, while all other conditions are held constant. As shown in Figure 3, change of the green output power is less than 3%, indicating high uniformity of the PPMgLN crystal. Therefore, it is possible that several beams can pass a single PPMgLN crystal at the same time, which can further enhance the optical-to-optical conversion efficiency.

Maximum green output power can be obtained at the phase-matching temperature for PPMgLN crystal. In the previous reports, the single-pass phase-matching temperature has been investigated, but the phase-matching temperature of the PPMgLN in a laser cavity has not been

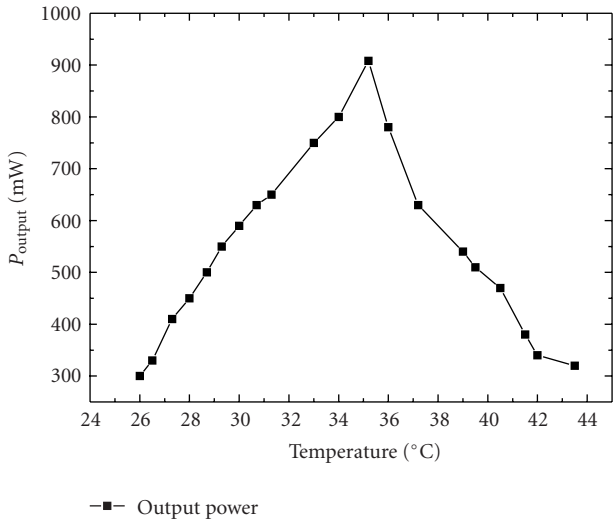

Figure 4: 532 nm output power versus temperature for SHG at an optical input power of 2.7 W.

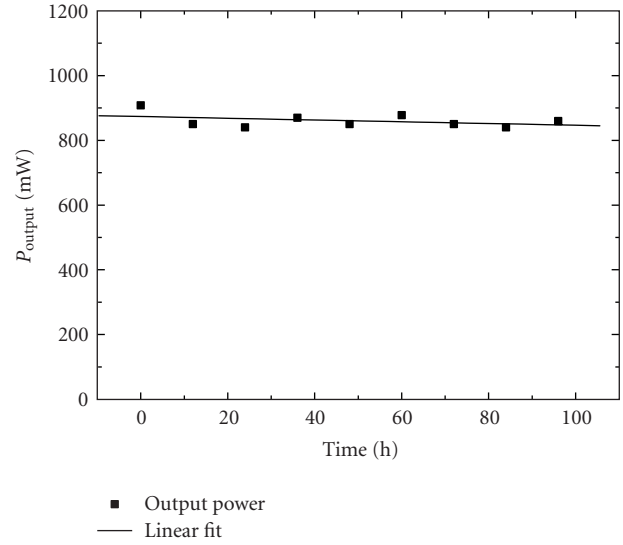

Figure 5: 532 nm output power versus work time for ISHG at phase-matching temperature.

reported. In this paper, the phase-matching temperature of the PPMgLN in the laser cavity was investigated by changing the crystal temperature. As shown in Figure 4, the phase-matching temperature of PPMgLN intracavity frequency doubling is 35.2°C, and the output power is very sensitive to the crystal temperature. The temperature change of 1°C could cause nearly 100 mW output drop. In contrast, in the single-pass scheme, the phase-matching temperature is 38°C, which is 2.8°C higher than that in the intracavity scheme.

To evaluate the reliability and stability of our green laser, continuous operation for 100 hours was carried out. During that period, no drop in green output power was observed, implying that the photorefractive damage is negligible in our experiments. As shown in Figure 5, the change of the green output power is less than 2.5% for 100 hours, indicating that the PPMgLN crystal is a practical material to use in generating stable green laser light. Longer-time experiment for evaluating the stability of the PPMgLN crystal is in process.

4. Conclusions

CW power of 908 mW at 532 nm with 33.5% optical-to-optical conversion efficiency has been obtained from a 0.5 mm thick, 10 mm long PPMgLN crystal in an intracavity frequency-doubling scheme. It has been shown that the efficiency of the intracavity scheme can be much higher than that of single-pass frequency-doubling scheme, indicating that we can obtain higher efficiency and power by employing the intracavity scheme. At the phase-matching temperature, the output power has shown stable operation for more than 100 hours, and the change of the output power is less than 3% at the different transverse positions of the PPMgLN. The experiment results clearly indicate that practically compact and highly efficient green lasers can be realized based on bulk PPMgLN crystals if the uniformity of the crystal is high. We expect that optical-to-optical conversion efficiency of more than 40% could be achieved if the AR coating of the PPMgLN crystal is improved.

Acknowledgments

The authors thank the C2C Link Corporation for helpful discussion as well as providing the high-quality PPMgLN nonlinear crystal. This work was supported by the Nation High-Tech R&D Program ("863" Program, Contract no. 2006AA030103), the National Key Technologies R&D Program (Contract no. 2006BAK12B13), and the National Knowledge Innovation Program (Contract no. KACX1-11).

References

[1] M. M. Fejer, G. A. Magel, D. H. Jundt, and R. L. Byer, "Quasi-phase-matched second harmonic generation: tuning and tolerances," *IEEE Journal of Quantum Electronics*, vol. 28, no. 11, pp. 2631–2654, 1992.

[2] G. D. Miller, R. G. Batchko, W. M. Tulloch, D. R. Weise, M. M. Fejer, and R. L. Byer, "42%-efficient single-pass cw second-harmonic generation in periodically poled lithium niobate," *Optics Letters*, vol. 22, no. 24, pp. 1834–1836, 1997.

[3] S. Kurimura, N. E. Yu, Y. Nomura, M. Nakamura, K. Kitamura, and T. Sumiyoshi, "QPM wavelength converters based on stoichiometric lithium tantalate," in *Advanced Solid-State Photonics (ASSP '05)*, vol. 98, pp. 92–96, Optical Society of America, Vienna, Austria, February 2005.

[4] N. Pavel, I. Shoji, T. Taira, et al., "Room-temperature, continuous-wave 1-W green power by single-pass frequency doubling in a bulk periodically poled MgO:$LiNbO_3$ crystal," *Optics Letters*, vol. 29, no. 8, pp. 830–832, 2004.

[5] S. V. Tovstonog, S. Kurimura, and K. Kitamura, "High power continuous-wave green light generation by quasiphase matching in Mg stoichiometric lithium tantalate," *Applied Physics Letters*, vol. 90, no. 5, Article ID 051115, 3 pages, 2007.

[6] L. Y. Liu, M. Oka, W. Wiechmann, and S. Kubota, "Longitudinally diode-pumped continuous-wave 3.5-W green laser," *Optics Letters*, vol. 19, no. 3, pp. 189–191, 1994.

[7] V. Pruneri, J. Webjörn, P. St. J. Russell, J. R. M. Barr, and D. C. Hanna, "Intracavity second harmonic generation of 0.532 μm in bulk periodically poled lithium niobate," *Optics Communications*, vol. 116, no. 1–3, pp. 159–162, 1995.

[8] K. S. Abedin, T. Tsuritani, M. Sato, and H. Ito, "Integrated intracavity quasi-phase-matched second harmonic generation based on periodically poled Nd:$LiTaO_3$," *Applied Physics Letters*, vol. 70, no. 1, pp. 10–12, 1997.

[9] M. Pierrou, F. Laurell, H. Karlsson, T. Kellner, C. Czeranowsky, and G. Huber, "Generation of 740 mW of blue light by intracavity frequency doubling with a first-order quasi-phase-matched $KTiOPO_4$ crystal," *Optics Letters*, vol. 24, no. 4, pp. 205–207, 1999.

Hindawi Publishing Corporation
Advances in OptoElectronics
Volume 2008, Article ID 956908, 6 pages
doi:10.1155/2008/956908

Research Article

Second Harmonic Generation Using an All-Fiber Q-Switched Yb-Doped Fiber Laser and MgO:c-PPLN

Yi Gan,[1] Xijia Gu,[2] Joyce Y. C. Koo,[2] Wanguo Liang,[1] and Chang-qing Xu[1]

[1] *Department of Engineering Physics, McMaster University, Hamilton, ON, Canada L8S 4L7*
[2] *Department of Electrical and Computer Engineering, Ryerson University, Toronto, ON, Canada M5B 2K3*

Correspondence should be addressed to Yi Gan, gany@mcmaster.ca

Received 13 June 2008; Accepted 26 August 2008

Recommended by Hiroshi Murata

We have experimentally demonstrated an efficient all-fiber passively Q-switched Yb-doped fiber laser with Samarium doped fiber as a saturable absorber. Average output power of 3.4 W at a repetition rate of 250 kHz and a pulse width of 1.1 microseconds was obtained at a pump power of 9.0 W. By using this fiber laser system and an MgO-doped congruent periodically poled lithium niobate (MgO:c-PPLN), second harmonic generation (SHG) output at 532 nm was achieved at room temperature. The conversion efficiency is around 4.2% which agrees well with the theoretical simulation.

1. Introduction

Over the last decades, many different display technologies have been developed to replace the traditional cathode-ray tubs (CRTs), especially in large screen projection market for business and home theater. Laser-based projection display seems to be a superior alternative to existing projection systems because laser light sources can provide extremely wide color expression. Lasers have faster response time and longer life time than any lamps. Moreover, the small system size with high brightness and high power efficiency will also attract the industry [1, 2].

For laser-based projection systems, a high power and high efficient green laser source with compact size is now one of key components. Traditional gas- and dye-based green lasers are not suitable for this application due to their large size, inefficiency, and cumbersomeness to maintain. Although many efforts have been focused on developing semiconductor green laser diodes, the performance achieved to date is still not satisfied because of the material limitation at this wavelength region. Nonlinear frequency conversion of high-power lasers around 1060 nm now seems to be the most practical method for many applications requiring high quality green lasers.

Visible fiber lasers have attracted a lot of attention recently due to potential applications in the fields of industrial processing, bioinstrumentation, and display. Comparing with the conventional Nd:YAG solid-state lasers, the ytterbium (Yb)-doped fiber lasers have strong potential for the systems where air-cooling, long term stability and maintenance-free operation are required. Using Yb-doped fiber lasers and nonlinear crystals to generate CW green light has already been reported [3–5]. But for laser display application, high repetition rate pulse input is more attractive for SHG process. Because the conversion efficiency is proportional to the square of input power, which means under the same average input power, the SHG conversion efficiency of a pulsed input will be much higher than that of a CW input due to the higher pulsed peak power.

In this study, we report an air-cooled simple all-fiber, passively Q-switched Yb doped fiber laser utilizing Sm-doped fiber as an SA. Then using this fiber laser and an MgO-doped periodically poled lithium niobate (MgO-PPLN) crystal, we have achieved high repetition green pulses output at room temperature. The characteristics of fiber laser output and SHG light have been investigated.

2. All-Fiber Q-Switched Yb-Doped Fiber Laser

Compact Yb-doped Q-switched fiber lasers have attracted significant interests as it could provide a high power, high

efficiency and low cost source for many applications. There are different technologies to Q-switch fiber laser that includes active Q-switching using, for example, piezoelectric modulator [6], electrooptic modulator [7], and acoustic modulator [8]. The other alternative is the passive Q-switching using a saturable absorber (SA) in laser cavity that offers much simpler design as compared to the active Q-switching. Huang et al. reported recently a passively Q-switched Yb-doped fiber laser with Cr4+: YAG as an SA and achieve a high peak power of 20 kW [9]. However their laser consists of a Cr4+: YAG slab, three collimating and focus lenses, and a mirror that complicated substantially the laser cavity design. Dvoyrin et al. reported pulsed Yb-doped fiber lasers with Bismuth-doped fiber as an SA [10]. They succeeded in Q-switching in wide wavelength range from 1050 to 1200 nm with pulse width from 1 to 1.5 microseconds at a repetition rate from 10 to 100 kHz. Nevertheless, the stable pulse operation was only obtained in double-cavity design and the peak power was limited to 40 W at 1064 nm. Fotiadi et al. described the dynamics of an all-fiber self-Q-switched Yb-doped fiber laser with a samarium absorber [11]. Regular pulse operation was observed at discrete pump levels and the dynamics was attributed to polarization mode switching. It appears that though saturable absorbers have been successfully employed in Q-switching solid-state lasers, it is still an interesting research topic to achieve high repetition rate, high peak power Q-switching in Yb-doped fiber laser.

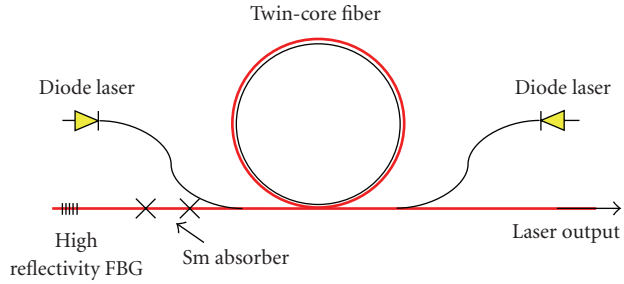

Figure 1: Schematic of an all-fiber Q-switched fiber laser design.

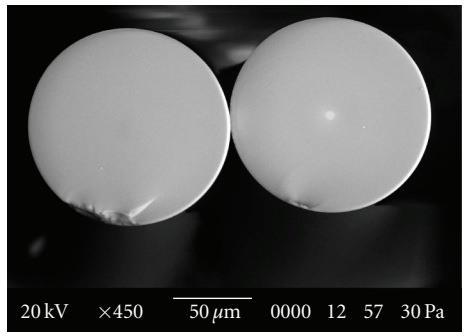

Figure 2: SEM image of the cross-section of the twin-core fiber coated with lower index of polymer. The left core is for pumping and the right one has a Yb-doped core.

2.1. Experiments

The schematic of the fiber laser configuration is shown in Figure 1. It consists of two pump lasers of 975 nm to provide bidirectional pump, 10.5 meters of twin-core fiber, a piece of Sm-doped fiber as an absorber and one highly reflective fiber Bragg grating (FBG). The twin-core fiber has two optically contacted large cores, coated with a low refractive index polymer as shown in Figure 2. The single-mode Yb-doped active core has a diameter of 6.7 μm and an NA of 0.13. The multimode core has a diameter of 118 μm with a multimode absorption coefficient of 0.77 dB/m at the pump wavelength. The advantage of this coupling method is the ability to increase the output power from the fiber laser by coupling multiple pump sources at both ends, or by exploiting the physical separation between the pump and active paths in which the independent access to the pump path allows for power scaling by adding the pump power along the fiber length. The efficient light coupling between the pump and active cores had been described recently in [12]. The single mode Sm-doped SA was obtained from CorAcitve (Sm119) with an NA of 0.14 and a core diameter of 6.3 μm. Its peak absorption near 1064 nm was measured to be 8 dB/m.

We select Sm-doped absorber for its fast response time [13]. In its near IR absorption band, the lifetime of upper energy level is less than 5 nanoseconds that is essential to achieve narrow pulse width and high repetition rate when used in Q-switching.

The diode pump laser has a fiber-coupled output though a multimode fiber of 105/125 μm core/cladding diameter, capable of delivering up to 6.5 W of optical power at 975 nm. The high reflectivity FBG was fabricated in house with a reflectivity of >99.9% and a −3 dB bandwidth of 0.6 nm centered at 1063.37 nm.The cleaved end of the active fiber served as a 4% output coupler.

The temporal behavior of pulse train was recorded with an InGaAs photodiode with a bandwidth of 80 MHz (New Focus, model: 2117) and a digital oscilloscope (Tektronix, model: TKD 3032B). The rise time of the InGaAs photodiode is about 3 nanoseconds. Optical spectra were recorded with an optical spectral analyzer (OSA) (Ando Corp. model: AQ-6315E). A power meter (Coherent, model: FieldMaster-GS) was used to measure CW laser power or average power of a Q-switched pulse train.

In our laser configuration, no active cooling was required for all fiber components. Two pump diode lasers were mounted on heat dissipate plates and fiber assembly used a standard anodized aluminum fiber tray mounted on an aluminum metal plate, which separates the electrical and optical compartments in the system. The power supply, providing up to 10A of current, uses a conventional fan for convection cooling.

2.2. Results and Discussion

Before inserting the Sm-doped SA, the CW output of the laser, assembled with same components less than that of an SA, was characterized by providing a reference for the performance of Q-switched laser output. The CW output

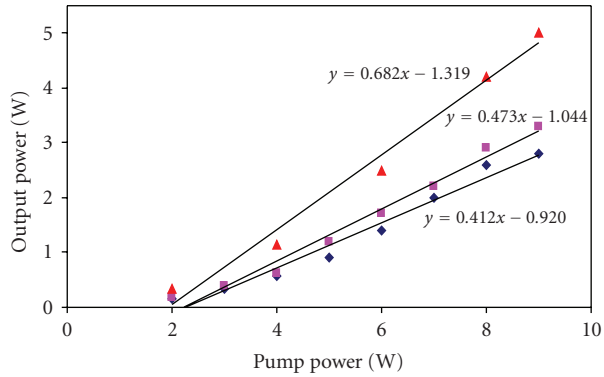

Figure 3: The average output power versus pump power: for CW output (▲); for Q-switched output with a 0.45 m of Sm-absorber (■); that with a 0.6 m of Sm-absorber (♦).

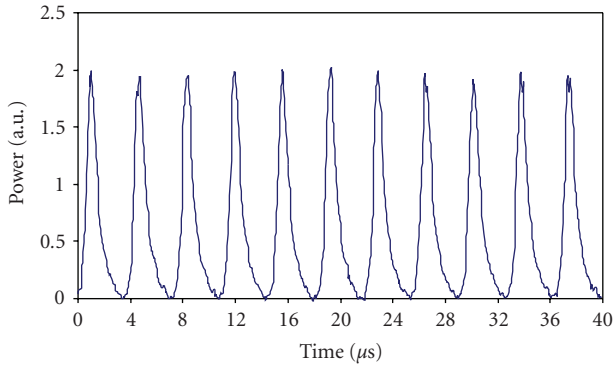

Figure 4: Typical Q-Switched pulse train recorded with oscilloscope at a pump power of 8.4 W.

as a function of pump power is plotted in Figure 3. In CW operation, the laser delivered 5 W at a pump power of 9 W with a slope efficiency reached 68%.

After inserting 0.6 m of Sm-doped SA, the Q-switched output gave an average power of 2.8 W at a pump power of 8.2 W with a power conversion efficiency of 41%. The laser with a shorter Sm-absorber fiber length of 0.45 m improved the slope efficiency and produced higher average power (see Table 1 for more details). The average output power of the Q-switched laser as function of the pumped power for two Sm-absorber lengths is also plotted in Figure 3. The Q-switching efficiency (the ratio of the Q-switched slope efficiency to that of CW one) was 69% and 60% for 0.45 m and 0.6 m of Sm-absorber, respectively, indicating that Sm-abosrber is a good candidate for Q-switching fiber laser.

Stable Q-switched pulses were obtained when the pump power was at much higher level than the threshold value. Figure 4 displays the oscilloscope trace of the pulse train. The pulse shape exhibits a fast leading edge and a slow falling edge that is typical for the Q-switched pulse. The pulse width was measured to be 800 nanoseconds at FWHM and the pulse duration is 3.6 microseconds for a 0.6 m long Sm-doped fiber at 8.4 W pump power. The pulse-to-pulse stability was better than ±5%. If the pump power is increased over 9 W,

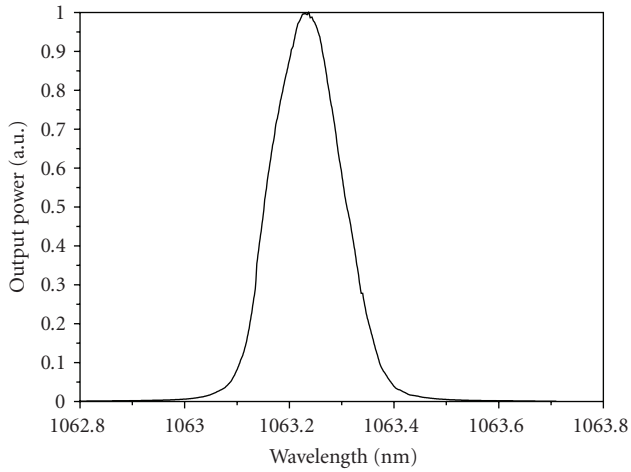

Figure 5: The output spectrum of the Q-switched fiber laser.

Table 1: Parameters of Yb-Sm Q-switched fiber laser.

	Sm-absorber length	
	0.6 m	0.45 m
Repetition rate, kHz	278	250
Pulse width, μs	0.80	1.1
Pulse energy, μJ	10.1	13.6
Maximum average power, W	2.8	3.4
Slope efficiency, %	41	47

the average output power that was attributed to the onset of nonlinear effects will start to decrease.

The spectrum of the Q-switched pulse output was measured by an OSA with its resolution set at 0.05 nm. Figure 5 shows the spectrum at an average output power of 1.0 W for 0.45 m of Sm-absorber. Its −3 dB bandwidth is as broad as 0.158 nm.

3. Second Harmonic Generation

Single-pass wavelength conversion by a nonlinear optical (NLO) crystal becomes one of the most attractive methods to generate coherent radiation in various spectral domains from ultraviolet to mid-infrared since QPM was first proposed in the early days of nonlinear optics [14]. Especially, as periodically poling technology became commercially available. Compared with other phase matching methods such as birefringent phase matching (BPM) technique, QPM technique allows us to use the largest nonlinear coefficient over the whole transparent spectral range of the crystal without the walk-off effect.

Among all the periodically poled crystals, periodically poled lithium niobate (PPLN) has been one of the most attractive materials due to its large second-order nonlinear coefficient, wide transparency band width covering UV to IR, mature and low cost fabrication process [15]. However, PPLN will suffer from pointing instability at medium powers and permanent photorefractive damage at high power [16]. Usually PPLN crystals have to heat to the temperature

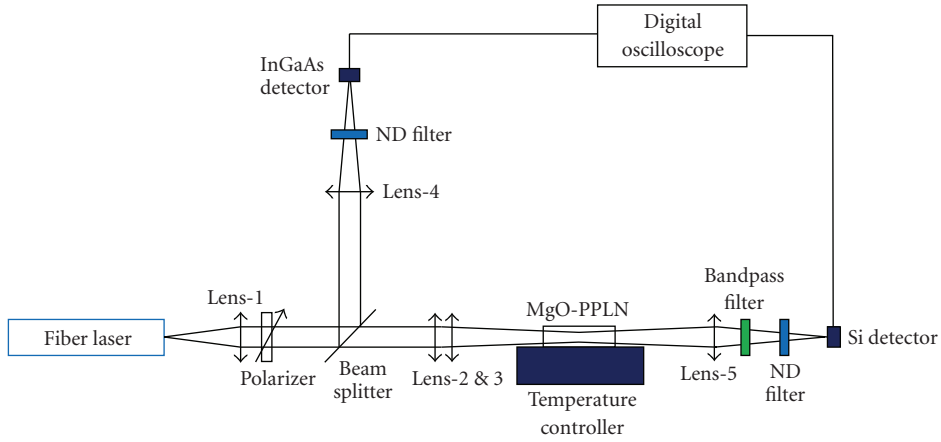

Figure 6: Second harmonic generation experimental setup.

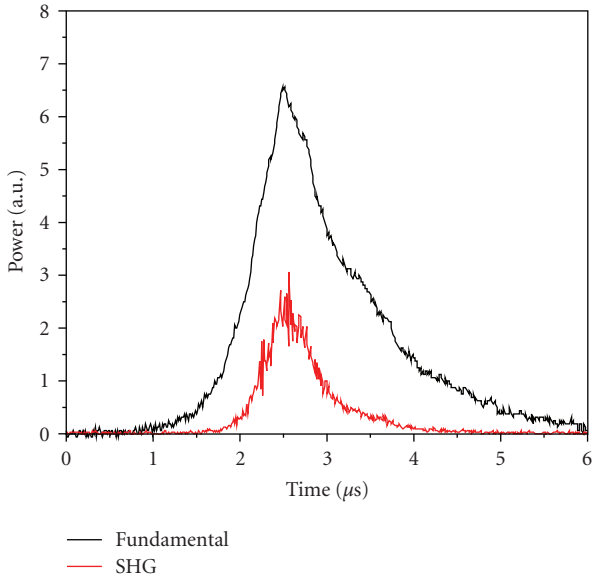

Figure 7: Fundamental pulse and SHG pluse.

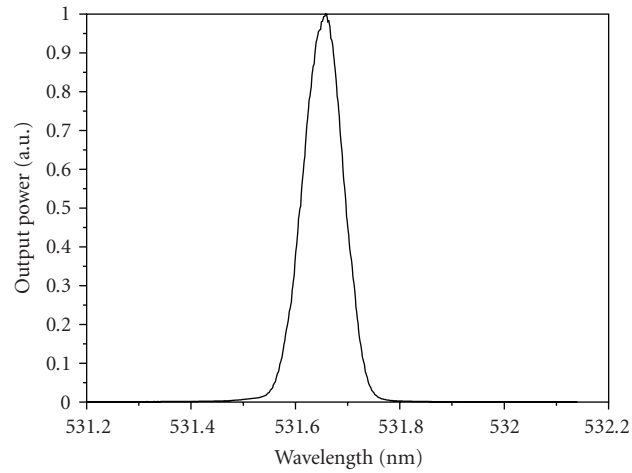

Figure 8: The output spectrum of SHG light.

over hundred degrees to reduce these effects. This effect also can be reduced by doping some magnesium oxide (MgO) into the crystal during growth. Compared to pure $LiNbO_3$ crystals, 4%-5% MgO:c-PPLN crystals can increase the resistance against optical damage hundred times higher, which allows devices working with high input and output power at room temperature [17].

3.1. Experiments

An electric-field poling technique was applied to fabricate the periodic domain structure on a 0.5 mm thick 3-inch 5% MgO:c-PPLN wafer. Typically, the applied voltage is around 21 kV. A uniform periodically poled structure with periods of 6.5 μm was obtained with a 50% duty ratio on the +Z face.

The experimental setup is schematically shown in Figure 6. Fundamental light from Q-switched fiber laser is collimated by a 10x objective lens (Lens-1). Since only the TM-polarization can satisfy the QPM condition, a polarizer is used to make the fundamental light's polarization parallel with the Z-direction of PPLN. A small part of fundamental light is separated by a beam splitter and focused by Lens-4 onto an InGaAs detector (Thorlabs, model: PDA10CS). The main stream of fundamental beam is focused by two lens (Lens-2&3). These two lenses can adjust the beam diameter to satisfy the optimum confocal condition for different sample length. In this paper, the sample length is 15 mm so the beam is focused to a 50 μm spot radius in the center of the sample.

The sample was mounted in a temperature-controlled oven (Thorlabs, model: TC200) and the temperature was set to 34.5°C which optimizes the QPM condition of the sample. SHG light was focused by Lens-5 and a bandpass filter is used to block the fundamental light. An Si detector (Thorlabs, model: PDA10A) is used for the measurement of the pulses trains. Both two detectors are connected to a digital oscilloscope (LeCroy, Model: LT224) for pulses trains recording. In this way, we can record the fundamental

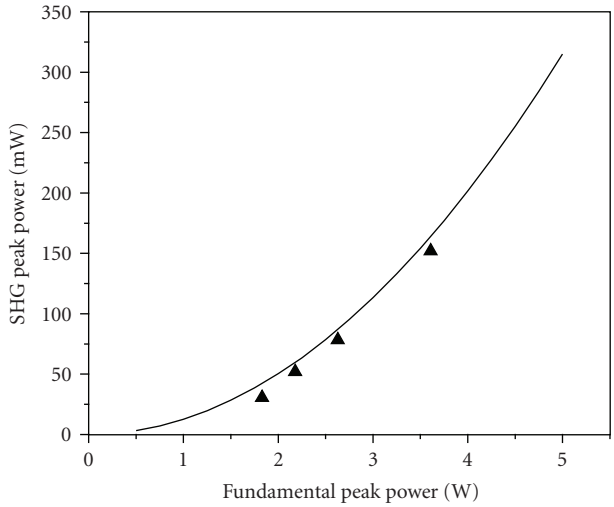

Figure 9: SHG peak power as a function of the fundamental peak power: the triangle dots and solid line represent experimental data and the theoretical simulation result.

pulses and SHG pulses synchronously in order to accurately compare each other. The responsivities of two detectors were calibrated by two CW DPSS lasers at 1064 nm and 532 nm, respectively.

3.2. Results and Discussion

Figure 7 shows the comparison of a fundamental pulse and an SHG pluse. The fiber laser used in SHG experiments is connected with 0.45 m Sm-absorber, as described before; the fundamental pulse width is about 1.1 microseconds. Becasue the SHG power is proportional to the squre of fundamental pulse, the SHG pulse FWHM width should be 0.707 fundamental pulse. As shown in Figure 7, the SHG pulse width is about 0.75 microsecond.

Figure 8 shows the output spectrum of SHG light at 531.64 nm. The −3 dB bandwidth is about 0.09 nm which is slightly narrower than that of the fundamental light at 1063.25 nm.

The SHG peak power is plotted against the incident fundamental peak power as shown in Figure 9. The SHG peak power of 152 mW was achieved when the fundamental peak power was 3.6 W (average power is 1 W). The conversion efficiency (SHG pulse power/fundamental pulse power) is 4.2% which agrees with the theoretical simulation result. The conversion efficiency can be expected to be above 90% when the input fundamental peak power is in kW level.

4. Conclusion

We have demonstrated an all-fiber, high repetition rate and high peak power passively Q-switched Yb-doped fiber laser using Sm-doped fiber as an SA. With a pump power of 8.4 W, the fiber laser outputs stable pulses with a pulse width of 1.1 microseconds at a repetition rate of 250 kHz, producing an average output power of 3.4 W. All fiber connections were fusion spliced and fiber was looped in a $15 \times 12 \times 0.8\,\text{cm}^3$ compact fiber tray. This laser design showed a significant improvement as compared with other Q-switched fiber lasers and has the following features: (a) all fiber components were splice connected, which avoided the use of any bulk optics, (b) realized bidirectional pumping using a twin-core fiber that separated pump path from the active signal path, (c) demonstrated high repetition rate in the order of 200 kHz.

Using this novel fiber laser and an MgO-PPLN wavelength conversion device, we have obtained the green laser with peak power of 150 mW at room temperature. The conversion efficiency is 4.2% which agrees well with the theoretical value. The MgO:c-PPLN sample is 15 mm long and the temperature is controlled at 34.5°C to satisfy QPM condition. The conversion efficiency will be higher if we can achieve high peak power for fundamental light from fiber laser. Further increasing the peak power is currently limited by the nonlinear effects in fiber laser and will be improved by the use of larger core active fiber. The all-fiber configurations provide a simple, low cost and easy to manufacturing solution for high power Q-switched pulse laser that should be attractive to micromachining, medical treatment, and other applications.

Acknowledgments

This work is partially supported by Natural Sciences and Engineering Research Council of Canada (NSERC), Canadian Institute for Photonics Innovations (CIPI), Ontario Centres of Excellent (OCE), and Canadian Foundation for Innovation (CFI).

References

[1] J. Lee, Y. Mun, S. Do, et al., "Laser TV for home theater," in *Projection Displays VIII*, vol. 4657 of *Proceedings of SPIE*, pp. 138–145, San Jose, Calif, USA, January 2002.

[2] G. Niven, "Laser TV: coming to a home theatre near you," *Opto & Laser Europe*, no. 142, pp. 33–34, 2006.

[3] F. J. Kontur, I. Dajani, Y. Lu, and R. J. Knize, "Frequency-doubling of a CW fiber laser using PPKTP, PPMgSLT, and PPMgLN," *Optics Express*, vol. 15, no. 20, pp. 12882–12889, 2007.

[4] H. Furuya, A. Morikawa, K. Mizuuchi, and K. Yamamoto, "High-beam-quality continuous wave 3 W green-light generation in bulk periodically poled MgO:$LiNbO_3$," *Japanese Journal of Applied Physics*, vol. 45, no. 8B, pp. 6704–6707, 2006.

[5] S. V. Tovstonog, S. Kurimura, and K. Kitamura, "High power continuous-wave green light generation by quasiphase matching in Mg stoichiometric lithium tantalate," *Applied Physics Letters*, vol. 90, no. 5, Article ID 051115, 3 pages, 2007.

[6] M. Leigh, W. Shi, J. Zong, J. Wang, S. Jiang, and N. Peyghambarian, "Compact, single-frequency all-fiber Q-switched laser at 1 μm," *Optics Letters*, vol. 32, no. 8, pp. 897–899, 2007.

[7] Y. Wang and C.-Q. Xu, "Modeling and optimization of Q-switched double-clad fiber lasers," *Applied Optics*, vol. 45, no. 9, pp. 2058–2071, 2006.

[8] Y. Kaneda, Y. Hu, C. Spiegelberg, J. Geng, and S. Jiang, "Single-frequency, all-fiber Q-switched laser at 1550 nm," *OSA Trends in Optics and Photonics Series*, vol. 94, pp. 126–130, 2004.

[9] J. Y. Huang, H. C. Liang, K. W. Su, and Y. F. Chen, "High power passively Q-switched ytterbium fiber laser with Cr^{4+}: YAG as a saturable absorber," *Optics Express*, vol. 15, no. 2, pp. 473–479, 2007.

[10] V. V. Dvoyrin, V. M. Mashinsky, and E. M. Dianov, "Yb-Bi pulsed fiber lasers," *Optics Letters*, vol. 32, no. 5, pp. 451–453, 2007.

[11] A. A. Fotiadi, A. S. Kurkov, and I. M. Razdobreev, "Dynamics of all fiber self-Q-switched Ytterbium/Samarium laser," in *Proceedings of the Laser and Electro-Optics/Quantum Electronics and Laser Science Conference (CLEO/QEC '07)*, pp. 1–2, Baltimore, Md, USA, May 2007, paper CMC4.

[12] X. J. Gu and Y. Liu, "The efficient light coupling in a twin-core fiber waveguide," *IEEE Photonics Technology Letters*, vol. 17, no. 10, pp. 2125–2127, 2005.

[13] B. Wu and P. L. Chu, "Fast optical switching in Sm^{3+}-doped fiber," *IEEE Photonics Technology Letters*, vol. 8, no. 2, pp. 230–232, 1996.

[14] J. A. Armstron, N. Bloembergen, J. Ducuing, and P. S. Pershan, "Introductions between light waves in a nonlinear dielectric," *Physical Review*, vol. 127, no. 6, pp. 1918–1939, 1962.

[15] K. K. Wong, *Properties of Lithium Niobate*, INSPEC, Edison, NJ, USA, 2002.

[16] G. D. Miller, R. G. Batchko, W. M. Tulloch, D. R. Weise, M. M. Fejer, and R. L. Byer, "42%-efficient single-pass cw second-harmonic generation in periodically poled lithium niobate," *Optics Letters*, vol. 22, no. 24, pp. 1834–1836, 1997.

[17] D. A. Bryan, R. Gerson, and H. E. Tomaschke, "Increased optical damage resistance in lithium niobate," *Applied Physics Letters*, vol. 44, no. 9, pp. 847–849, 1984.

Hindawi Publishing Corporation
Advances in OptoElectronics
Volume 2008, Article ID 428971, 10 pages
doi:10.1155/2008/428971

Research Article

Noise Analysis of Second-Harmonic Generation in Undoped and MgO-Doped Periodically Poled Lithium Niobate

Yong Wang,[1] Jorge Fonseca-Campos,[1] Wan-guo Liang,[1] Chang-Qing Xu,[1] and Ignacio Vargas-Baca[2]

[1] *Department of Engineering Physics, McMaster University, Hamilton, ON, Canada L8S4L8*
[2] *Department of Chemistry, McMaster University, Hamilton, ON, Canada L8S4L8*

Correspondence should be addressed to Wan-guo Liang, wgliangy@yahoo.com

Received 29 February 2008; Accepted 21 July 2008

Recommended by Yalin Lu

Noise characteristics of second-harmonic generation (SHG) in periodically poled lithium niobate (PPLN) using the quasiphase matching (QPM) technique are analyzed experimentally. In the experiment, a0.78 μm second-harmonic (SH) wave was generated when a 1.56 μm fundamental wave passed through a PPLN crystal (bulk or waveguide). The time-domain and frequency-domain noise characteristics of the fundamental and SH waves were analyzed. By using the pump-probe method, the noise characteristics of SHG were further analyzed when a visible light (532 nm) and an infrared light (1090 nm) copropagated with the fundamental light, respectively. The noise characterizations were also investigated at different temperatures. It is found that for the bulk and waveguide PPLN crystals, the SH wave has a higher relative noise level than the corresponding fundamental wave. For the same fundamental wave, the SH wave has lower noise in a bulk crystal than in a waveguide, and in MgO-doped PPLN than in undoped PPLN. The 532 nm irradiation can lead to higher noise in PPLN than the 1090 nm irradiation. In addition, increasing temperature of device can alleviate the problem of noise in conjunction with the photorefractive effect incurred by the irradiation light. This is more significant in undoped PPLN than in MgO-doped one.

1. Introduction

Among a variety of nonlinear optical processes, second-harmonic generation (SHG) is one of the most well-known wavelength-conversion schemes [1–3]. In order to enhance the conversion efficiency of SHG, the phase velocities of the interacting waves must be matched, which can be achieved, for example, by selecting appropriate polarization states and the incident angle of a birefringent crystal [1]. Another method to match the phase velocities of the interacting waves is the quasiphase matching (QPM) technique, in which the ferroelectric domains of a nonlinear crystal are inverted periodically, and thus the phases of the interacting waves are controlled in a coherence length to produce constructive interference between the generated waves in different regions of the nonlinear optical medium [2, 3]. There are several advantages of this technique over other phase matching techniques. In particular, any wavelength can be phase-matched in the transparent range of a $LiNbO_3$ crystal simply by choosing a suitable poling period in the QPM structure; the largest nonlinear component (i.e., d_{33}) can be obtained; the propagating waves can undergo the largest nonlinear interaction in the crystal, enhancing the conversion efficiency and offering the possibility of engineering the nonlinearity [2–5].

In such nonlinear SHG processes, it is well known that the conversion efficiency of SHG is proportional to the power of the fundamental wave [1–3]. Therefore, high-power light sources (up to ~200 mW) are required to achieve efficient conversions in many practical applications [6, 7]. It has been found that $LiNbO_3$ waveguides are more vulnerable to high-power irradiating light than bulk crystals, especially to lightwave with a shorter wavelength, due to the photorefractive effect (PRE) [7–12]. In addition, in both bulk and waveguide PPLN crystals, the phase-matching conditions are influenced by the temperature distribution along the optical path of the interacting wave; and high-power irradiation is apt to generate uneven temperature distribution [2, 7, 13].

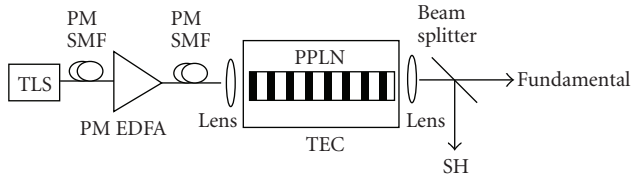

Figure 1: Experimental setup of SHG. PM SMF: polarization maintaining single-mode fiber. TLS: tunable laser source.

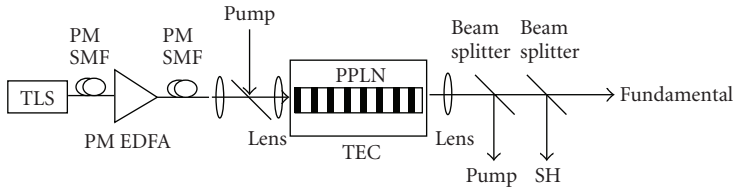

Figure 2: Experimental setup of SHG with a pump. PM SMF: polarization-maintaining single-mode fiber. TLS: tunable laser source.

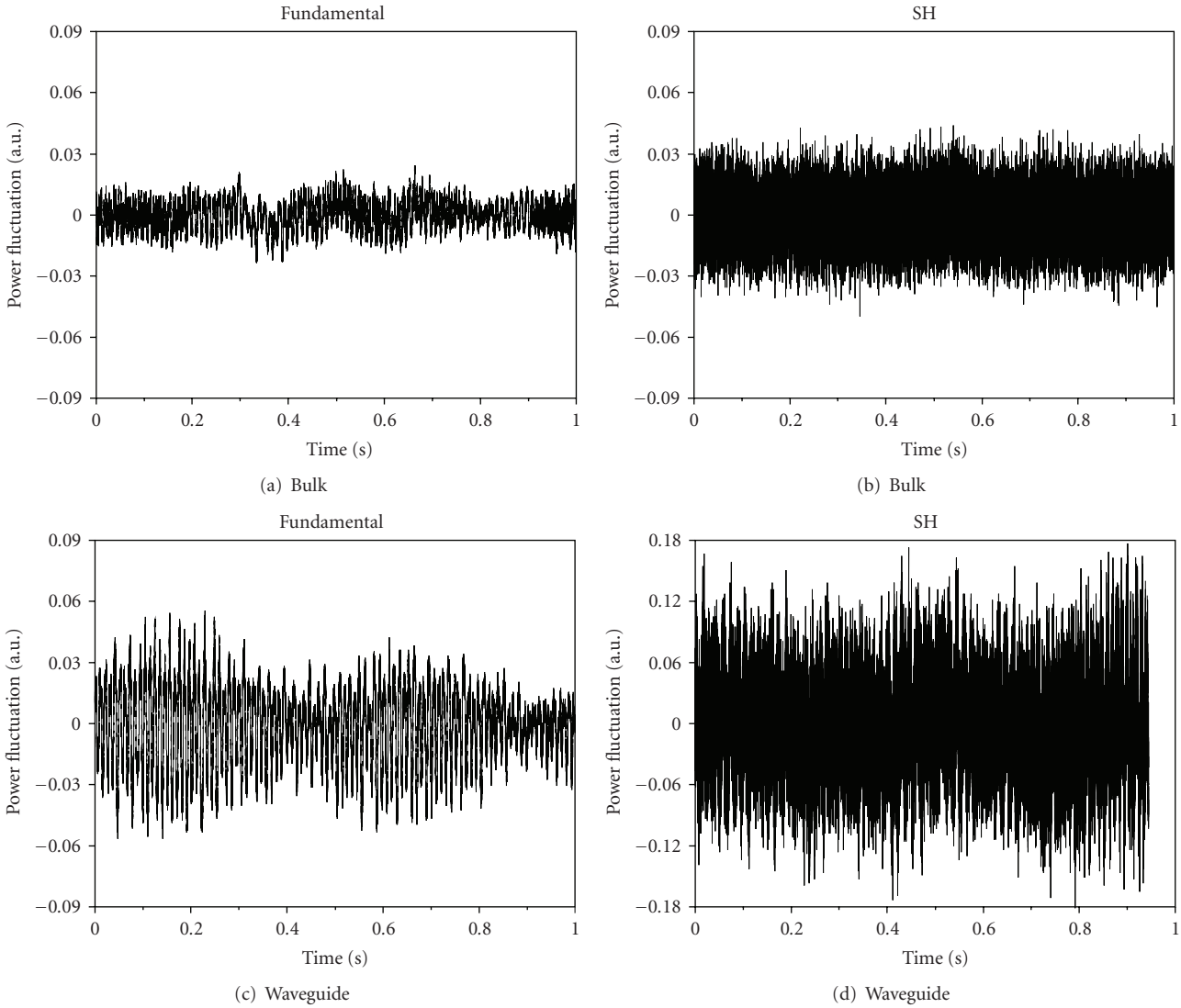

Figure 3: Power fluctuations of fundamental and SH waves in undoped PPLN crystal measured in the time domain. It is shown that the SH wave has higher peak-to-peak fluctuation than that of the fundamental wave; and for either wave, the waveguide leads to higher noise than the bulk crystal.

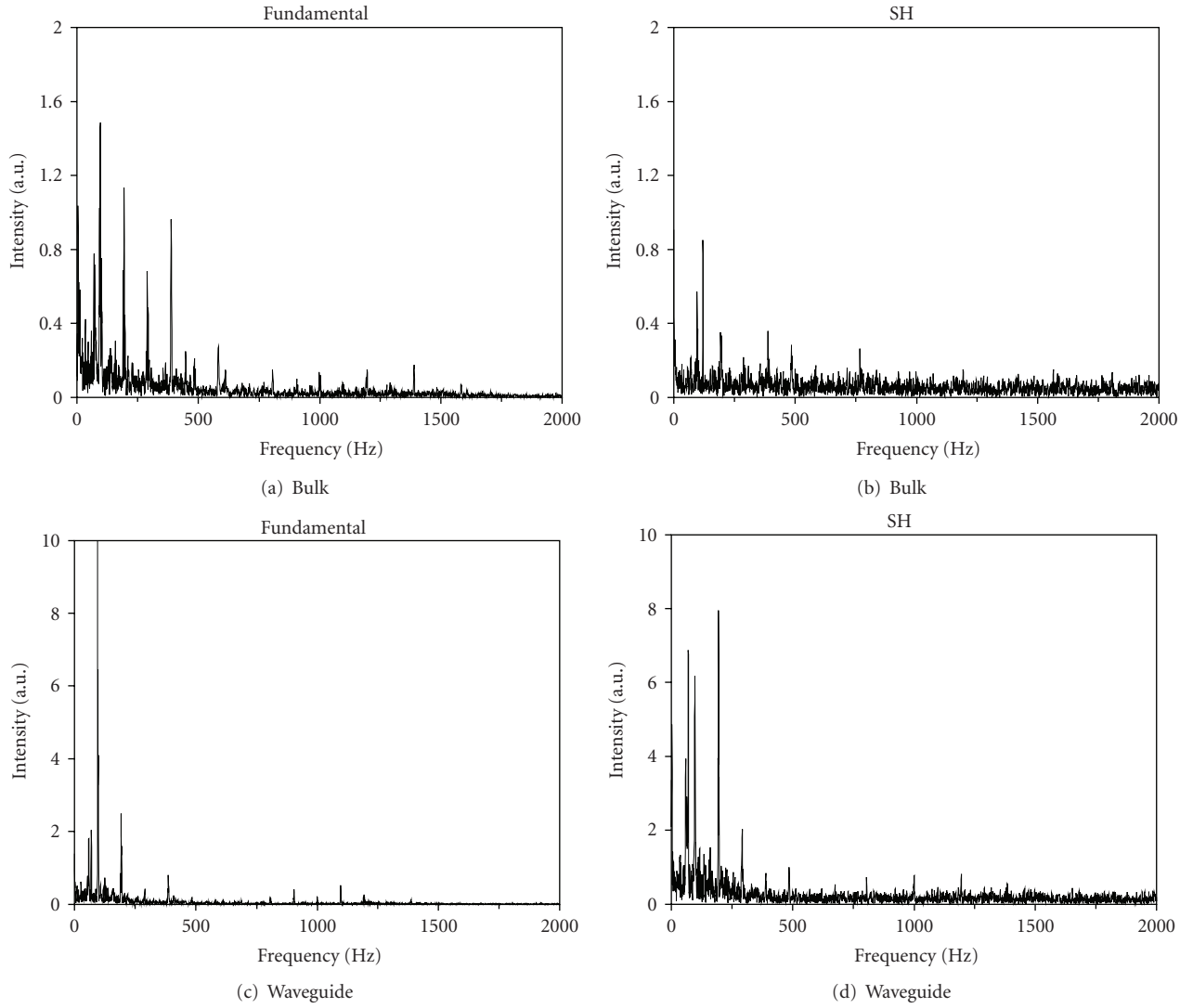

Figure 4: Frequency spectra corresponding to the fundamental and SH temporal output traces in Figure 3.

As a result, the thermal effect is an important aspect to be taken into account in high-power applications. In many applications, such as lidar, remote sensing, spectroscopy, coherent communications, dense wavelength-division, and time-division multiplexing and demultiplexing, the noise characteristics of second-harmonic (SH) waves generated in nonlinear interactions are concerned since the noise in the SH wave can significantly impact the accuracy of measurement [2–5, 14–16]. As a result, it is important to investigate the noise characteristics in SHG processes under different conditions, such as power, material, temperature, and so forth. So far, few systematic investigations of noise characteristics under different operating conditions and comprehensive comparisons of noise in bulk and waveguide PPLN as well as in doped and undoped crystals have been reported in the literature to the best of our knowledge.

In this work, we experimentally investigated the noise characteristics of SHG in undoped and 5 mol % MgO-doped PPLN crystals. In the experiment, a 0.78 μm SH wave was generated when a 1.55 μm fundamental wave passed through a PPLN bulk or an annealed proton-exchanged waveguide. The fundamental and SH waves were then separated through a beam splitter and sent to two photodetectors, respectively. By analyzing the time-domain and frequency-domain characteristics of the fundamental and SH waves, we studied the noise characteristics of the fundamental and SH waves. Furthermore, we applied a visible (532 nm) and an infrared (1090 nm) irradiation wave to the crystals, respectively, and observed the change of noise characteristics in the case of apparent photorefractive effects. The results obtained in this work are helpful and provide some guides in design and applications of SHG in PPLN.

2. Experimental Setup

The experimental setup is schematically shown in Figure 1, including a tunable laser source (Agilent 8164A), a thermal-electrical controller (TEC), a polarization-maintaining

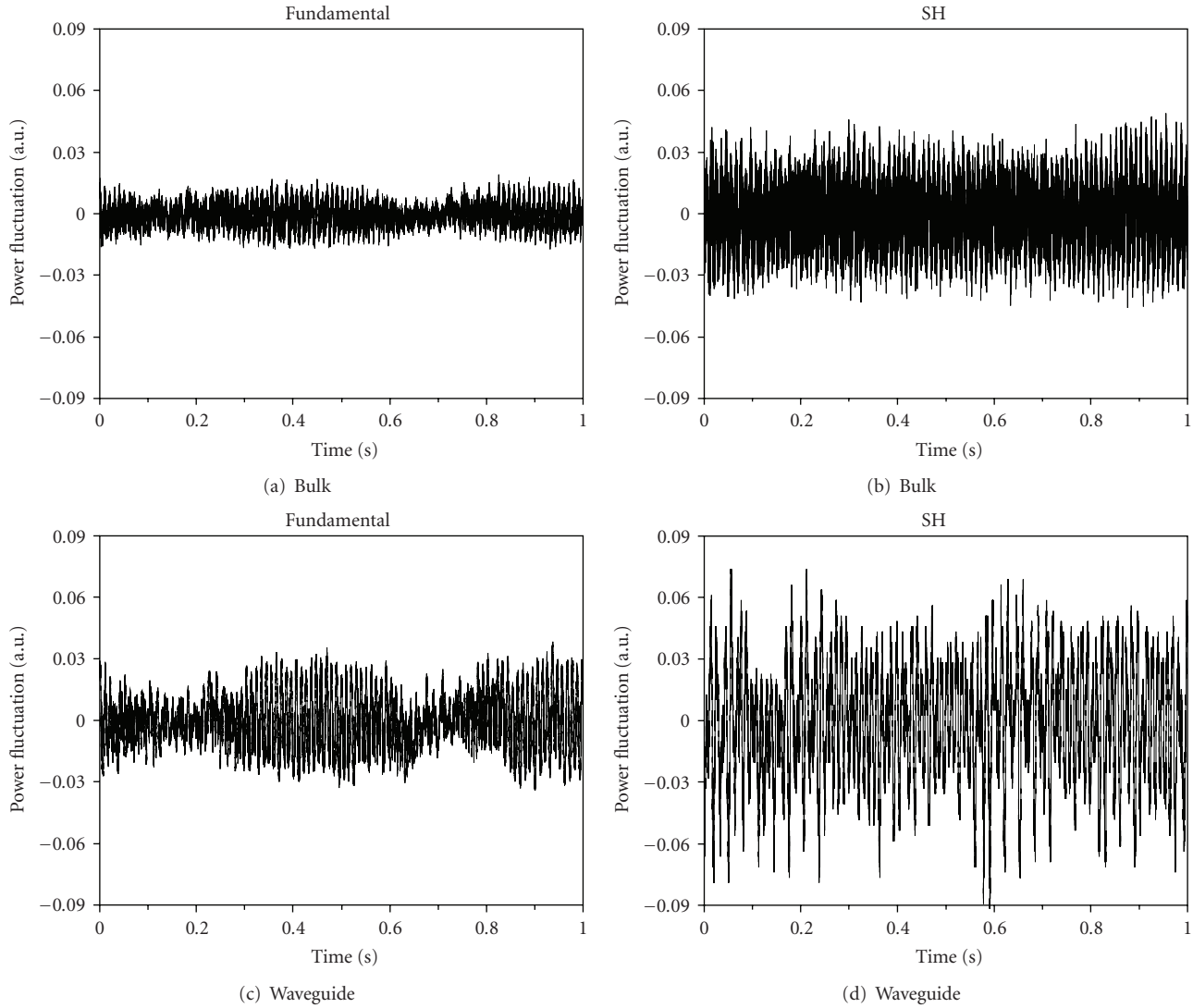

Figure 5: Power fluctuations of fundamental and SH waves in MgO-doped PPLN crystal.

erbium-doped fiber amplifier (EDFA, KEOPSYS), and a wavelength-selective beam splitter. The temperature of the PPLN crystal is controlled using the TEC. Two pieces of polarization-maintaining fibers were used to connect the tunable laser and the EDFA. The output wave from the EDFA passed through a narrow bandpass filter to eliminate amplified spontaneous emission (ASE) of the amplifier. Two focusing lenses were used to couple light into and out of the PPLN crystal. The maximal injected power of the fundamental wave into the PPLN crystal was 500 mW. The output fundamental and SH waves from the PPLN crystal were separated through the beam splitter.

The crystal poling periods are in the range of 17–19 μm, which ensures their QPM wavelengths of SHG locate in the wavelength range of the tunable laser. The QPM structure was poled by the electrostatic discharge method, while the waveguides were fabricated by using the proton exchange technique and they only support the transverse-magnetic (TM) modes [13, 14, 17]. For the fundamental wave propagating in the bulk PPLN crystals, the beam waist was focused to 30–40 μm in diameter.

We also studied the noise characteristics of PPLN with extra pump irradiation at wavelength of 0.532 and 1.09 μm, respectively, by using the pump-probe method. The influence of the pump irradiation on the SHG noise was investigated experimentally. The experimental setup is shown in Figure 2, where another two-beam splitters were inserted in the optical path of Figure 1, used to combine the fundamental wave (namely, probe) and the pump light into the PPLN crystal at its input end, and to separate the pump light from the fundamental and SHG waves at the output end of the crystal, respectively. The other components and their functions are the same as those in the previous setup. The 532 nm green light is generated from a CW intracavity frequency-doubled Nd:YAG laser (Coherent, Verdi), whose maximal output power is 2 W. The 1090 nm light is from a single-mode Yb-doped double-clad fiber laser, and its maximal output power used in the experiment is 1 W.

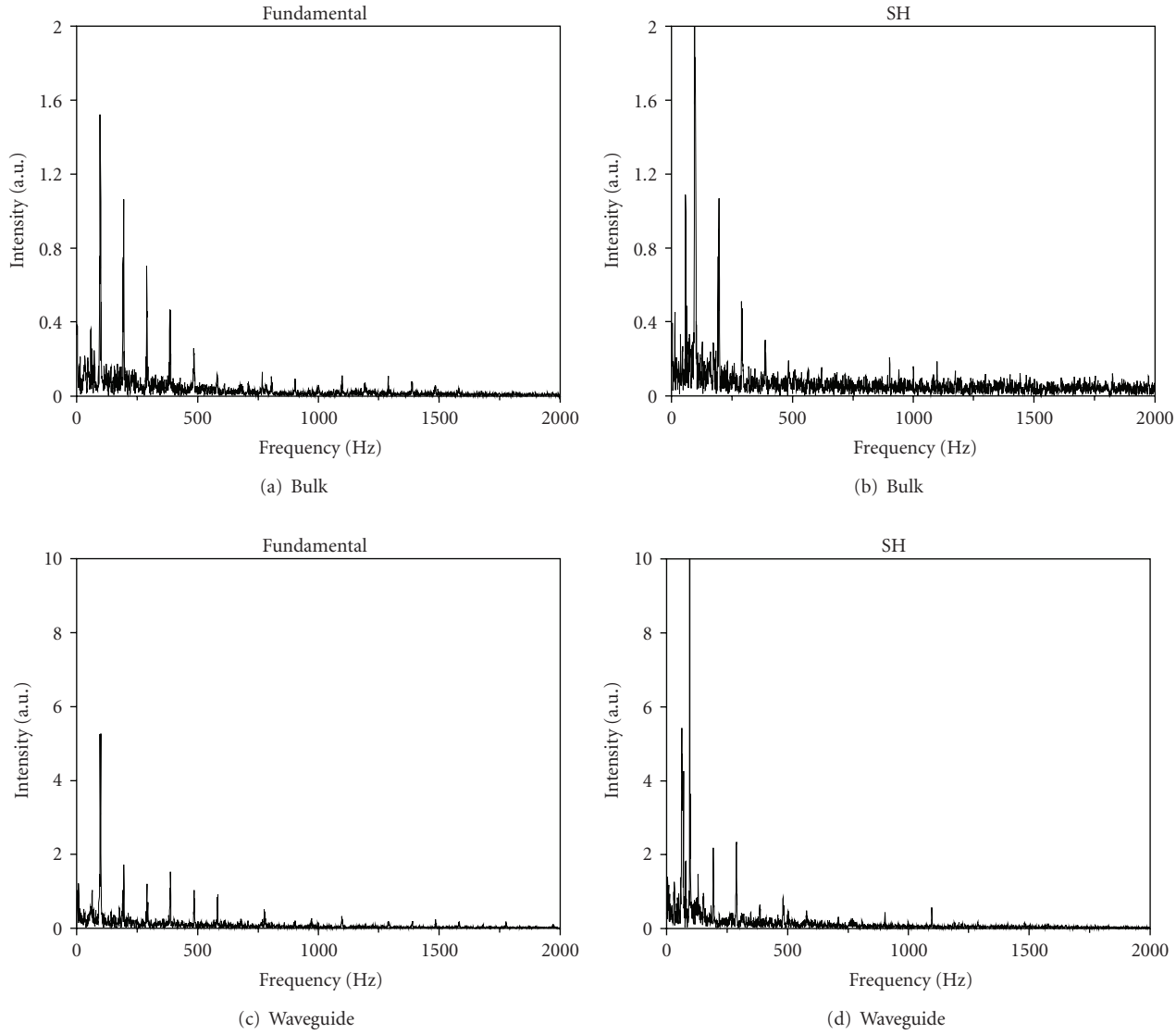

Figure 6: Frequency spectra corresponding to the fundamental and SH temporal output traces in Figure 5.

Table 1: RMS noise values of fundamental and SH waves in MgO-doped and undoped PPLN.

RMS Noise (%)	Undoped PPLN		MgO-doped PPLN	
	Pump	SH	Pump	SH
Bulk	0.76	1.2	0.5	1.0
Waveguide	2.0	4.7	1.3	2.9

3. Experimental Results

3.1. SHG without Other Irradiation

First, we tested SHG from an undoped PPLN crystal at room temperature. For the bulk and waveguide PPLN, the fundamental and SH output powers exhibit certain fluctuations over the time as shown in Figure 3. To facilitate the comparison of noises under different conditions, the output powers are all normalized, that is, their average powers are scaled to unity. We can see that both fundamental and SH waves fluctuate with the time but at different amplitudes. Also, we can see that in both bulk and waveguide PPLN, the fluctuation amplitude of the fundamental wave is lower than that of the SH wave, and for each wave, its noise is higher in the waveguide PPLN than in the bulk.

The corresponding frequency spectra in the frequency range of 0–2 kHz, obtained by using the fast Fourier

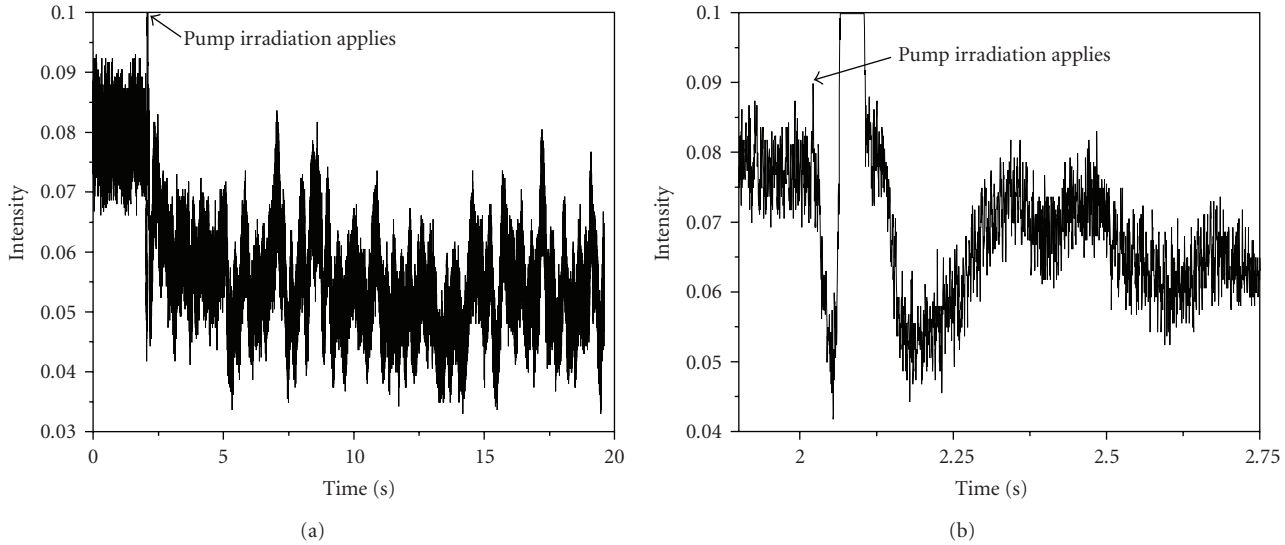

Figure 7: (a) Output SH power from undoped PPLN waveguide before and after 10 mW 532 nm irradiation, (b) detailed change of SH power near the switching point.

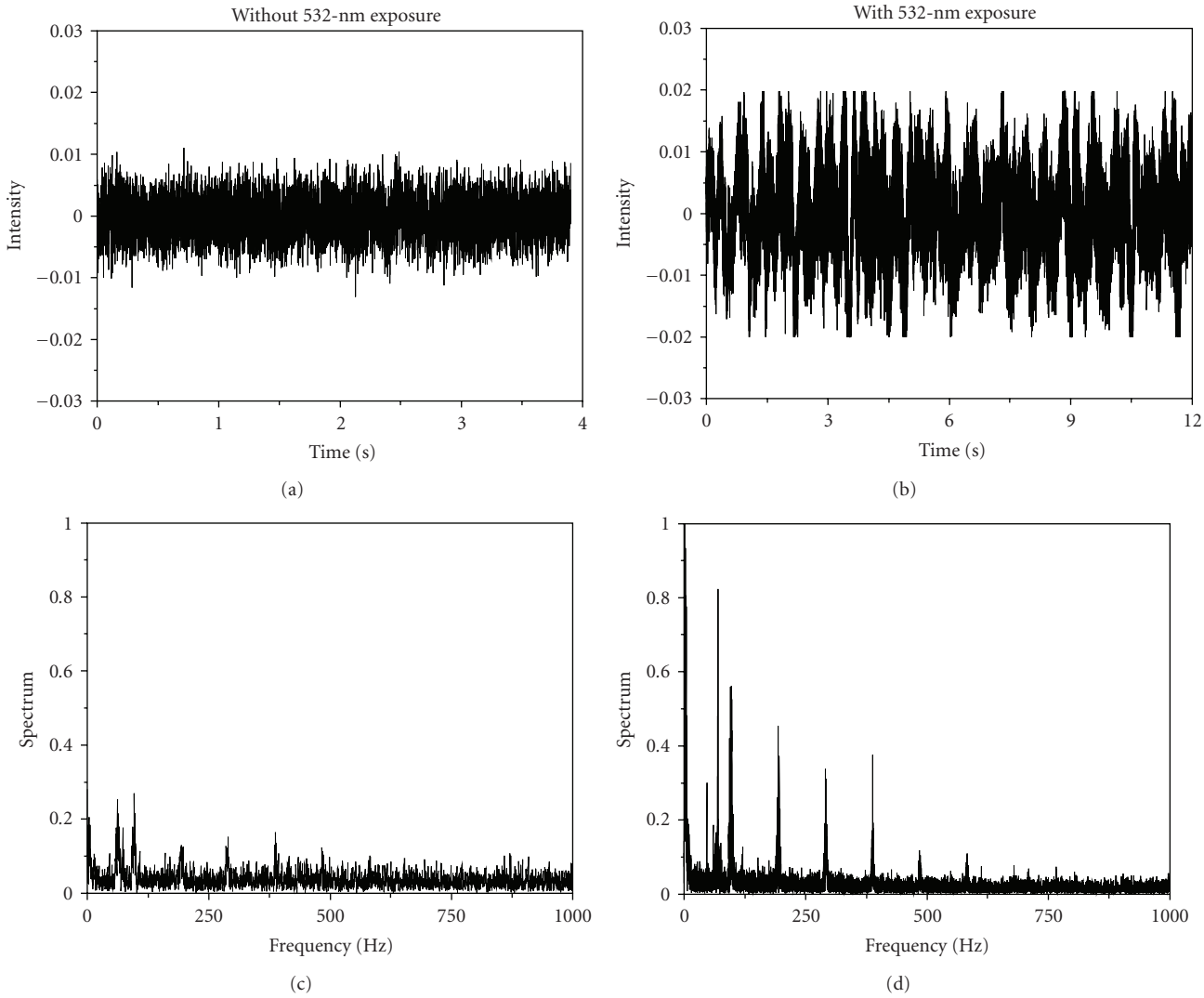

Figure 8: (a) (b) Noise characteristics of SHG in undoped PPLN waveguide with and without 532 nm irradiation. (c) (d) The normalized frequency spectra corresponding to the temporal traces in (a) and (b).

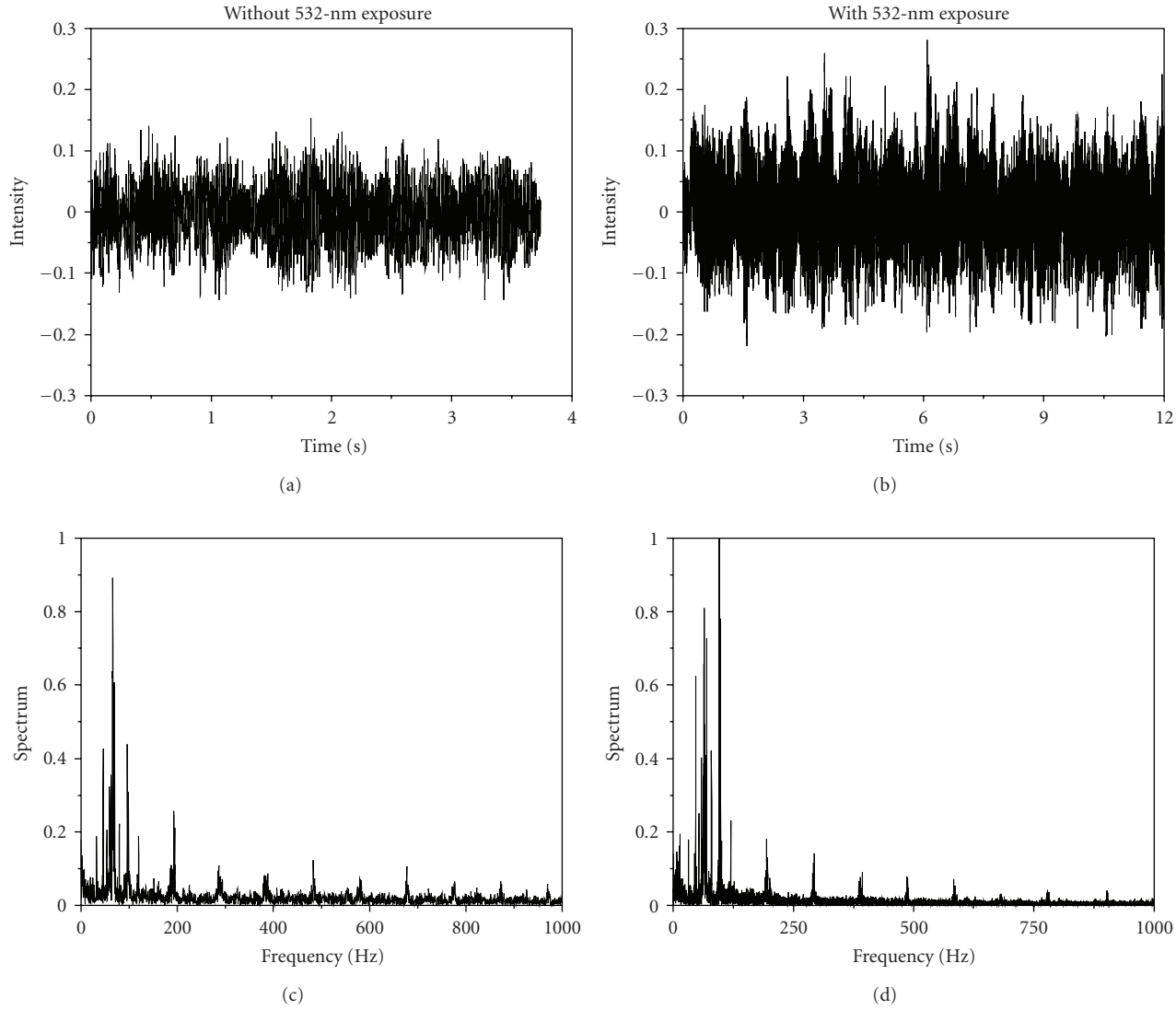

Figure 9: (a) (b) Noise characteristics of SHG in MgO-doped PPLN waveguide with and without 532 nm irradiation. (c) (d) The normalized frequency spectra corresponding to the temporal traces in (a) and (b).

transform (FFT), are shown in Figure 4. In the bulk and waveguide PPLN, the fundamental and SH waves exhibit different noise spectrum structures. In particular, the SH wave has more noise spectral components than the fundamental wave. As a result, the total noise power is higher in the SH wave than in the fundamental wave. It is known from the nonlinear interaction relationship of SHG that any instability of the fundamental wave can be enhanced in the SH wave.

Similarly for a 4.5 cm long MgO-doped PPLN crystal at room temperature, the temporal fundamental and SH output powers are depicted in Figure 5. The power fluctuations of the fundamental and SH waves in the MgO-doped PPLN crystal have the same trends as those in the undoped PPLN crystal (shown in Figure 3), but the fluctuation amplitude of each wave is lower in Figure 5 than its counterpart in Figure 3. This implies that SHG in the MgO-doped PPLN has lower noise than that in the undoped PPLN. The corresponding frequency spectra are shown in Figure 6.

To quantitatively describe the noise amplitude, we adopt root-mean-square (RMS) value here. The RMS values of the fundamental and SH temporal output traces (shown in Figures 3 and 5) are calculated and compared in Table 1. We can see that the SH noise intensity is nearly two times higher than its fundamental wave, the noise intensity in the waveguide is three times that in the bulk, and the noise in the MgO-doped PPLN is about 50% lower than that in the undoped PPLN.

The noise of the fundamental wave mainly results from the following aspects. First, the input wave from the tunable laser and power amplifier has certain noise, which usually exhibits the 1/f noise in the low-frequency range, and the Gaussian white noise in high-frequency range. Second, the

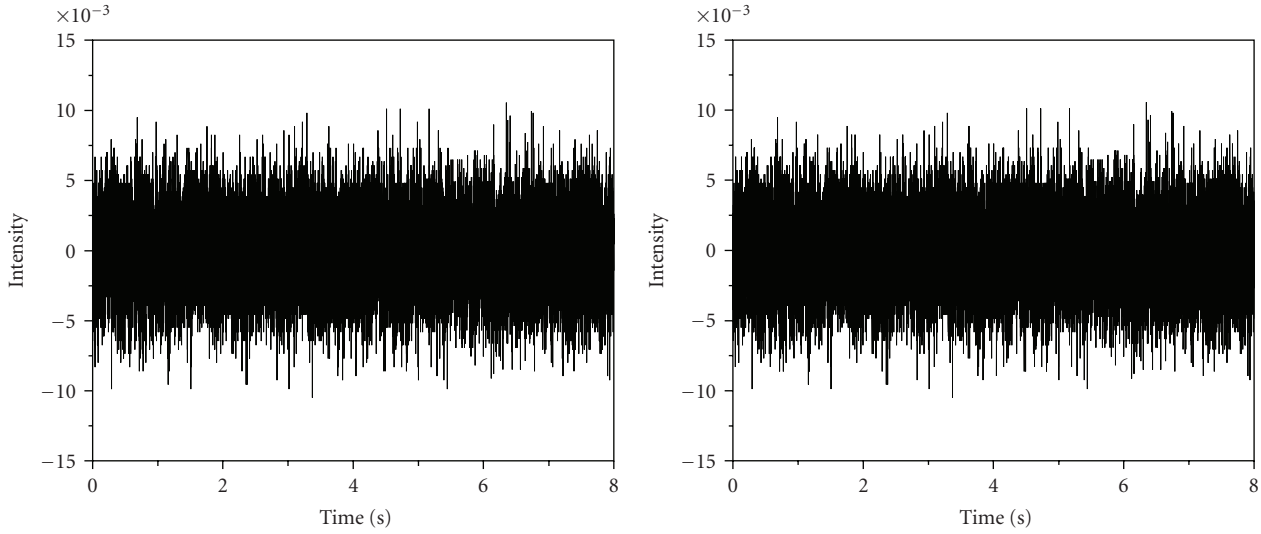

Figure 10: For undoped bulk PPLN, comparison of SH outputs with and without 532 nm irradiation.

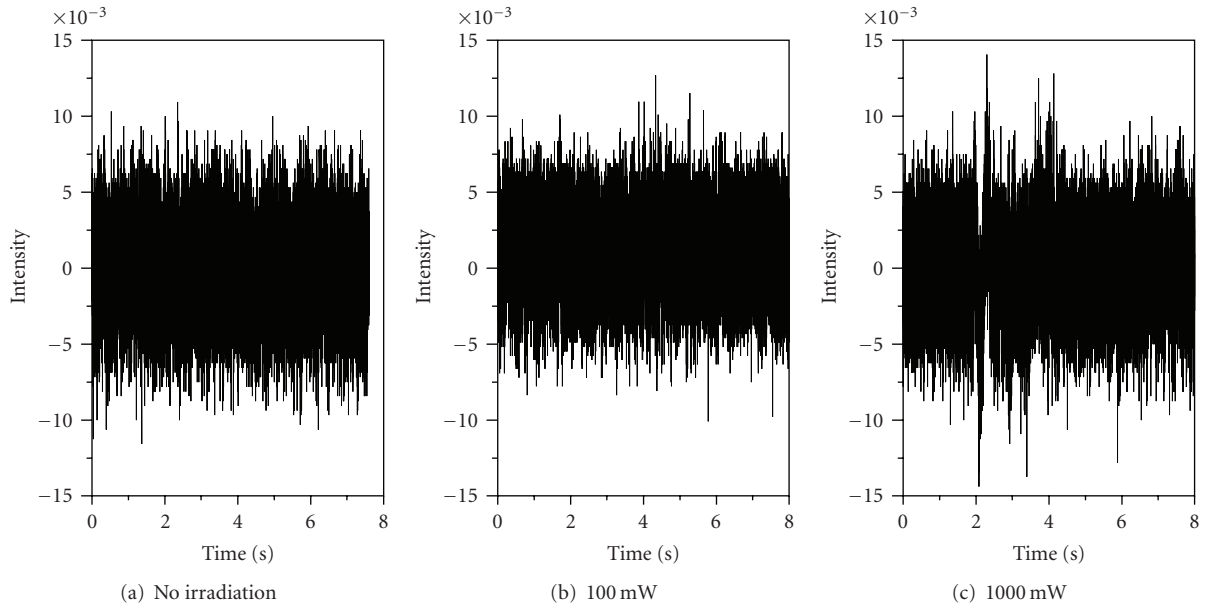

Figure 11: For MgO-doped bulk PPLN, comparison of SH outputs with different irradiation powers of 532 nm irradiation.

instability of the coupling between the fiber and device contributes to the low-frequency fluctuation of the output. Third, a change in the input polarization state of the device may change the output power. The second and third terms vary from time to time, and contribute some spikes in the noise spectrum (mainly in the low-frequency range). These are more significant in the waveguide device than in the bulk PPLN. In fact, the waveguide devices are more sensitive to optical and mechanical perturbations than the bulk devices. With these impacts, the SHG power is more unstable than the fundamental power as shown in Figures 3 and 5. Our experimental results are consistent with the previous observations [18, 19].

3.2. SHG with 532-nm Irradiation

We then investigated the noise characteristics of SHG in the MgO-doped and undoped PPLN crystals with the 532 nm irradiation. The experimental setup is shown in Figure 2.

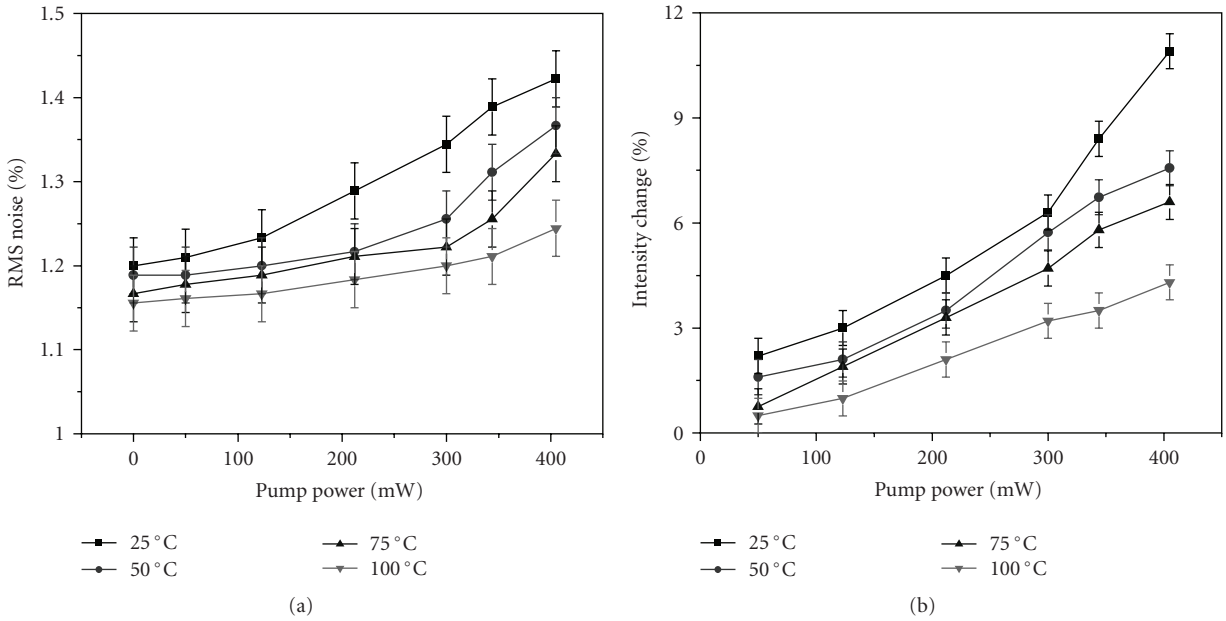

Figure 12: (a) RMS noise of SHG and (b) intensity change of SHG versus 1090 nm pump power, measured at different temperatures.

For the undoped PPLN waveguide, the results of output SH power are shown in Figure 7, where the 532 nm pump irradiation (10 mW) is applied to the PPLN waveguide at the time of 2 seconds. We can see in Figure 7(a) that after turning on the 532-nm pump irradiation, the SH output power exhibits an abrupt oscillation and then decreases quickly. The temporal trace becomes noisier with the 532 nm exposure than the case without the exposure. In Figure 7(b), the initial evolution of the SH power under the 532 nm exposure is depicted. There is an apparent undershoot followed by an overshoot when the 532 nm pump is applied. Thereafter, the SH power shows significant fluctuations. These are related to the photorefractive effect, [7–12] which cannot only change the efficiency of SHG but also increase noise in the SH wave.

The noise amplitudes and frequency spectra of the SH wave with and without the 532 nm pump are compared in Figure 8. The RMS value of noise in the case of the 532 nm exposure is about 2.3 times as high as that in the absence of the 532 nm exposure. From the corresponding frequency spectra shown in Figures 8(c) and 8(d), we can see that the 532 nm pump irradiation can increase noises mainly at a low-frequency range (<400 Hz).

For the MgO-doped PPLN waveguide, Figure 9 shows the noise amplitudes and frequency spectra of the SH wave with and without the 532 nm irradiation. The 532 nm pump power is 30 mW. The RMS noise value of the SH wave is increased by a factor of 1.48 under the 532 nm irradiation.

For the undoped bulk PPLN, the output SH trace is shown in Figure 10 with and without 100 mW 532 nm irradiation. There is no apparent change in noise amplitude. In fact, the ratio of the RMS values in these two cases is 1.02.

For the MgO-doped bulk PPLN, the noise characteristics are quite similar for different irradiation powers up to 1 W, as shown in Figure 11. The RMS noise is increased by 2% and 7% under 0.1- and 1.0-W irradiation, respectively. In addition, the average output power of the SH wave has nearly no change under the 532 nm exposure, which implies a good performance of SHG in MgO-doped bulk PPLN for high-power applications.

From the above experimental results, we can see that the undoped PPLN waveguide performs worst under the 532 nm irradiation in terms of SHG conversion efficiency and noise, while the SHG in the MgO-doped bulk is less sensitive to the 532 nm irradiation. The noise increase of the SH wave under the irradiation is related to photorefractive effect, which can change the refractive index in the optical path of light propagation. Such a change in the refractive index is somehow nonuniform in the PPLN, and may vary with both time and position, which can lead to temporal and spatial variations in the phase matching condition of SHG. In addition, other accompanying effects, such as thermal effect, optical scattering, and two-photon absorption can also affect the SH wave in the time domain.

3.3. SHG with 1090 nm Irradiation

Next, we tested the SHG in the previous undoped bulk PPLN under the 1090 nm irradiation. The RMS noise of SHG and its intensity change versus 1090 nm pump power are shown in Figure 12, respectively, at different temperatures. We can see in Figure 12(a) that on the one hand, similar to the previous 532 nm irradiation, the noise increases with an increase of 1090 nm pump power at any temperature; on the other hand, with an increase of device temperature, the noise tends to decrease. However, the amplitude of noise reduction is maximum 0.2%, which is not significant. In Figure 12(b),

with an increase of 1090 nm pump power, the increase of SHG intensity change is apparent. In particular, it is raised by four times when the applied pump power varies from 50 to 400 mW. In addition, an elevation of device temperature is helpful to alleviate the problems of noise and attenuation.

Similar results were observed for the MgO-doped bulk PPLN crystals. However, the influence of increased temperature is not as significant as that for the undoped PPLN crystals. In the waveguides, it is found that the noise increase and intensity variation are several times higher than those in the corresponding bulk crystals.

4. Conclusions

We have shown the noise characteristics of the SH waves in bulk and waveguide PPLN crystals. It is found that for the bulk and waveguide PPLN crystals, the noise or instability of the SH wave is higher than that of the fundamental wave. For the same fundamental wave, the SH wave tends to have lower noise in a bulk crystal than in a waveguide, and in MgO-doped PPLN than in undoped one. In particular, the corresponding RMS value of the noise amplitude in a waveguide can be two times higher than that in a bulk PPLN. In addition, the photorefractive effect incurred by the irradiation light can degrade the conversion performance in terms of SHG efficiency and noise intensity. In the pump-probe method with the pumping wavelengths of 532 and 1090 nm, both SHG noise and intensity vary with pump power. The 532 nm pump can bring a more significant influence than the 1090 nm one. In addition, increasing crystal temperature can alleviate the noise and absorption problems to some extent, which is more significant to undoped PPLN than to MgO-doped PPLN. The quantitative results obtained in this work provide some useful information for the applications of QPM PPLN devices for SHG.

Acknowledgments

The authors would like to thank the Ontario Photonics Consortium (OPC), the Materials and Manufacturing Ontario (MMO), the Photonics Research Ontario (PRO), the Natural Sciences and Engineering Council of Canada (NSERC), the Canada Foundation for Innovation (CFI) under the New Opportunities Program.

References

[1] Y. R. Shen, *The Principles of Nonlinear Optics*, John Wiley & Sons, New York, NY, USA, 1984.

[2] T. Suhara and M. Fujimura, *Waveguide Nonlinear-Optic Devices*, Springer, Berlin, Germany, 2003.

[3] M. M. Fejer, G. A. Magel, D. H. Jundt, and R. L. Byer, "Quasi-phase-matched second harmonic generation: tuning and tolerances," *IEEE Journal of Quantum Electronics*, vol. 28, no. 11, pp. 2631–2654, 1992.

[4] C.-Q. Xu, H. Okayama, and M. Kawahara, "1.5-μm band efficient broadband wavelength conversion by difference frequency generation in a periodically domain-inverted $LiNbO_3$ channel waveguide," *Applied Physics Letters*, vol. 63, no. 26, pp. 3559–3561, 1993.

[5] C.-Q. Xu, B. Zhou, Y. L. Lam, S. Arahira, Y. Ogawa, and H. Ito, "All-optical demultiplexing using $LiNbO_3$ quasiphase-matched wavelength converters," *Japanese Journal of Applied Physics*, vol. 40, no. 8, pp. L881–L883, 2001.

[6] Y. Nishida, H. Miyazawa, M. Asobe, O. Tadanaga, and H. Suzuki, "0-dB wavelength conversion using direct-bonded QPM-Zn: $LiNbO_3$ ridge waveguide," *IEEE Photonics Technology Letters*, vol. 17, no. 5, pp. 1049–1051, 2005.

[7] D. Eger, M. A. Arbore, M. M. Fejer, and M. L. Bortz, "High intensity illumination effects in $LiNbO_3$ and $KTiOPO_4$ waveguides," *Journal of Applied Physics*, vol. 82, no. 3, pp. 998–1005, 1997.

[8] A. M. Glass, "The photorefractive effect," *Optical Engineering*, vol. 17, no. 5, pp. 470–479, 1978.

[9] T. Fujiwara, X. Cao, R. Srivastava, and R. V. Ramaswamy, "Photorefractive effect in annealed proton-exchanged $LiNbO_3$ waveguides," *Applied Physics Letters*, vol. 61, no. 7, pp. 743–745, 1992.

[10] C.-Q. Xu, H. Okayama, and Y. Ogawa, "Photorefractive damage of $LiNbO_3$ quasiphase matched wavelength converters," *Journal of Applied Physics*, vol. 87, no. 7, pp. 3203–3208, 2000.

[11] M. Asobe, O. Tadanaga, T. Yanagawa, H. Itoh, and H. Suzuki, "Reducing photorefractive effect in periodically poled ZnO- and MgO-doped $LiNbO_3$ wavelength converters," *Applied Physics Letters*, vol. 78, no. 21, pp. 3163–3165, 2001.

[12] B. Chen, J. Fonseca-Campos, W. Liang, Y. Wang, and C.-Q. Xu, "Wavelength and temperature dependence of photorefractive effect in quasi-phase-matched $LiNbO_3$ waveguides," *Applied Physics Letters*, vol. 89, no. 4, Article ID 043510, 3 pages, 2006.

[13] B. Chen, C.-Q. Xu, B. Zhou, Y. Nihei, A. Harada, and Y. Wang, "Temperature characteristics of 1.5-μm-band MgO doped $LiNbO_3$ quasi-phase matched wavelength converters," *Japanese Journal of Applied Physics*, vol. 40, no. 6B, part 2, pp. L612–L614, 2001.

[14] Y. Wang, J. Fonseca-Campos, and C.-Q. Xu, "Picosecond-pulse wavelength conversion based on cascaded second-harmonic generation-difference frequency generation in a periodically poled lithium niobate waveguide," *Applied Optics*, vol. 45, no. 21, pp. 5391–5403, 2006.

[15] J. Fonseca-Campos, Y. Wang, B. Chen, et al., "40-GHz picosecond-pulse second-harmonic generation in an MgO-doped PPLN waveguide," *Journal of Lightwave Technology*, vol. 24, no. 10, pp. 3698–3708, 2006.

[16] Y. Wang and C.-Q. Xu, "Analysis of ultrafast all-optical OTDM demultiplexing based on cascaded wavelength conversion in PPLN waveguides," *IEEE Photonics Technology Letters*, vol. 19, no. 7, pp. 495–497, 2007.

[17] C.-Q. Xu, "Plasma/electrostatic ferroelectric material processing," in *Proceedings of the 4th Asia-Pacific International Symposium on the Basic and Application of Plasma Technologies (APSPT-4)*, pp. 49–53, Yunlin, Taiwan, December 2005.

[18] D.-W. Chen and T. S. Rose, "Low noise 10-W cw OPO generation near 3 μm in MgO doped PPLN," in *Proceedings of the Conference on Lasers and Electro-Optics (CLEO '05)*, vol. 3, pp. 1829–1831, Baltimore, Md, USA, May 2005.

[19] H. K. Nguyen, C. Zah, M. H. Hu, et al., "107-mW low-noise green light emission by frequency doubling of reliable 1060-nm DFB semiconductor laser diodes," in *Proceedings of the International Conference on Quantum Electronics and the Pacific Rim Conference on Lasers and Electro-Optics (IQEC/CLEO-PR '05)*, Tokyo, Japan, July 2005.

Hindawi Publishing Corporation
Advances in OptoElectronics
Volume 2008, Article ID 587091, 6 pages
doi:10.1155/2008/587091

Research Article

Detection of an Optical Signal Using Difference Frequency Generation in a Periodically Poled $LiTaO_3$ Microwave Waveguide

Hiroshi Murata and Yasuyuki Okamura

Graduate School of Engineering Science, Osaka University, 1-3 Machikaneyama, Toyonaka, Osaka 560-8531, Japan

Correspondence should be addressed to Hiroshi Murata, murata@ee.es.osaka-u.ac.jp

Received 9 June 2008; Accepted 25 August 2008

Recommended by Chang-qing Xu

The detection of an optical signal modulated at 15 GHz was demonstrated experimentally by using difference frequency generation based on a second-order nonlinear optical effect in a periodically poled $LiTaO_3$ microwave rectangular waveguide. The measured frequency dependence of the generated microwave signal was in good agreement with the theoretically expected result. An interesting application of the proposed device is the detection of high-speed optical clock detection.

1. Introduction

The detection of a high-speed optical signal is indispensable in many optoelectronic systems. The operational principle of standard photodetectors is based on the generation of photocarriers by the injection of an optical signal into a semiconductor/metal, where detected signals are obtained as a photocurrent according to the envelope of the injected optical signal to the detectors. Therefore, amplitude/intensity-modulated optical signals can be detected directly. However phase/frequency-modulated optical signals cannot. The speed of standard photodetectors is limited by the transit time of the photocarriers through the device or an RC time constant. Therefore, detection efficiency decreases as optical signal frequency increases, and signal detection modulated at high frequency ranges over millimeter-waves is rather difficult except for specifically tailored ultra-fast detectors like the unitraveling-carrier photodiode (UTC-PD) [1].

Difference frequency generation (DFG) based on a second-order nonlinear optical effect is another candidate for the detection of a high-speed optical signal [2–4]. Using DFG, it is possible to shift the spectrum of a modulated optical signal from lightwave frequency ranges to micro-/millimeter-wave frequency ranges directly. Therefore, not only amplitude/intensity-modulated optical signals, but also phase/frequency-modulated signals are applicable. In next generation optical fiber communication networks, several types of advanced vector modulation signals (frequency shift keying (FSK)/phase shift keying (PSK)/amplitude and phase shift keying (APSK)) are important for extremely high-bit-rate data transfer. The DFG technique is applicable to the conversion of optical FSK/PSK/APSK signals, which are hard to detect directly using conventional photocurrent based devices. The conversion of optical orthogonal frequency-division multiplexing (OFDM) signals to a microwave frequency range is also possible by using the DFG technique.

Several studies on signal generation/conversion based on DFG from a second-order nonlinear optical effect have been reported [2–4]. However, the conversion efficiency is low due to the difficulty of phase matching which comes from the differences in the velocities between the lightwaves and the micro-/millimeter waves. Furthermore, the Manley-Rowe relationship, which expresses the difference in the photon energy between lightwaves and micro-/millimeter waves [5], causes even lower output power.

In this paper, we present the detection of an optical signal modulated at a microwave frequency using DFG in periodically-poled $LiTaO_3$ with a microwave resonator structure composed of a straight microwave waveguide. In order to obtain high conversion efficiency, a periodically poled structure of ferroelectric optical crystal is adopted for quasi-phase-matching (QPM) between the lightwave and the microwave. The microwave Fabry-Perot resonator is also utilized for the enhancement of the output signal

by the resonance effect. This device has the following advantages: it has a simple structure, only the optical signal at the target frequency is converted, the other optical signals including an optical carrier can pass through the device without disturbance, peak detection frequency can be tailored by tuning the polarization reversal period and the resonance condition, and the signal conversion efficiency becomes greater at higher frequencies unlike conventional photodetectors.

In the following sections, the device structure, analysis, design, and experimental results of the proposed device are presented.

2. Device Structure

Figure 1 shows the structure of the DFG-based optical signal detection device we have proposed. $LiTaO_3$ is adopted as a nonlinear optical material for DFG. $LiNbO_3$ or other ferroelectric optical crystals with second-order optical nonlinearity are also applicable. The surfaces of the four sidewalls of the long rectangular $LiTaO_3$ crystal are covered with a thin metal film in order to construct a microwave rectangular waveguide. Both ends of the rectangular $LiTaO_3$ crystal are uncovered for light beam coupling and microwave output. A channel optical waveguide structure is also applicable for confining and guiding lightwaves along the crystal. The $LiTaO_3$ crystal is periodically poled for QPM between the lightwave and the microwave. By DFG in the $LiTaO_3$ crystal, a microwave signal is generated when the modulation frequency of the input optical signal coincides with the designed frequency determined by the poling period and the microwave resonance condition.

Periodic poling structure is designed for QPM between the modulated lightwave and the generated microwave. In DFG for optical signal detection, the frequency difference between the two lightwaves, which corresponds to the frequency of the generated microwave, is rather small compared with their individual frequencies. Therefore, the quasi-velocity-matching (QVM) scheme between the light group velocity and the microwave phase velocity [6] is useful for the design of the poling period for the QPM.

The structure of the microwave resonator is just a Fabry-Perot cavity. Since the refractive index value of $LiTaO_3$ in the microwave frequency range is rather large (~6.5) compared with air, about half of the microwave signal generated through DFG in the $LiTaO_3$ crystal is reflected at both ends of the microwave rectangular waveguide and propagates backwards and forwards in it. As a result, the Fabry-Perot cavity can be constructed without specific mirrors/reflectors in the microwave frequency ranges.

3. Analysis and Design

In the DFG shown in Figure 1, the coupling between the two lightwave modes, with angular frequencies ω_1 and ω_2, and the microwave mode of ω_3 propagating to the $+y$ direction is described by using coupled-mode equations assuming the slowly varying amplitude approximation [5]

$$\begin{aligned} j\frac{dA_1}{dy} &= \kappa_1 \Gamma A_2 A_3 \exp\left[-j(\beta_2+\beta_3-\beta_1)y\right], \\ j\frac{dA_2}{dy} &= \kappa_2 \Gamma A_1 A_3^* \exp\left[-j(\beta_1-\beta_3-\beta_2)y\right], \\ j\frac{dA_3}{dy} &= \kappa_3 \Gamma A_1 A_2^* \exp\left[-j(\beta_1-\beta_2-\beta_3)y\right], \end{aligned} \tag{1}$$

where A_1, A_2, and A_3 are the complex amplitudes of the electric field of each mode, κ_1, κ_2, and κ_3 are the coupling constants determined by the nonlinear coefficient of the crystal and the polarization of the three modes, Γ is the parameter defined by the overlap of the field distribution of the three modes, and β_1, β_2, and β_3 are the phase constants of the three modes.

The key point of the device design is to utilize a single guided-mode structure for the output microwave signal at the designed frequency. If there are several microwave guided modes or radiation modes in the device at the designed frequency range, the nonlinear polarization induced by the second order nonlinear optical effect might be simultaneously coupled to several modes propagating with different phase constants. Then, the generated signal by DFG might be spread out over these modes, and it is difficult to obtain high conversion efficiency.

Here, we set A_3 as the mode in the microwave frequency range and introduce a microwave waveguide with a rectangular structure. Adopting the periodically poled structure, the sign of the three coupling constants (κ_1, κ_2, and κ_3) is modulated along the propagation direction. Therefore, the phase-mismatching among the three modes can be compensated for and high-efficiency coupling can be obtained. The length, L, of each polarization-reversed/nonreversed region to realize efficient DFG for the microwave at angular frequency $\omega_3 = \omega_1 - \omega_2 = 2\pi f_m$ is expressed by the following equation:

$$\begin{aligned} L &= \frac{\pi}{|\beta_1-\beta_2-\beta_3|} \\ &\approx \frac{\pi}{|(\partial\beta/\partial\omega)(\omega_1-\omega_2)-\beta_3|} \\ &= \frac{\pi}{|(n_g/c)\omega_3-(n_m/c)\omega_3|} \\ &= \frac{c}{2f_m(n_m-n_g)}, \end{aligned} \tag{2}$$

where n_g is the group index of the lightwaves which is expressed by $n_g = c(\partial\beta/\partial\omega)$, n_m is the effective index of the microwave mode in the rectangular waveguide, and c is the lightwave velocity in vacuum. This final transformed equation is equivalent with the QVM condition in traveling-wave electro-optic modulators [6].

It is clear from (2) that there is an optimum detection frequency for the poling period. Therefore, the proposed detection device is a band-operating device. The frequency

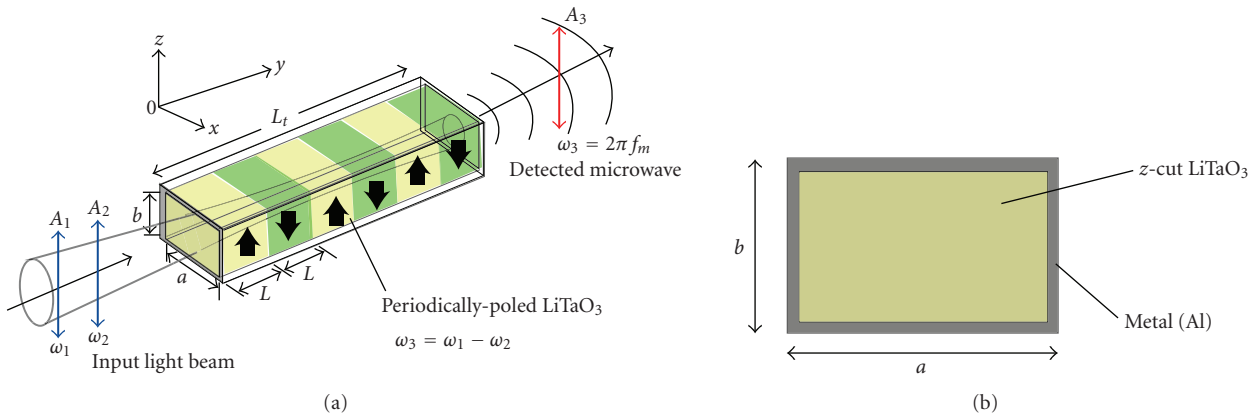

FIGURE 1: Basic structure of the optical signal detection device with periodically poled structure and microwave rectangular waveguide. The whole structure is (a), and its cross sectional view is (b).

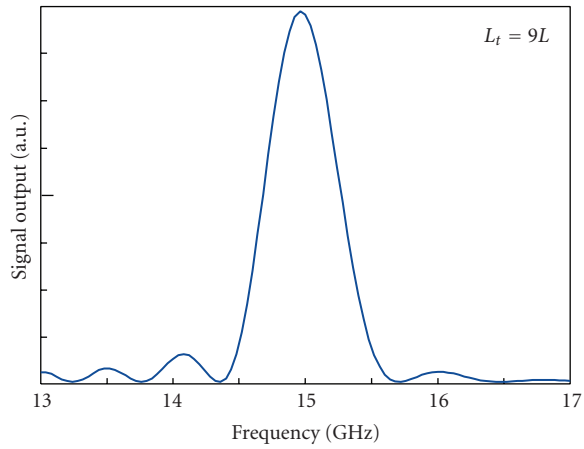

FIGURE 2: Calculated frequency dependence by the QPM.

response of the signal detection determined by the QPM can be calculated using the coupled-mode equation (1) taking into account the reversal of the sign of the coupling coefficient by polarization reversal. The calculated example is shown in Figure 2, where the total device length, L_t, was set as $L_t = 9L$. The QPM bandwidth is inversely proportional to the total device length L_t. The frequency response of the proposed device is also dependent on the resonance condition of the Fabry-Perot cavity structure. Therefore, the final frequency response is determined by the multiplication of the response by the QPM shown in Figure 2 and the response by the Fabry-Perot resonator.

In order to utilize the largest nonlinear coefficient of the $LiTaO_3$ crystal, d_{33}, a z-cut $LiTaO_3$ crystal substrate was adopted and the z-axis of the crystal was set parallel to the shorter side in the cross-section. Under this configuration, the polarization directions of the two lightwave modes that we set were the same and parallel to the z-axis. Therefore, the generated microwave by the DFG with the d_{33} nonlinear coefficient was polarized along the z-axis. This means that the TE guided mode in the microwave rectangular waveguide can be obtained. The calculated dispersion relationship of the TE_{10} mode is shown in Figure 3. By setting the length of the shorter side of the crystal to an appropriate value, the microwave rectangular waveguide only supports a TE_{10} mode in the designed frequency range and a high-efficiency DFG signal generation can be expected.

4. Experiments

The prototype device was fabricated using a z-cut $LiTaO_3$ substrate. First, a periodically poled structure was fabricated in a 0.4 mm thick crystal substrate by use of the pulse voltage applying method. The period of the poling, $2L$, was set to 10.2 mm, where the designed lightwave wavelength was 1550 nm (the group index of the extraordinary light is $n_g = 2.17$) and the peak detection frequency was 15 GHz using a microwave rectangular waveguide, with a cross-section of 2.0×0.4 mm (the effective index of the TE_{10} mode is $n_m = 4.13$ at 15 GHz). Next, the periodically poled crystal was cut with a diamond saw to 45.9 mm along the propagation direction and 2.0×0.4 mm in cross-section, which was designed for the cutoff frequency of the microwave rectangular waveguide at 11.6 GHz and for a single-mode structure with a frequency range from 11.6 GHz to 23.1 GHz. After cutting, both ends of the crystal were polished. Finally, a 2 μm thick Al film was deposited on the four sidewalls of the crystal by use of electron-beam vapor deposition.

The microwave resonance characteristics of the fabricated device were measured by use of a pair of microwave probe antennas and a network analyzer. The measured microwave transfer characteristic through the fabricated device is shown in Figure 4. The resonance peaks in a Fabry-Perot cavity were clearly observed. The measured separation of the adjoining resonance frequency, Δf, was $\Delta f \sim 1$ GHz around 15 GHz, which was in good agreement with the calculated value from the following equation:

$$\Delta f = \frac{c}{2 L_t n_m}, \tag{3}$$

where c is the lightwave velocity in vacuum, L_t is the total length of the device, and n_m is the effective index of

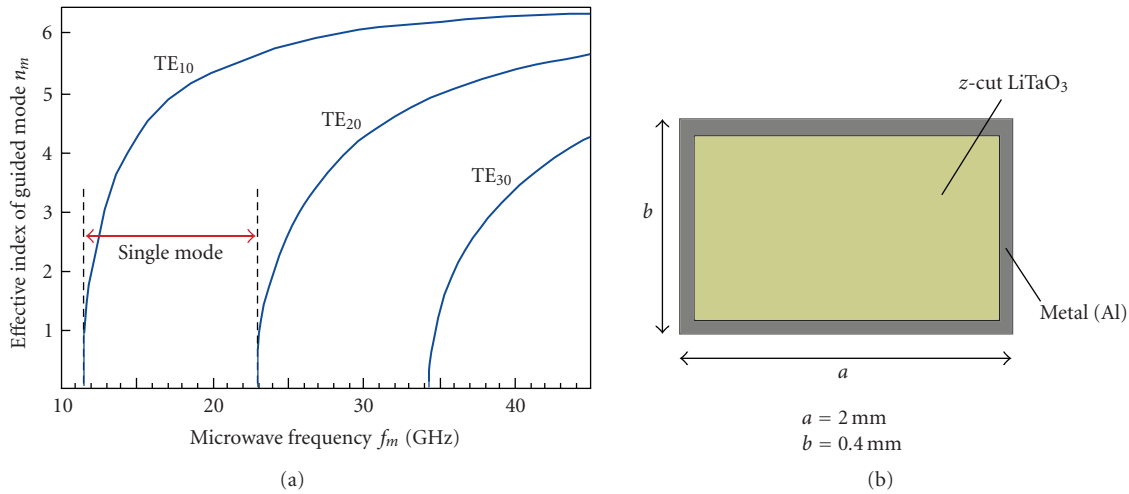

Figure 3: Calculated dispersion characteristics of the guided modes in the $LiTaO_3$ microwave rectangular waveguide with $a = 2$ mm and $b = 0.4$ mm.

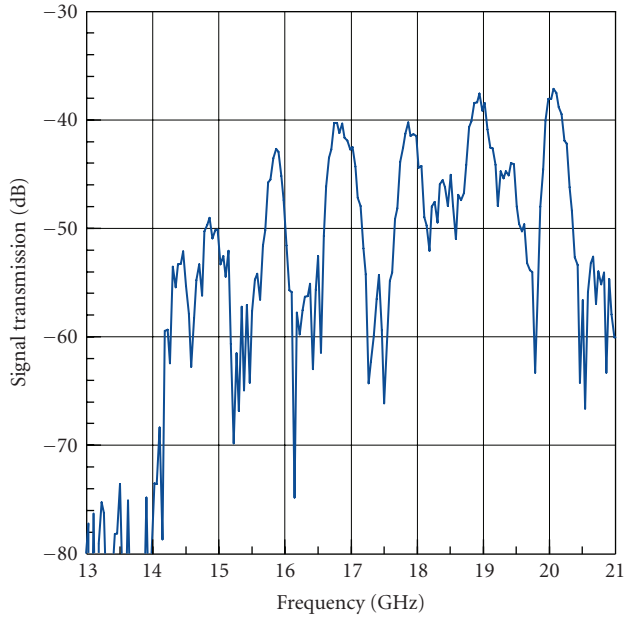

Figure 4: Measured microwave resonance characteristics of the fabricated device.

the microwave TE_{10} mode propagating in the rectangular waveguide, which was calculated as ~4 in the designed frequency range. Therefore, a single-mode microwave propagation characteristic in the designed frequency range was confirmed experimentally. The measured unloaded Q-factor around each resonance frequency was ~50. In Figure 4, the transmission signal is rather small below 14 GHz, which was due to the cutoff characteristics of the microwave probe antennas used in the measurement.

The experimental setup for optical signal detection is shown in Figure 5. The light source was a 1550 nm CW DFB laser diode. The CW lightwave from the laser diode was deeply modulated by use of a high-speed optical intensity modulator with a driving modulation frequency from 13 GHz to 18 GHz and amplified by use of an Erbium-doped optical fiber amplifier. The intensity modulated lightwave with a power of 20 mW was focused on the end surface of the fabricated device using a lens of a 50 mm in focal length. The output microwave signal, which was emitted from the end of the DFG device, was measured using a microwave horn antenna and a microwave spectrum analyzer. An example of the detected signal spectrum is shown in Figure 6. A clear signal was observed at 15.1 GHz. The measured frequency response of the detected signal is shown in Figure 7. The peak detection frequency was 15.1 GHz, which was in good agreement with the expected characteristics calculated from the frequency response by the QPM (Figure 2) and the measured microwave resonance characteristics of the fabricated device (Figure 4). The detected signal power level (~0.1 pW) was comparable with the estimated value using the d_{33} nonlinear coefficient of $LiTaO_3$, the microwave frequency, the light wavelength, the device length and cross-section, the unloaded Q-factor of the Fabry-Perot resonator, and the coupling efficiency between the device and the horn antenna used in the measurement.

5. Discussion and Conclusion

In the experiment, the coupling between the DFG device and the microwave horn antenna was small (< -10 dB), since the radiated microwave from the device rapidly spread out from the end of the rectangular waveguide with a small cross-section of 2.0×0.4 mm, which is rather small compared with the wavelength of the emitted microwave in air of 20 mm. By using an appropriate microwave circuit for increasing the coupling efficiency such as a microwave lens or a large aperture array of antennas, we expect to enhance the output power by ~10 dB. The application of an optical waveguide structure is also attractive for increasing the conversion efficiency with diffraction-less light propagation over a long interaction length. It should be noted that the output power

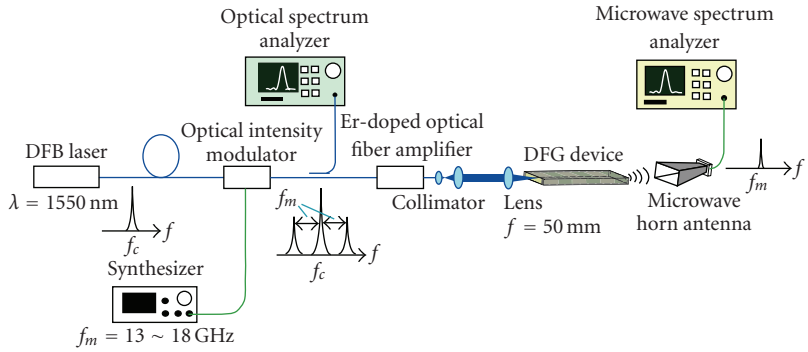

Figure 5: Experimental setup for the detection of an optical signal modulated at ~15 GHz.

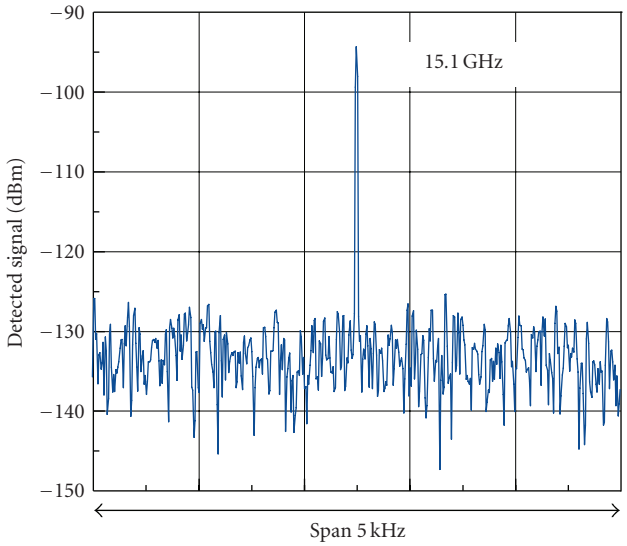

Figure 6: Measured spectrum of the detected signal. The modulation frequency was 15.1 GHz and the input lightwave power was 20 mW.

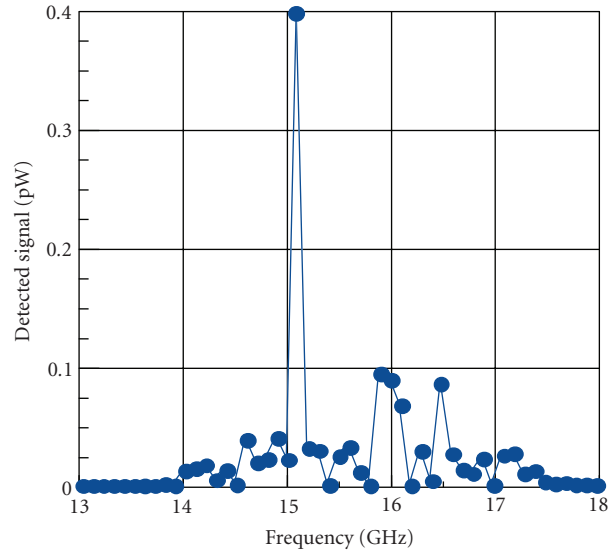

Figure 7: Measured frequency dependence of the detected signal with the input lightwave power of 20 mW.

level of the detected signal is proportional to the square of the signal frequency. Therefore, as the signal frequency becomes higher, the larger conversion efficiency is obtainable. By increasing the output power with these techniques, it is expected that the detection of optical clock signals at a high-repetition frequency without disturbance from other data signals would be obtainable. This would be useful for the next generation optical communication networks.

An optical heterodyne scheme injecting another phase-locked laser beam to the DFG device is also applicable for converting the signal to other frequency ranges, which is useful for extracting subcarrier multiplexed signals in orthogonal frequency-division multiplexing (OFDM) schemes or radio-on-fiber (ROF) systems.

Acknowledgments

The authors thank Drs. Akira Enokihara and Hidehisa Shiomi for their valuable advice and Toshiki Iwai and Ngo Quang Hong for their help with the analysis and the experiments. This work was supported in part by the Grants-in-Aid for Scientific Research from the Ministry of Education, Science, Sports and Culture, Japan.

References

[1] T. Ishibashi, S. Kodama, N. Shimizu, and T. Furuta, "High-speed response of uni-traveling-carrier photodiodes," *Japanese Journal of Applied Physics*, vol. 36, no. 10, pp. 6263–6268, 1997.

[2] K. Kawase, M. Sato, T. Taniuchi, and H. Ito, "Coherent tunable THz-wave generation from $LiNbO_3$ with monolithic grating coupler," *Applied Physics Letters*, vol. 68, no. 18, pp. 2483–2485, 1996.

[3] T. Hori, K.-H. Park, T. Kawanishi, and M. Izutsu, "Generation of CW millimeter wave signals in a lithium niobate nonlinear optical waveguide using modulated optical input," *Japanese Journal of Applied Physics*, vol. 39, no. 7A, pp. L667–L669, 2000.

[4] K. Suizu, T. Shibuya, S. Nagano, et al., "Pulsed high peak power millimeter wave generation via difference frequency generation using periodically poled lithium niobate," *Japanese Journal of Applied Physics*, vol. 46, part 2, no. 36–40, pp. L982–L984, 2007.

[5] A. Yariv, *Quantum Electronics*, John Wiley & Sons, New York, NY, USA, 3rd edition, 1989.

[6] H. Murata, A. Morimoto, T. Kobayashi, and S. Yamamoto, "Optical pulse generation by electrooptic-modulation method and its application to integrated ultrashort pulse generators," *IEEE Journal on Selected Topics in Quantum Electronics*, vol. 6, no. 6, pp. 1325–1331, 2000.

Hindawi Publishing Corporation
Advances in OptoElectronics
Volume 2008, Article ID 948294, 8 pages
doi:10.1155/2008/948294

Research Article

Electrooptic Modulators with Controlled Frequency Responses by Using Nonperiodically Polarization-Reversed Structure

Ha Viet Pham, Hiroshi Murata, and Yasuyuki Okamura

Graduate School of Engineering Science, Osaka University, Machikaneyama, Toyonaka, Osaka 560-8531, Japan

Correspondence should be addressed to Ha Viet Pham, havietpham@ec.ee.es.osaka-u.ac.jp

Received 20 June 2008; Accepted 2 September 2008

Recommended by Chang-qing Xu

We discuss a new method to design traveling-wave electrooptic modulators with controlled frequency responses using nonperiodically polarization-reversed structure. Using our method, the frequency responses of both magnitude and phase of modulation index are controllable. Several electrooptic modulators for advanced modulation formats such as duobinary modulation and wideband single-sideband modulation are proposed.

1. Introduction

High-speed traveling-wave electrooptic modulators are very important devices because of their applications in many optoelectronic fields, such as telecommunication, optical signal processing, and optical measurement. With the increasing demand for broadband communication, many studies on the high-speed electrooptic modulators have been carried out for optical fiber communication system [1]. In addition, the precise control of the frequency responses of high-speed electrooptic modulators has been required for the new generation optical fiber communication systems [2–4]. In a standard traveling-wave electrooptic modulator, the frequency response of the modulation index is restricted by two effects: the velocity mismatching between the lightwave and modulation microwave and the loss of modulation microwave in the traveling-wave electrodes.

The polarization reversal technology of ferroelectric optical crystals, such as $LiNbO_3$ and $LiTaO_3$, is attractive for realizing high-performance electrooptic modulators. We have developed traveling-wave electrooptic modulators utilizing the periodically polarization-reversed structure for quasi-velocity-matching (QVM) between the lightwave propagating in the optical waveguide and the modulation microwave traveling along the electrodes. This technique is attractive because it compensates for the velocity mismatch in the high frequency ranges without the requirement of specific and fine structures of the optical waveguide and the electrodes for velocity matching. Several advanced electrooptic modulators using periodically polarization-reversed structure have been proposed and demonstrated, such as a QVM electrooptic phase modulator [5], an electrooptic single-sideband (SSB) modulator [6], and an optical frequency shifter [7]. The bandwidth of the modulation frequency response in these electrooptic modulators with the simple periodically polarization-reversed structure is inversely proportional to its electrode length and becomes relatively narrow for a long-electrode device.

We have proposed a design to realize the traveling-wave electrooptic modulators utilizing nonperiodically polarization-reversed structures [8]. Using the proposed design, it is possible to obtain electrooptic modulators with the arbitrary frequency responses of the magnitude of the modulation index over a specified frequency range. The flat broadband electrooptic modulator with the compensation for the degradation by both velocity mismatch and the microwave loss is obtained. However, the control of not only the magnitude but also the phase of the modulation index is very important in order to design the electrooptic modulators for advanced modulation formats.

In this paper, we extend our design method to control frequency responses of both the magnitude and the phase of modulation index in electrooptic modulators with nonperiodically polarization-reversed structures utilizing

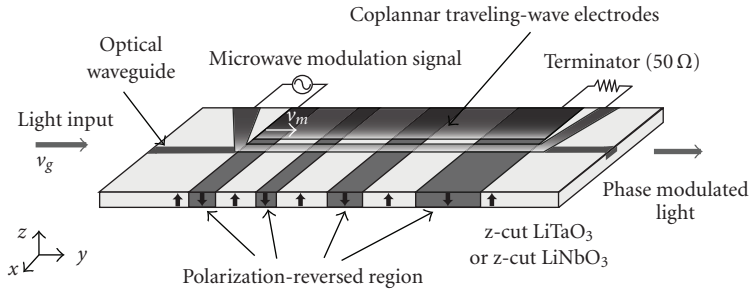

Figure 1: Basic structure of traveling-wave electrooptic phase modulator with nonperiodically polarization-reversed structure.

new flatness parameters. This new approach is applicable to the electrooptic modulators for advanced modulation formats, such as duobinary modulation or broadband single-sideband modulation. This paper is organized as follows. In Section 2, the basic structure of the electrooptic phase modulator using the nonperiodic polarization reversal and the frequency responses of modulation index are presented. In Section 3, the calculation method to control the frequency responses of both the magnitude and the phase of the modulation index is described. Several calculation results are shown in Section 4. In Section 5, the designs of the duobinary modulator and broadband single-sideband modulator with nonperiodically polarization-reversed structure are discussed.

2. Traveling-Wave Electrooptic Modulators with Polarization-Reversed Structure

A schematic of the basic structure of the traveling-wave electrooptic modulator is shown in Figure 1. It consists of a single-mode channel waveguide and simple coplanar traveling-wave electrodes fabricated on a ferroelectric substrate. A Mach-Zehnder waveguide for intensity modulation is also applicable. The velocity mismatch between the group velocity of the lightwave propagating in the optical waveguide and the phase velocity of a modulation microwave traveling along the electrodes is compensated for by adopting the periodic polarization reversal scheme [9]. The domain length L of a standard QVM with the periodic polarization reversal scheme is determined as follows:

$$L = \frac{1}{2f_m(1/v_m - 1/v_g)}, \tag{1}$$

where f_m is the peak modulation frequency, v_m is the phase velocity of the modulation microwave traveling along the electrodes, and v_g is the group velocity of the lightwave propagating in the waveguide. The parameter v_m can be calculated from the effective dielectric constant of the coplanar traveling-wave electrodes taking account of its structure. The parameter v_g can be derived from both the material dispersion of the refractive index of the ferroelectric material substrate and the mode dispersion of the optical waveguide.

The nonperiodic polarization reversal scheme is used to control the frequency response of the electrooptic modulation. Figure 2 shows the structure of the nonperiodic polarization reversal. The total active length for modulation is L_t. It is divided into M sections of successive polarization-reversed and nonreversed region. Each domain length is L_i $(i = 1, 2, \ldots, M)$.

The modulation index $\Delta\phi(f)$, which is a function of the modulation microwave frequency f, is calculated using the following equation:

$$\begin{aligned}\Delta\phi(f) = &-\int_0^{y_1} k\Delta n\, dy + \int_{y_1}^{y_2} k\Delta n\, dy \\ &- \cdots + (-1)^M \int_{y_{M-1}}^{y_M} k\Delta n\, dy,\end{aligned} \tag{2}$$

where k is the wave vector of the lightwave in vacuum and Δn is the refractive index change by the Pockels effect. When the light polarization is along the z-axis and the modulation electrical field is also along the z-axis, the refractive index change induced by the electrical field of the microwave at the position y $(0 \le y \le L_t)$ is derived as follows, taking account of the velocity mismatch between the lightwave and the modulation wave,

$$\begin{aligned}\Delta n(y) = &\frac{1}{2} n_e^3 r_{33} \frac{V}{d} \Gamma \exp(-\alpha y) \\ &\times \exp\left[j2\pi f \left\{ t_0 - \left(\frac{1}{v_m} - \frac{1}{v_g} \right) y \right\} \right],\end{aligned} \tag{3}$$

where n_e is the extraordinary ray refractive index of the substrate, r_{33} is the Pockels coefficient of the substrate. V is the voltage applied to the electrodes, d is the gap between the electrodes, Γ is the overlap factor between the optical field and the electrical field, α is the attenuation coefficient of the electrical field of the modulation microwave, and t_0 is the time when the lightwave arrived at the position $y = 0$.

3. Control of Frequency Response

When tuning the length of each domain, the frequency responses of the modulation index magnitude $|\Delta\phi(f)|$ and phase $\arg[\Delta\phi(f)]$ change. In order to design a nonperiodic polarization reversal structure for an arbitrary frequency

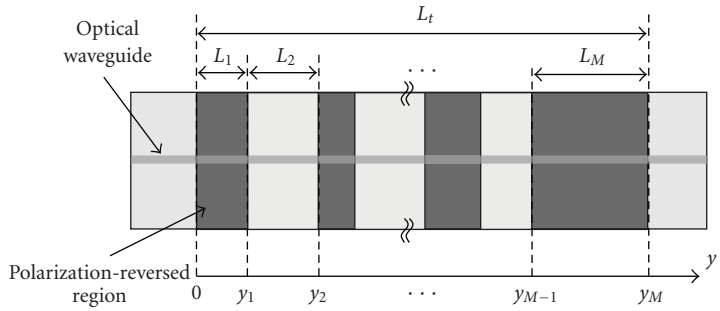

Figure 2: Nonperiodically polarization-reversed structure.

response of the modulation index magnitude, we have proposed the modified flatness parameter MF [8], which expresses the difference between the magnitude of the modulation index $|\Delta\phi(f)|$ and the target function $\mathrm{TF}(f)$ in the defined frequency range from f_1 to f_2

$$\mathrm{MF} = \frac{(f_2 - f_1)\int_{f_1}^{f_2} |\Delta\phi(f)/\mathrm{TF}(f)|^2 df}{\left[\int_{f_1}^{f_2} |\Delta\phi(f)/\mathrm{TF}(f)|\, df\right]^2} - 1. \tag{4}$$

By tuning the length of each domain, the value of the modified flatness parameter changes. If the modified flatness parameter becomes zero, the magnitude of the modulation index and the target function completely coincide in the frequency range.

We extended this method for dealing with both the modulation index magnitude and the phase. We define two flatness parameters, MF_M and MF_P, for the magnitude and the phase of the modulation index by using two target functions: $\mathrm{TF}_M(f)$ for the magnitude and $\mathrm{TF}_P(f)$ for the phase in the defined frequency range from f_1 to f_2, as follows:

$$\mathrm{MF}_M = \frac{(f_2 - f_1)\int_{f_1}^{f_2} (|\Delta\phi(f)|^2/|\mathrm{TF}_M(f)|^2) df}{\left[\int_{f_1}^{f_2} (|\Delta\phi(f)|/|\mathrm{TF}_M(f)|) df\right]^2} - 1,$$

$$\mathrm{MF}_P = \frac{(f_2 - f_1)\int_{f_1}^{f_2} (|\arg[\Delta\phi(f)]|^2/|\mathrm{TF}_P(f)|^2) df}{\left\{\int_{f_1}^{f_2} (|\arg[\Delta\phi(f)]|/|\mathrm{TF}_P(f)|) df\right\}^2} - 1, \tag{5}$$

where MF_M is the difference between the magnitude of the modulation index $|\Delta\phi(f)|$ and $\mathrm{TF}_M(f)$, and MF_P is the difference between the phase of the modulation index $\arg[\Delta\phi(f)]$ and $\mathrm{TF}_P(f)$.

If the modified flatness parameter MF_M becomes zero, the magnitude of the modulation index $|\Delta\phi(f)|$ and the target function $\mathrm{TF}_M(f)$ completely coincide in the defined frequency range. And if the modified flatness parameter MF_P becomes zero, the phase of the modulation index $\arg[\Delta\phi(f)]$ and the target function $\mathrm{TF}_P(f)$ completely coincide in that defined frequency range. We tried to find the condition for minimizing the two flatness parameters MF_M and MF_P at the same time by tuning the domain lengths L_i $(i = 1, 2, \ldots, M)$ successively and repeatedly. In this calculation, the initial value for each domain length is set as the same value in the periodic case $L_i = L$ $(i = 1, 2, \ldots, M)$. At the first step of calculation, only the length of the first domain L_1 is changed, and the corresponding modulation index value is calculated. By repeating the calculation with tuning the length L_1, the smallest values of MF_M and MF_P which are called the local minimizing values in this calculation step are obtained. After that, only the next domain length L_2 is tuned and the next local minimal values of MF_M and MF_P are obtained. These local minimal values are smaller than the previous ones, respectively. This calculation step with tuning the domain length is repeated by changing the domain to be tuned from the first domain to the last domain successively. When finishing the calculation step with tuning the last domain length, the domain to be tuned is set to the first domain again and these calculation steps are repeated. In these repeating calculations, the minimal values of the two flatness parameters MF_M and MF_P are obtained when the local minimal values become the same with the values in the previous calculation step, respectively. As a result, the length of each domain is optimal and the difference between the frequency responses of modulation index and the target functions becomes minimum. Therefore, it is possible to control the frequency responses of the magnitude and the phase of modulation index.

4. Calculation Results

We tried to calculate the frequency response using our method shown in the previous section. In these calculations, the attenuation coefficient α was set as negligible for simplicity. It is also possible to calculate and design the frequency response of the modulation index taking into account the attenuation coefficient [8].

Figure 3 shows examples of calculated frequency responses of the magnitude and the phase of the modulation index in the traveling-wave electrooptic modulators with nonperiodic polarization reversals for the flat, parabolic magnitude responses and linear phase responses. The number of domains was set as $M = 6$ and the frequency range was set from $f_1 = 0.7 f_m$ to $f_2 = 1.3 f_m$. The target function for the flat magnitude response was defined as $\mathrm{TF}_{M1}(f) = c_1$ (c_1 is constant, and its value is proportional to the applied modulation voltage to the electrodes), and the

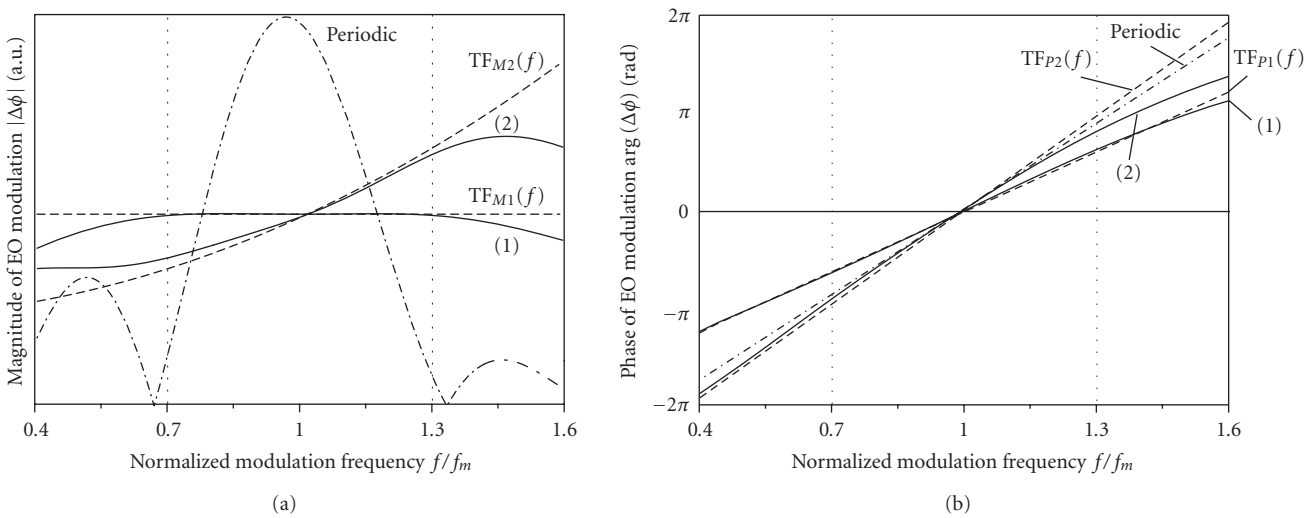

Figure 3: Frequency dependence of modulation index in traveling-wave electrooptic modulators for flat, parabolic magnitude responses with linear phase responses. (a) Magnitude responses, (b) phase responses.

Table 1: (1) Obtained normalized domain lengths for the flat magnitude response and the linear phase response, and (2) the parabolic magnitude response and the linear phase response.

	L_1/L	L_2/L	L_3/L	L_4/L	L_5/L	L_6/L
(1)	0.03	0.22	0.41	0.40	1.07	0.77
(2)	0.22	0.41	0.58	0.58	0.77	0.96

target function for the linear phase response was defined as $TF_{P1}(f) = a_1[(f/f_m) - 1]$ (a_1 is constant, and it is set as 6.5 rad in calculation). With these conditions, the calculation for minimizing the flatness parameters was carried out. The obtained frequency responses of the magnitude and the phase are shown by the curves (1) in Figures 3(a) and 3(b), respectively.

The target function for the parabolic magnitude response was also defined as $TF_{M2}(f) = c_2[(f/f_m)^2 - 1] + c_1$ (with c_2/c_1 is set as 0.6) and the target function for the linear phase response was defined as $TF_{P2}(f) = a_2[(f/f_m) - 1]$ (with a_2 is set as 10 rad). The calculation was also carried out. The obtained frequency responses of the magnitude and the phase are also shown as the curves (2) in Figures 3(a) and 3(b), respectively. For comparison, the frequency responses of the magnitude and the phase in traveling-wave electrooptic modulator with the periodic polarization reversal are also shown in the figures.

The obtained frequency responses almost coincide with the target functions in the designed frequency ranges. Table 1 shows the values of the obtained domain lengths normalized by the length L. The length L is the domain length in the periodic polarization reversal for QVM at the peak modulation frequency f_m. For example, if we set the peak modulation frequency as $f_m = 15$ GHz and the lightwave wavelength as $\lambda = 1.55$ μm, then the corresponding length of L becomes $L = 4.33$ mm for a $LiTaO_3$ guided-wave modulator (microwave phase velocity $v_m = 6.47 \times 10^7$ m/s and lightwave group velocity $v_g = 1.29 \times 10^8$ m/s).

We confirmed the validity of the proposed method. It is possible to obtain the traveling-wave electrooptic modulators with the required frequency responses of both the magnitude and the phase of the modulation index by using our new approach.

5. Applications

Recently, there are many reports related to the advanced modulation formats such as duobinary, SSB, QPSK modulation to increase the capacity of the data transmission for the new generation optical fiber communication systems. Using the control technique of the frequency responses in the electrooptic modulators with the nonperiodic polarization reversal, it is possible to design the new electrooptic modulators for the advanced modulation formats.

5.1. Electrooptic Intensity Modulator for Duobinary Modulation

The optical duobinary modulation format offers a larger capacity of data transmission and a large tolerance for fiber chromatic dispersion in optical fiber communication system [3, 10]. Several experimental studies on the generation of the optical duobinary modulation signals have been reported. In these reports, the electrical/optical filters are required to limit the spectrum bandwidth of the generated signals. By using the nonperiodically polarization-reversed structure, it is possible to obtain the electrooptic modulators with specifically tuned filter-like modulation frequency responses with any passband (low-pass, high-pass, band-pass, Gaussian like, etc.). It can be used for the generation of the duobinary modulation signals without the external electric/optic filters.

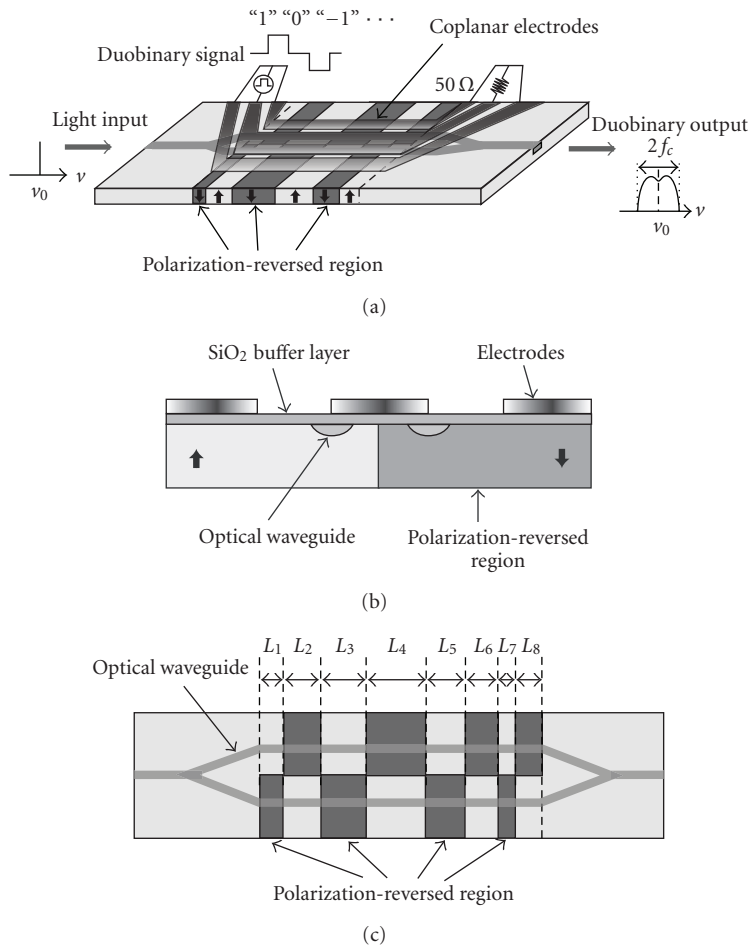

Figure 4: Basic structure of duobinary modulator with nonperiodic polarization reversal. (a) Whole view, (b) cross-section view, (c) polarization-reversed patterns.

Figure 4 shows the structure of the electrooptic intensity modulator for duobinary modulation using nonperiodic polarization reversal. It consists of the Mach-Zehnder waveguide, coplanar traveling-wave electrodes, and nonperiodically polarization-reversed structures. The lengths of each domain are the same in the two arms of the Mach-Zehnder waveguide, however, the polarity is opposite in the two arms. Therefore, by applying the electrical fields with the same direction, the push-pull intensity modulation with the same modulation index magnitude for the duobinary operation is obtained with a single modulation signal.

Using the proposed method for the frequency response control, we tried to obtain a Gaussian filter-like frequency response in the electrooptic modulation with a cutoff frequency f_c for generating the optical duobinary modulation signals. The target function for the Gaussian filter-like magnitude response was defined as $\mathrm{TF}_{\mathrm{MG}}(f) = \Delta\phi_0 \exp[-g(f/f_m)^2]$ (with g is set as 2) and the target function for the linear phase response was defined as $\mathrm{TF}_{\mathrm{PG}}(f) = a(f/f_m)$ (with a is set as 5.5 rad). The number of domains was set as $M = 8$ and the frequency range was set as the baseband from $f_1 = 0$ to $f_2 = f_m$. The obtained results are shown in Figure 5. The targets functions are shown as the dashed lines. The obtained frequency responses of the magnitude and the phase of electrooptic modulation are shown as the solid lines. Table 2 shows the obtained domain

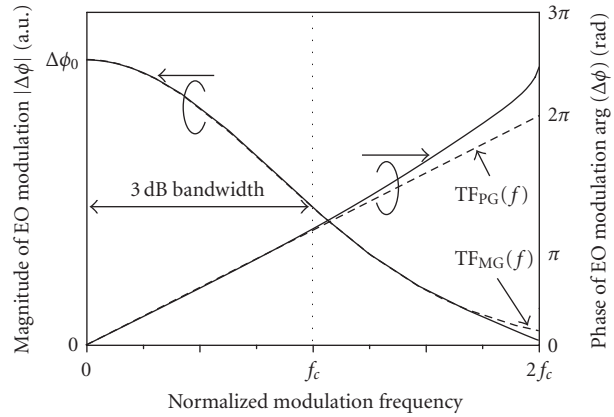

Figure 5: Frequency dependence of modulation index in traveling-wave electrooptic modulator for the Gaussian-like filter magnitude response and the linear phase response.

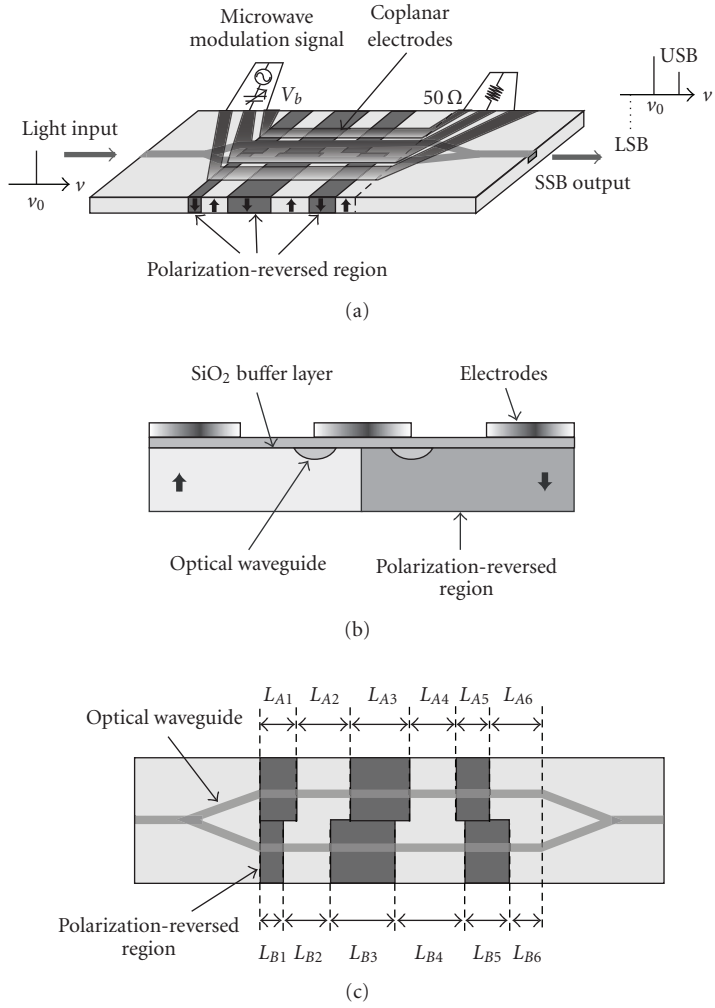

Figure 6: Basic structure of SSB modulator with nonperiodic polarization reversal. (a) Whole view, (b) cross-section view, (c) polarization-reversed patterns.

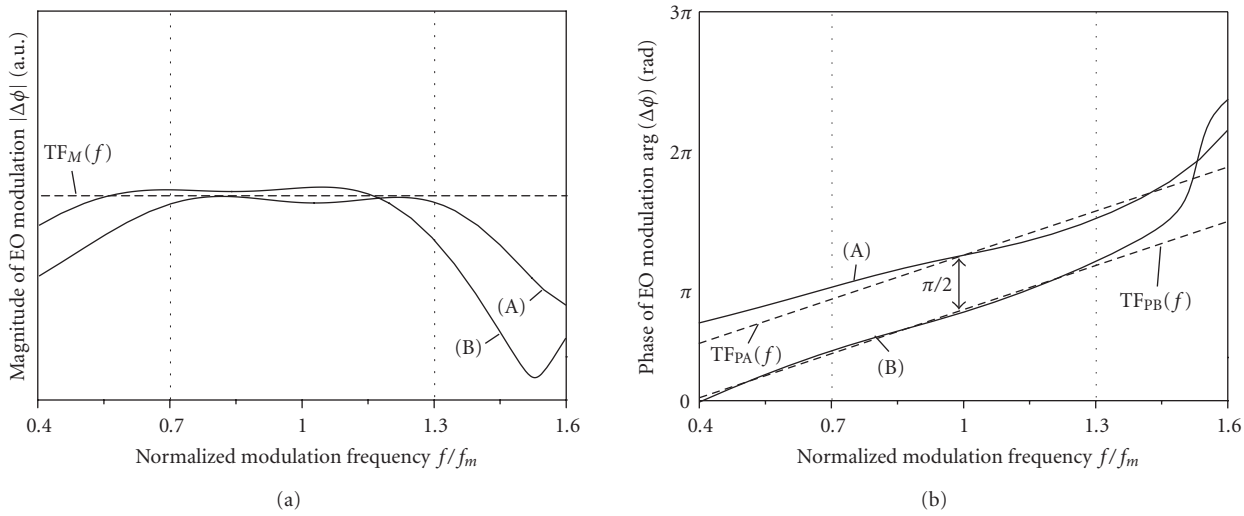

Figure 7: Frequency dependence of modulation index in designed SSB modulator for flat magnitude responses and linear phase responses with $\pi/2$ difference. (a) Magnitude responses, (b) phase responses.

Table 2: Obtained normalized domain lengths for the Gaussian-like magnitude response and the linear phase response.

L_1/L	L_2/L	L_3/L	L_4/L	L_5/L	L_6/L	L_7/L	L_8/L
0.102	0.359	0.281	1.999	0.100	0.101	0.159	0.111

lengths normalized by the periodic case length L. By using the Gaussian filter-like magnitude and the linear phase responses in electrooptic modulation, it is possible to generate the duobinary modulation signals by simple digital electrical driving signal without any filter.

We also applied the calculated polarization reversal pattern into the two arms of the Mach-Zehnder waveguide in the proposed duobinary modulator and calculated its performance. For the design of a 10 Gbps duobinary modulator, the cutoff frequency f_c was set as 5 GHz and the lightwave wavelength as $\lambda = 1.55\,\mu$m. Then, the total electrode length L_t became $L_t = 24$ mm for a $LiTaO_3$-based device.

We also checked the effect caused by the attenuation of the modulation microwave in the electrodes. We assumed a typical attenuation coefficient of the modulation microwave ($\alpha = 0.25$ dB/cm/GHz$^{0.5}$) in coplanar electrodes. As a result, the frequency response of the 10 Gbps duobinary modulator with the microwave attenuation became almost the same with the calculated one with the negligible attenuation coefficient in the frequency range from 0 to 10 GHz. Therefore, an ~10 Gbps duobinary modulator is expected using our new approach.

5.2. Broadband Single-Sideband Modulator

By using optical single-sideband modulation formats, it is possible to reduce the optical power in the signal transmission. This is attractive in long-haul optical fiber communication systems with higher density wavelength multiplexing [4]. We proposed and demonstrated the SSB modulators using the periodic polarization reversal [6]. By using our new approach, the SSB modulator with the flat and wider operational frequency range can be designed.

Figure 6 shows the structure of this electrooptic modulator using nonperiodic polarization reversal. It consists of the Mach-Zehnder waveguide, coplanar traveling-wave electrodes, and two nonperiodically polarization-reversed patterns set in the two arms of the Mach-Zehnder waveguide. In order to have the SSB modulation characteristics, it is required that the magnitudes of the modulation index are the same in the two arms of the Mach-Zehnder waveguide and the phases of the modulation index in the two arms are different as $\pi/2$ in the designed frequency range. For realizing these two modulation characteristics, we applied the control method of the frequency responses.

Figure 7 shows the calculated frequency responses for the SSB modulator with nonperiodic polarization reversal for the same target function $TF_{MA}(f) = TF_{MB}(f) = TF_M(f) = c$ (constant) and linear target functions $TF_{PA}(f) = a(f/f_m) + b$ and $TF_{PB}(f) = a(f/f_m) + b - \pi/2$ (with $a = 4$ rad, b is a common phase offset value). In this example, the number of domains was set as $M = 6$ and the frequency range was set as $f_1 = 0.7f_m$ and $f_2 = 1.3f_m$. The calculated frequency responses of the magnitude and the phase of modulation index are shown by curves (A) and (B) in Figure 7. The obtained frequency responses of the modulation index magnitudes are flat and almost the same. The obtained frequency responses of the modulation index phase are linear and have a phase difference of about $\pi/2$ in the designed frequency range. Table 3 shows the obtained domain lengths normalized by the periodic case length L.

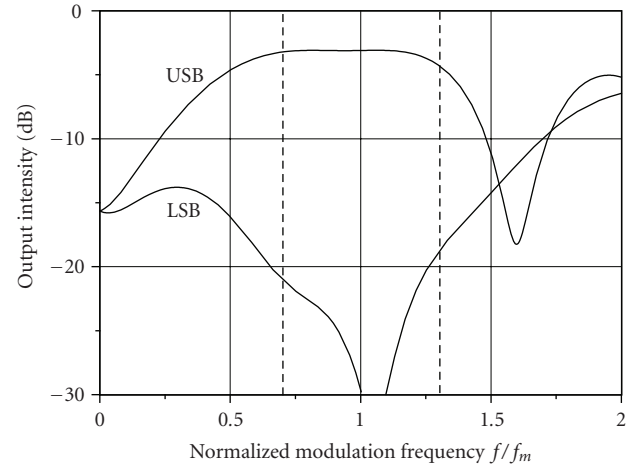

Figure 8: Frequency responses of USB and LSB components of designed SSB modulator.

Table 3: Obtained normalized domain lengths for the designed SSB modulator.

	L_1/L	L_2/L	L_3/L	L_4/L	L_5/L	L_6/L
(A)	0.65	1.31	0.58	0.51	0.48	0.28
(B)	0.19	0.96	1.42	0.45	0.51	0.24

We applied the calculated polarization reversal patterns (A) and (B) into the two arms of the Mach-Zehnder waveguide in the SSB modulator and calculated the performance of the SSB modulation. The obtained frequency dependence of the upper sideband (USB) and the lower sideband (LSB) is shown in Figure 8, where we assumed the optical delay of $\lambda/4$ in the two arms of the Mach-Zehnder waveguide by supplying an appropriate DC bias voltage to the electrodes. It is shown that the USB is generated around the designed frequency range, while the LSB is almost suppressed. The sideband suppression is expected over 20 dB around the designed frequency range. The characteristics of the USB and the LSB can be switched by changing the DC bias voltage. Therefore, the broadband SSB modulation characteristics are expected with our new approach.

6. Conclusion

We proposed the novel design of the traveling-wave electrooptic modulators using nonperiodically polarization-reversed structures to control frequency responses of both the magnitude and the phase of the modulation index. It is

possible to design advanced electrooptic modulators such as duobinary modulators or broadband SSB modulators. This approach is also applicable to design other devices such as broadband optical frequency-shift-keying (FSK) modulator, and broadband optical frequency shifter (OFS).

Acknowledgments

This work was supported in part by Grants-in-Aid for Scientific Research from the Ministry of Education, Culture, Sports, Science, and Technology of Japan. This research was also partially support by a grant from the Global COE Program, "Center for Electronic Devices Innovation," from the Ministry of Education, Culture, Sports, Science, and Technology of Japan.

References

[1] E. L. Wooten, K. M. Kissa, A. Yi-Yan, et al., "A review of lithium niobate modulators for fiber-optic communications systems," *IEEE Journal of Selected Topics in Quantum Electronics*, vol. 6, no. 1, pp. 69–82, 2000.

[2] T. Kawanishi, T. Sakamoto, and M. Izutsu, "High-speed control of lightwave amplitude, phase, and frequency by use of electrooptic effect," *IEEE Journal of Selected Topics in Quantum Electronics*, vol. 13, no. 1, pp. 79–91, 2007.

[3] K. Yonenaga and S. Kuwano, "Dispersion-tolerant optical transmission system using duobinary transmitter and binary receiver," *Journal of Lightwave Technology*, vol. 15, no. 8, pp. 1530–1537, 1997.

[4] S. Shimotsu, S. Oikawa, T. Saitou, et al., "Single side-band modulation performance of a $LiNbO_3$ integrated modulator consisting of four-phase modulator waveguides," *IEEE Photonics Technology Letters*, vol. 13, no. 4, pp. 364–366, 2001.

[5] H. Murata, K. Kinoshita, G. Miyaji, A. Morimoto, and T. Kobayashi, "Quasi-velocity-matched $LiTaO_3$ guided-wave optical phase modulator for integrated ultrashort optical pulse generators," *Electronics Letters*, vol. 36, no. 17, pp. 1459–1460, 2000.

[6] H. Murata, K. Kaneda, and Y. Okamura, "38 GHz optical single-sideband modulation by using guided-wave electrooptic modulators with periodic polarization-reversal," in *Proceedings of Conference on Lasers and Electro-Optics (CLEO '04)*, vol. 2, p. 3, San Francisco, Calif, USA, May 2004.

[7] H. Murata, T. Iwamoto, and Y. Okamura, "Novel electrooptic optical frequency shifters by use of 3-branch waveguide interferometer and polarization-reversal structures," in *Proceedings of the 9th Optoelectronics and Communications Conference (OECC '04)*, pp. 564–565, New York, NY, USA, July 2004.

[8] H. V. Pham, H. Murata, and Y. Okamura, "Travelling-wave electrooptic modulators with arbitrary frequency response utilising non-periodic polarisation reversal," *Electronics Letters*, vol. 43, no. 24, pp. 1379–1381, 2007.

[9] H. Murata, A. Morimoto, T. Kobayashi, and S. Yamamoto, "Optical pulse generation by electrooptic-modulation method and its application to integrated ultrashort pulse generators," *IEEE Journal of Selected Topics in Quantum Electronics*, vol. 6, no. 6, pp. 1325–1331, 2000.

[10] D. M. Gill, A. H. Gnauck, X. Liu, et al., "42.7-Gb/s cost-effective duobinary optical transmitter using a commercial 10-Gb/s mach-zehnder modulator with optical filtering," *IEEE Photonics Technology Letters*, vol. 17, no. 4, pp. 917–919, 2005.

Hindawi Publishing Corporation
Advances in OptoElectronics
Volume 2008, Article ID 752847, 6 pages
doi:10.1155/2008/752847

Research Article

Phase Velocity Estimation of a Microstrip Line in a Stoichiometric Periodically Domain-Inverted $LiTaO_3$ Modulator Using Electro-Optic Sampling Technique

Shintaro Hisatake, Akira Kaino, Tomoaki Yasuda, and Tadao Nagatsuma

Division of Advanced Electronics and Optical Science, Graduate School of Engineering Science, Osaka University, Toyonaka, Osaka 560-8531, Japan

Correspondence should be addressed to Shintaro Hisatake, hisatake@ee.es.osaka-u.ac.jp

Received 30 April 2008; Accepted 30 July 2008

Recommended by Chang-qing Xu

We estimate the phase velocity of a modulation microwave in a quasi-velocity-matched (QVM) electro-optic (EO) phase modulator (QVM-EOM) using EO sampling which is accurate and the most reliable technique for measuring voltage waveforms at an electrode. The substrate of the measured QVM-EOM is a stoichiometric periodically domain-inverted $LiTaO_3$ crystal. The electric field of a standing wave in a resonant microstrip line (width: 0.5 mm, height: 0.5 mm) is measured by employing a CdTe crystal as an EO sensor. The wavelength of the traveling microwave at 16.0801 GHz is determined as 3.33 mm by fitting the theoretical curve to the measured electric field distribution. The phase velocity is estimated as $v_m = 5.35 \times 10^7$ m/s, though there exists about 5% systematic error due to the perturbation by the EO sensor. Relative dielectric constant of $\epsilon_r = 41.5$ is led as the maximum likelihood value that derives the estimated phase velocity.

1. Introduction

Wide expansion of an optical spectrum by a deep phase modulation at a high-modulation frequency is the essential technique for many electro-optic (EO) light controlling fields, such as ultrashort pulse generation [1], comb generation [2], time-to-space mapping of an optical signal [3], and so on.

Quasi-velocity-matching (QVM) with periodic domain inversion of an $LiTaO_3$ (LT) or $LiNbO_3$ (LN) crystal in a traveling-wave EOM is one of the promising techniques to widely spread the optical spectrum. Especially, periodically domain-inverted stoichiometric LT (SLT) crystals are attractive QVM-EOMs because of their stronger EO effect and lower coercive fields than congruent-melt LT crystals. On the basis of the QVM technique, Morimoto et al. spread a 3-THz-wide modulation sidebands (comb) at a 16.25-GHz modulation frequency [4]. The QVM technique compensates for velocity mismatching between an optical group velocity v_g and a microwave phase velocity v_m in the EO crystal by periodically inverting the sign of the EO coefficient of the crystal. In the ideal QVM-EOM, the modulation index is almost proportional to the interaction length and as a result, large modulation index at the high modulation frequency can be achieved with long device.

Accurate values of v_g and v_m are needed in designing the QVM-EOM, because uncertainty of these values results in degradation of the modulation efficiency, which is achievable modulation index per unit interaction length per unit modulation electric field strength. The group velocity of the optical wave can be calculated with group refractive index $n_g(\lambda)$ of the EO crystal. Likewise, the phase velocity of the modulation microwave is calculated as $v_m = c/\sqrt{\epsilon_{\text{eff}}}$, where ϵ_{eff} is the effective relative dielectric constant which is determined by the geometry of the transmission line and the relative dielectric constant ϵ_r of the substrate. The group refractive index of SLT crystals is estimated accurately using Sellmeier equation with constants listed in [5]. In contrast with the accurate value of $n_g(\lambda)$, very little data of ϵ_r for

LT crystal are available, which is in the range $38.9 \le \epsilon_r \le 44.5$ at microwave frequencies [6, 7]. To our knowledge, no accurate data of ϵ_r for SLT crystals at microwave frequencies are available.

In this paper, we estimate the phase velocity of the modulation microwave in SLT-based QVM-EOM on the basis of a direct observation of an amplitude of a standing-wave in a resonant microstrip line using EO sampling technique [8]. Because the EO sampling is accurate and most reliable technique for measuring voltage waveforms at an electrode, the phase velocity can be estimated accurately from the relation of $v_m = \lambda_m f_m$, where λ_m is the wavelength of the traveling microwave and f_m is the resonant frequency. In Section 2, the principle of the QVM is summarized. Section 3 discusses influence that the estimation error of the phase velocity gives to the modulation efficiency. In Section 4, experimental results are presented.

2. Quasi-Velocity-Matching

Figures 1(a) and 1(b) show a schematic of a normal traveling-wave EOM and a QVM-EOM, respectively. To avoid unnecessary complexities, we employ a one-dimensional analysis for our devices. For a traveling-wave EOM, if the y axis is the direction in which the optical and modulation wave propagate in a virgin (single-domain) EO crystal, the variation of the refractive index induced by an electric field $E_m \sin(\omega_m t)$ is obtained at y as

$$\Delta n(y; t_0) = \Delta n_m \sin\left(\omega_m t_0 - \frac{\pi}{L_0} y\right), \tag{1}$$

where $\Delta n_m = (1/2) n_e^3 \gamma_{33} E_m$ is the amplitude of index changes, n_e is the extraordinary refractive index of the crystal, γ_{33} is the EO coefficient of the crystal, and $\omega_m = 2\pi f_m$. A half-period L_0 of the domain inversion is given by

$$L_0 = \frac{1}{2 f_m (1/v_m - 1/v_g)}, \tag{2}$$

where v_m is the phase velocity of the modulation wave, and v_g is the group velocity of the optical wave. Here, we assume that the optical wave arrives at point $y = 0$ at time $t = t_0$.

For $v_g > v_m$, the phase retardation of optical wave at the position y is expressed as

$$\theta(y; t_0) = \frac{2\pi}{\lambda} \int_0^y \Delta n(y; t_0) dy = \Delta\phi \sin\left(\omega_m t_0 - \frac{\pi}{2L_0} y\right), \tag{3}$$

where

$$\Delta\phi = \frac{4L_0}{\lambda} \Delta n_m \sin\left(\frac{\pi}{2L_0} y\right). \tag{4}$$

If there is the so-called velocity mismatching between the modulation wave and the optical wave, the modulation index $|\Delta\phi|$ becomes a periodical function of y with period $2L_0$.

When a traveling-wave EOM has a suitable domain-inverted half-period of L_0, QVM occurs and accordingly a large modulation index is achieved. In such a situation, phase retardation $\theta(l; t_0)$ given to the optical wave passing through the length of l, $qL_0 \le l < (q+1)L_0$, in a periodically domain-inverted crystal as shown in Figure 1(b) is expressed as

$$\begin{aligned} \theta(l; t_0) &= \frac{2\pi}{\lambda} \int_0^{L_0} \Delta n(y; t_0) dy - \frac{2\pi}{\lambda} \int_{L_0}^{2L_0} \Delta n(y; t_0) dy \cdots \\ &\quad + (-1)^q \frac{2\pi}{\lambda} \int_{qL_0}^{l} \Delta n(y; t_0) dy \\ &= \Delta\phi_{\mathrm{QVM}} \cos(\omega_m t_0 - \Phi). \end{aligned} \tag{5}$$

The modulation index $\Delta\phi_{\mathrm{QVM}}$ can be expressed by

$$\Delta\phi_{\mathrm{QVM}} = \begin{cases} \dfrac{4L_0 \Delta n_m}{\lambda} \sqrt{q^2 + (2q+1) \sin^2\left(\dfrac{\pi l}{2L_0}\right)} & (q : \text{even}), \\ \dfrac{4L_0 \Delta n_m}{\lambda} \sqrt{q^2 + (2q+1) \cos^2\left(\dfrac{\pi l}{2L_0}\right)} & (q : \text{odd}). \end{cases} \tag{6}$$

Figure 2 shows modulation indices of (a) the QVM-EOM, and (b) the typical traveling-wave EOM (velocity mismatching). The solid line of Figure 2(a) is calculated using (6). The modulation index achieved by QVM-EOM is almost proportional to the interaction length though it is lower than perfect velocity-matched condition by a factor of $2/\pi$. The upper limit of the modulation index for non-domain-inverted EOM is $\Delta\phi_0 = 8L_0 \Delta n_m / \lambda$.

3. Efficiency Analysis for the QVM-EOM

The analysis presented in the former section was ideal case in which there is no error in the period of the domain inversion. Uncertainties in the value of the phase velocity and group velocity degrade the modulation efficiency through the length error of the domain-inversion period for the QVM. In this section, we will discuss degradation of the modulation efficiency in the presence of length error in the period of the domain inversion.

Figure 3 show the refractive index changes seen from the optical wave in periodically domain-inverted EO crystal. The half period of the domain inversion in Figures 3(a) and 3(b) is $L = L_0$ and $L = L_0 + \Delta L$, where $\Delta L/L_0 = 10\%$, respectively. The QVM occurs in the case of Figure 3(a), and as a result the traveling optical wave of $\omega_m t_0 = 0$ sees the positive refractive index change throughout the interaction. The case of 10% error in the domain-inversion length is shown in Figure 3(b). If there is an error in length of domain inversion, the optical wave of $\omega_m t_0 = 0$ sees not only positive but also a negative refractive index change throughout the interaction.

Figure 4(a) shows the normalized modulation index calculated for the interaction length of $l = 12L_0$. The modulation efficiency almost proportionally decreases with the increase of $|\Delta L|$. The modulation efficiency decreases to about 50% in the case of $\Delta L/L_0 = 10\%$. Figure 4(b) shows the modulation index as a function of the interaction length. The calculation is carried out for the length error in the half period of the domain inversion of (i) $\Delta L/L_0 = 0\%$, (ii) $\Delta L/L_0 = 10\%$, and (iii) $\Delta L/L_0 = 15\%$. An upper limit of the modulation index exists if $\Delta L \neq 0$. Because longer

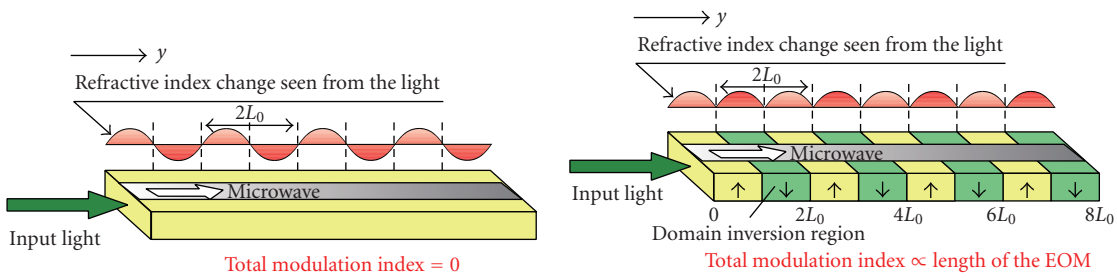

(a) Traveling-wave EOM (b) QVM-EOM

FIGURE 1: (a) Traveling-wave EOM, (b) QVM-EOM with periodic domain inversion.

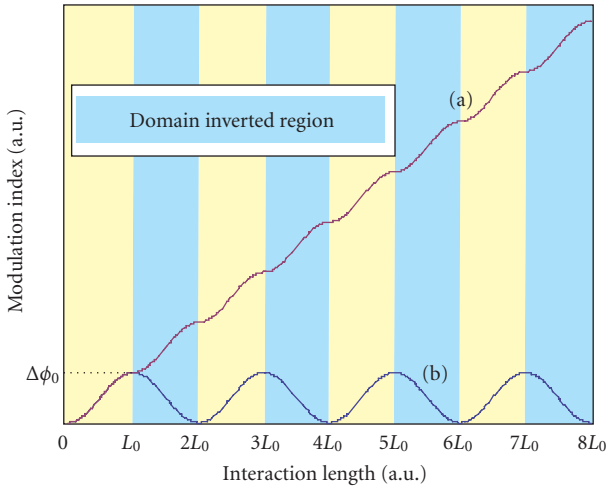

(a) Quasi-velocity-matching
(b) Velocity mismatching

FIGURE 2: Modulation indices of EOMs. (a) QVM-EOM with periodic domain inversion, and (b) typical traveling-wave EOM (velocity mismatching).

interaction length is essential for larger modulation index, it is important to estimate the length of the half period of the domain inversion in high accuracy.

Propagation of uncertainties of v_m and v_g can be evaluated by

$$\frac{\Delta L}{L_0} = \frac{v_g}{v_g - v_m}\frac{\Delta v_m}{v_m} \approx 1.8 \times \frac{\Delta v_m}{v_m},$$
$$\frac{\Delta L}{L_0} = \frac{v_m}{v_g - v_m}\frac{\Delta v_g}{v_g} \approx 0.8 \times \frac{\Delta v_g}{v_g}. \quad (7)$$

The influence on the modulation efficiency of uncertainty of v_g is lower than half of the influence on the modulation efficiency of uncertainty of v_m. Moreover, v_g can be estimated more accurately than v_m by using Sellmeier equation with constants for SLT crystal listed in [5]. Using Sellmeier equation, $n_g = 2.41$ at $\lambda = 514.5$ nm is derived. From this reliable value of n_g, the group velocity is derived as $v_g = 1.24 \times 10^8$ m/s.

The phase velocity of the modulation microwave can be calculated as $v_m = c/\sqrt{\epsilon_{\text{eff}}}$. The effective relative dielectric constant for microstrip line can be calculated using Kobayashi's formula [9, 10]. Kobayashi's formula is claimed to predict dispersion better than 0.6% in the range $1 \le \epsilon_r \le 128$ and $0.1 \le w/h \le 10$, where w and h are width and height of the microstrip line, respectively. However, uncertainty of the estimated v_m is comparatively large, because the reported value of ϵ_r for LT crystal is inaccurate and ranging $38.9 \le \epsilon_r \le 44.5$ [7]. If we employ values of $38.9 \le \epsilon_r \le 44.5$, v_m of the modulation microwave for 16.25 GHz can be calculated as 5.14×10^7 m/s $\le v_m \le 5.53 \times 10^7$ m/s using Kobayashi's formula. In that case, the half period of the domain inversion for QVM at 16.25 GHz is calculated as 2.7 mm $\le L_0 \le$ 3.1 mm with the group velocity of $v_g = 1.24 \times 10^8$ m/s. There is 14% of length uncertainty in the half period of the domain inversion. From Figure 4(b), $\Delta L/L_0 = 14\%$ results in the degradation of the modulation efficiency to about 10%.

4. Estimation of the Phase Velocity of the Modulation Wave Using EO Sampling Technique

Figure 5 shows a schematic of our QVM-EOM. An SLT crystal is used for an EO substrate. The modulation electrode structure is a microstrip line. The width of the microstrip line is $w = 0.5$ mm and the height of the substrate is $h = 0.5$ mm. The strip line is open-terminated for resonance.

Figure 6(a) shows an experimental setup. A pulsed fiber laser (repetition frequency: $f_{\text{rep}} = 40$ MHz) was used for probe pulses. The repetition frequency of the pulsed laser and the frequency of the microwave signal source are synchronized with each other. The frequency of the microwave should be set to be $f_m = N \times f_{\text{rep}} + \Delta f$, where N is an integer and Δf is an offset frequency. In the experiment, the frequency of the microwave is set to be $f_m = 16.0801$ GHz, where $N = 402$ and $\Delta f = 100$ kHz.

Figure 6(b) shows a cross-section of the microstrip line under the measurement. A CdTe crystal is used for the EO sensor. The aperture size of the EO sensor is 3 mm × 3 mm. The probe beam is focused on the CdTe crystal by the object lens (×10). The spot size is about 20 μm. The probe beam is reflected by a dielectric mirror attached to the EO

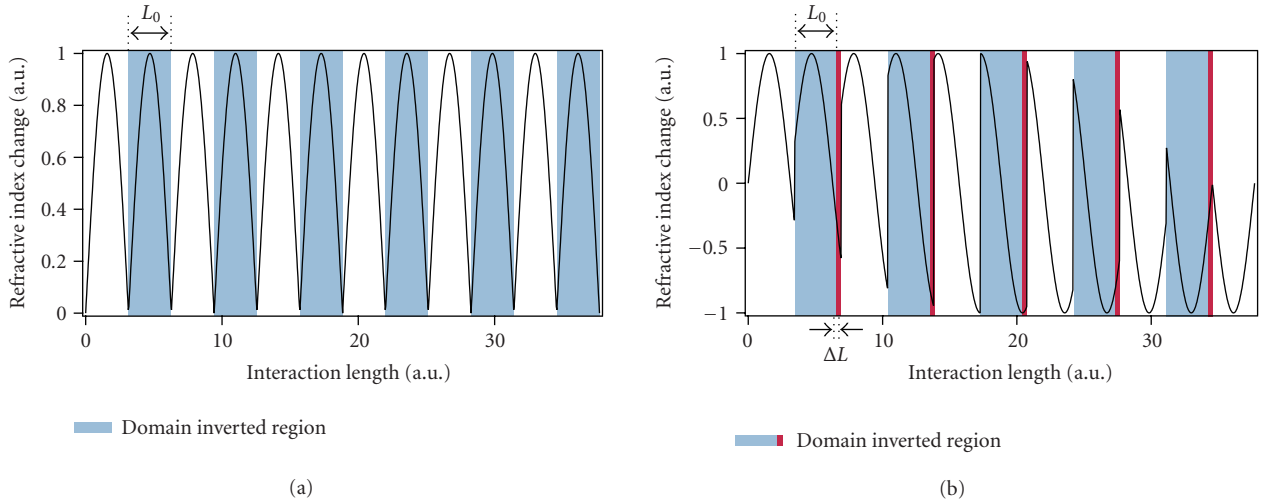

FIGURE 3: Refractive index change seen from the optical wave in periodically domain-inverted EO crystals. (a) Perfectly quasi-velocity-matched condition. Half period of the domain inversion is $L = L_0$. (b) Half period of the domain inversion is $L = L_0 + \Delta L$, where $\Delta L/L_0 = 10\%$.

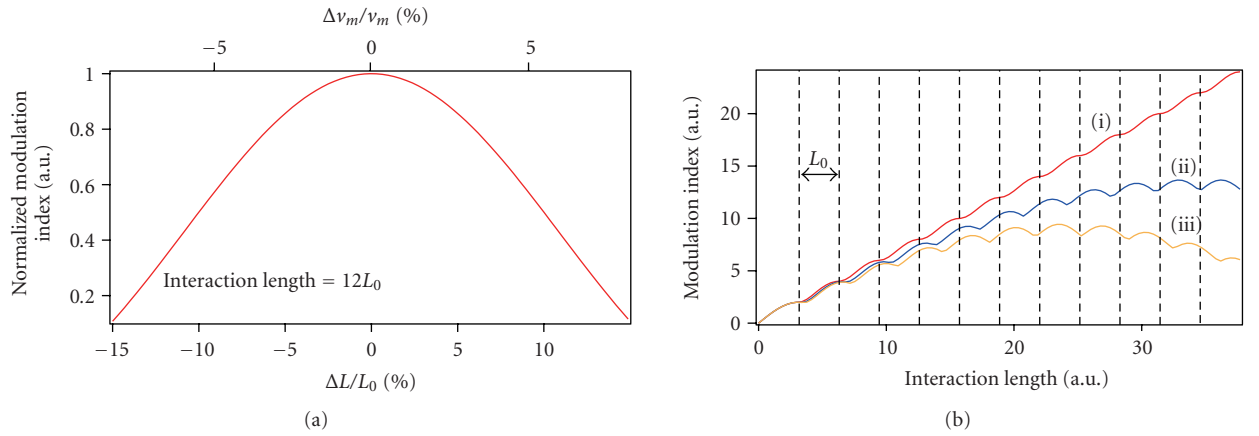

FIGURE 4: (a) Modulation index as a function of $\Delta L/L_0$. The interaction length is $12L_0$. (b) Modulation index as a function of the interaction length. (i) $\Delta L/L_0 = 0\%$, (ii) $\Delta L/L_0 = 10\%$, and (iii) $\Delta L/L_0 = 15\%$.

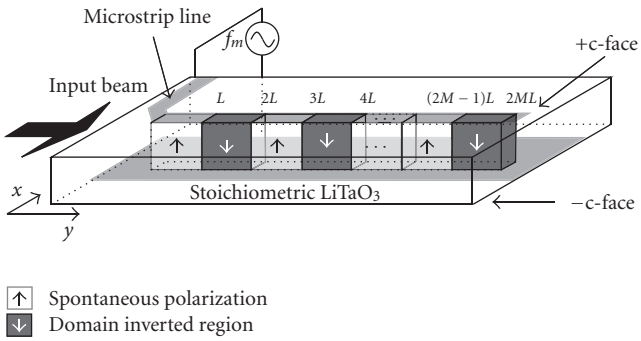

FIGURE 5: A schematic of our QVM-EOM. The substrate of the QVM-EOM is the stoichiometric $LiTaO_3$ crystal. The domain inversion is performed with the half period of L. The modulation electrode structure is the microstrip line. The width of the microstrip line is 0.5 mm. The height of the substrate is 0.5 mm.

sensor. Polarization of the reflected beam is modulated by the electric field of the microwave. The polarization-modulated beam propagates along the same path of the incident beam path. Two orthogonal polarization components of the modulated beam are differentially detected by two photodiodes. The detected signal component of $A\cos(2\pi\Delta f t + \phi)$ passes through a bandpass filter whose center frequency is 100 kHz. The amplitude of the signal, which is proportional to the amplitude of the electric field of the standing wave, is measured by a spectrum analyzer.

In the experiment, we scanned the probe beam in the y-direction with 50 μm step and measured electric field profile of the resonant standing wave. Figure 7 shows an experimental result. The theoretical curve of $a + 20\text{Log}[V(y;\gamma)]$ (solid line) is fitted to the experimental data. Fitting parameters are offset power a and $\gamma = \alpha + j\beta$. From the least square fitting, a, α, and β are estimated as $a = -64.7$ dBm, $\alpha = -0.0057$,

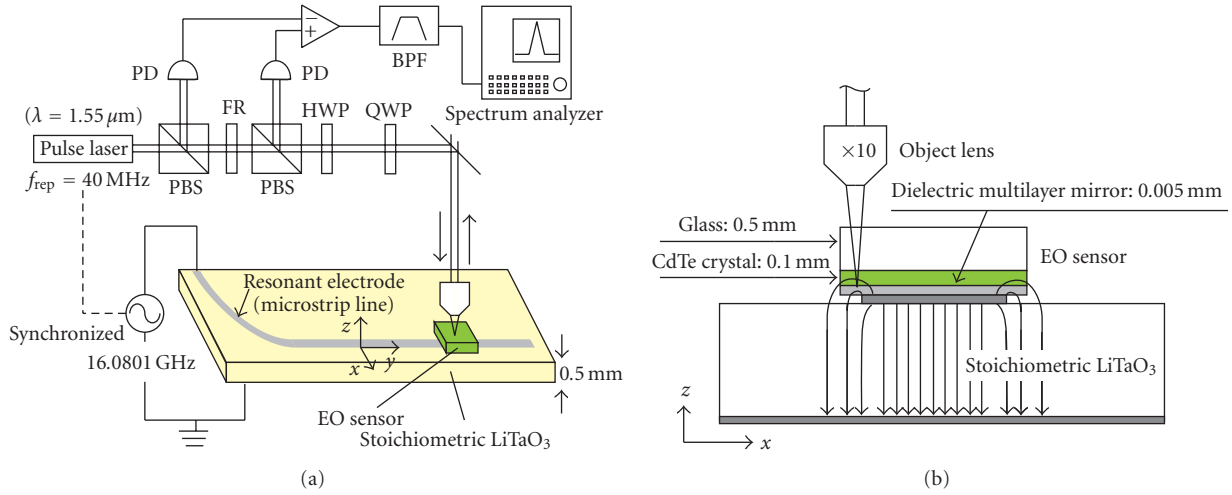

Figure 6: (a) Experimental setup. (b) Cross-section of the microstrip line under the measurement.

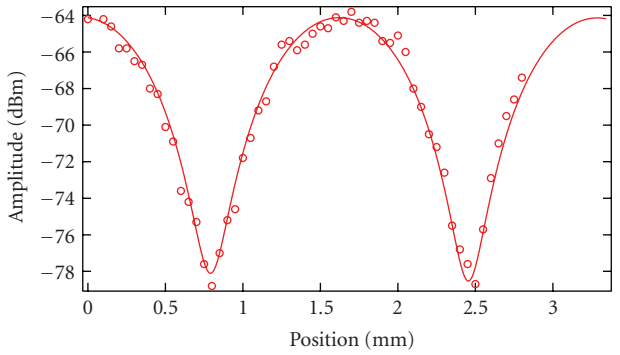

Figure 7: Magnitude of the voltage standing wave on an open-terminated microstrip line at $f_m = 16.0801$ GHz.

and $\beta = 1.888$, respectively. As a result, the wavelength of the traveling microwave is estimated as $\lambda_m = 2\pi/\beta = 3.33$ mm. The phase velocity at the modulation frequency of $f_m = 16.0801$ GHz is estimated as $f_m \times \lambda_m = 5.35 \times 10^7$ m/s. From this phase velocity, relative dielectric constant of $\epsilon_r = 41.5$ is derived using Kobayashi's formula. The half period of the domain inversion at the modulation frequency of near 16 GHz is derived as $L = 2.94$ mm with the phase velocity of $v_m = 5.35 \times 10^7$ m/s and the group velocity of 1.24×10^9 m/s.

The estimated phase velocity is slower than the real-phase velocity because of the perturbation of the EO sensor. In our case, this systematic error is estimated by numerical analysis (moment method) to be 5% or less. The 5% error in the phase velocity corresponds to the domain-inversion length error of $\Delta L/L_0 = 9\%$ which results in the degradation of the modulation efficiency to about 50%.

The systematic error depends mainly on (1) the difference of the dielectric constant between the device under test (DUT) and the EO sensor, (2) the distance between the DUT and the EO sensor, and (3) the thickness of the EO sensor. Using low-dielectric constant materials such as a polymer [11] as a sensor, the perturbation can be reduced. By loading a low-dielectric material between the DUT and the sensor to keep a distance, the perturbation can also be reduced, though the sensitivity is reduced at the same time. The use of a thinner sensor is an adequate plan to reduce the perturbation, however it also reduces the sensitivity. For a specific case, the tradeoff relationship between the perturbation strength and the sensitivity has been analyzed in the literature [12].

By using SLT substrate of the EOM as the EO sensor, it is also possible to measure the standing wave without using an external superstrate sensor [13]. In this case, special geometry should be constructed to transmit the probe beam between the microstrip line and the ground plane. This type of EOS system is now under construction and the results including the comparison with current technique will appear elsewhere.

5. Conclusion

We have estimated the phase velocity of the modulation microwave of 16 GHz in the periodically domain-inverted SLT phase modulator. The theoretical curve of the amplitude distribution of the standing wave in the microstrip line was fitted to the experimental data measured by EO sampling technique. From the curve fitting, the phase velocity of $v_m = 5.35 \times 10^7$ m/s was estimated though there is about 5% systematic error due to the perturbation by the EO sensor. Relative dielectric constant of $\epsilon_r = 41.5$ was led as the maximum likelihood value that derives the estimated phase velocity.

Acknowledgments

The authors would like to thank Drs. H. Togo and N. Kukutsu from NTT Microsystem Integration Laboratories for their cooperation and support. They also thank Dr. T. Kobayashi for helpful discussions. This research was partially supported by a grant from the Global COE Program,

"Center for Electronic Devices Innovation," from the Ministry of Education, Culture, Sports, Science, and Technology of Japan, and Grant-in-Aid for Scientific Research on Priority Areas, 19023006, 2008.

References

[1] K. Shibuya, S. Hisatake, and T. Kobayashi, "Sub-picosecond optical pulse generation with repetition rate of several tens of gigahertz using electrooptic standing-wave phase grating with periodic domain inversion," *Japanese Journal of Applied Physics*, vol. 44, no. 9A, pp. 6558–6563, 2005.

[2] S. Hisatake, Y. Nakase, K. Shibuya, and T. Kobayashi, "Generation of flat power-envelope terahertz-wide modulation sidebands from a continuous-wave laser based on an external electro-optic phase modulator," *Optics Letters*, vol. 30, no. 7, pp. 777–779, 2005.

[3] S. Hisatake and T. Kobayashi, "Time-to-space mapping of a continuous light wave with picosecond time resolution based on an electrooptic beam deflection," *Optics Express*, vol. 14, no. 26, pp. 12704–12711, 2006.

[4] A. Motimoto, M. Tamaru, Y. Matsuda, M. Arisawa, and T. Kobayashi, in *3 THz sideband generation by electro-optic modulation and the application to ultrashort pulse generation*, p. 234, Institute of Electrical and Electronics Engineers, Piscataway, NJ, USA, July 1995.

[5] M. Nakamura, S. Higuchi, S. Takekawa, K. Terabe, Y. Furukawa, and K. Kitamura, "Refractive indices in undoped and MgO-doped near-stoichiometric $LiTaO_3$ crystals," *Japanese Journal of Applied Physics*, vol. 41, no. 4, pp. L465–L467, 2002.

[6] M. V. Jacob, J. G. Hartnett, J. Mazierska, J. Krupka, and M. E. Tobar, "Lithium tantalate—a high permittivity dielectric material for microwave communication systems," in *Proceedings of IEEE Region 10 Annual International Conference on Convergent Technologies for Asia-Pacific Region (TENCON '03)*, vol. 4, pp. 1362–1366, Bangalore, India, October 2003.

[7] M. V. Jacob, J. G. Hartnett, J. Mazierska, V. Giordano, J. Krupka, and M. E. Tobar, "Temperature dependence of permittivity and loss tangent of lithium tantalate at microwave frequencies," *IEEE Transactions on Microwave Theory and Techniques*, vol. 52, no. 2, pp. 536–541, 2004.

[8] J. A. Valdmanis, G. Mourou, and C. W. Gabel, "Picosecond electro-optic sampling system," *Applied Physics Letters*, vol. 41, no. 3, pp. 211–212, 1982.

[9] M. Kobayashi and R. Terakado, "Accurately approximate formula of effective filling fraction for microstrip line with isotropic substrate and its application to the case with anisotropic substrate," *IEEE Transactions on Microwave Theory and Techniques*, vol. 27, no. 9, pp. 776–778, 1979.

[10] M. Kobayashi, "A dispersion formula satisfying recent requirements in microstrip CAD," *IEEE Transactions on Microwave Theory and Techniques*, vol. 36, no. 8, pp. 1246–1250, 1988.

[11] M. Yaita and T. Nagatsuma, "Optical sampling of electrical signals in poled polymeric media," *IEICE Transactions on Electronics*, vol. E76-C, no. 2, pp. 222–228, 1993.

[12] T. Nagatsuma, T. Shibata, E. Sano, and A. Iwata, "Subpicosecond sampling using a noncontact electro-optic probe," *Journal of Applied Physics*, vol. 66, no. 9, pp. 4001–4009, 1989.

[13] B. H. Kolner and D. M. Bloom, "Direct electro-optic sampling of transmission-line signals propagating on a gaas substrate," *Electronics Letters*, vol. 20, no. 20, pp. 818–819, 1984.

Hindawi Publishing Corporation
Advances in OptoElectronics
Volume 2008, Article ID 208458, 5 pages
doi:10.1155/2008/208458

Research Article

Domain-Reversed Lithium Niobate Single-Crystal Fibers are Potentially for Efficient Terahertz Wave Generation

Yalin Lu[1] and Kitt Reinhardt[2]

[1] *The Physics Department, Laser and Optics Research Center (LORC), 2354 Fairchild Dr. 2A31, United States Air Force Academy, CO 80840, USA*
[2] *Air Force Office of Scientific Research (AFOSR/NE), 875 North Randolph Street, Suite 326, Arlington, VA 22203, USA*

Correspondence should be addressed to Yalin Lu, yalin.lu@usafa.edu

Received 16 May 2008; Accepted 31 August 2008

Recommended by Hiroshi Murata

Nonlinear frequency conversion remains one of the dominant approaches to efficiently generate THz waves. Significant material absorption in the THz range is the main factor impeding the progress towards this direction. In this research, a new multicladding nonlinear fiber design was proposed to solve this problem, and as the major experimental effort, periodic domain structure was introduced into lithium niobate single-crystal fibers by electrical poling. The introduced periodic domain structures were nondestructively revealed using a crossly polarized optical microscope and a confocal scanning optical microscope for quality assurance.

1. Introduction

The terahertz (THz) frequency range (0.1∼30 THz) lies in the gap between microwave and infrared of the electromagnetic spectrum. THz technology lags behind both microwave and infrared technologies, mainly because of the limitations in both THz generation and detection. Development of new THz sources has been recently receiving considerable interest in many applications such as security inspection, spectroscopy, medical imaging, and sensing. The application requirements for such THz sources are versatile, and it will be reasonable to classify them according to the THz sources' compactness, frequency tunability, emission linewidth, coherence, and output power.

The most common approach used to generate THz waves is to rectify a femotosecond (fs) laser pulse using an electro-optic (EO) crystal. Efficient ultrabroad band, single-cycle THz wave generation has been realized in a few crystals such as ZnTe or GaP at a wavelength around 800 nm, under the condition of matching both optical and THz pulses' group velocities [1]. Tradeoff for this approach is that the majority of such EO crystals have strong material dispersion, which limits the output wave's bandwidth and power. On the other extreme, continuous-wave (cw) THz generation has been realized in free-electron lasers and quantum cascade lasers. The former offers high output power, but they are bulky and inflexible. The latter, however, provides the potential for good system compactness, high efficiency, and suitable frequency tunability, but with very limited output power availability and short wavelength coverage.

Using periodically poled nonlinear optical crystals for efficient THz generation is becoming an alternative approach. Conventional techniques such as difference frequency generation (DFG), which uses two laser sources (either nanosecond-pulsed or cw), are attractive in inducing coherent THz waves with a suitable frequency tunability. Phase matching among the three interactive waves (two optical and one THz) can be realized by artificially introducing reversed domain structures (so-called quasiphase matching (QPM) method if periodically or quasiperiodically poled [2]). Unfortunately, such techniques' generation efficiency is low due to the strong absorption of THz waves in those commonly used nonlinear crystals such as $LiNbO_3$(LN), $KTiOPO_4$ (KTP) [3].

Optical rectification of fs laser pulses using artificially poled nonlinear optical crystals is used to generate multicycle

or arbitrary wave forms [4]. When an fs optical pulse propagates through a poled lithium niobate (PLN) crystal with its second-order nonlinear susceptibility ($\chi^{(2)}$) reversing its sign between neighboring domains, a THz nonlinear polarization is generated via DFG or optical rectification. Due to the group velocity mismatch between optical and THz waves, the optical pulse will lead the THz by the optical pulse duration τ_p after a walkoff length $l_w = c\tau_p/(n_{\mathrm{THz}} - n_{\mathrm{optical}})$. If the domain length of the poled nonlinear crystal is comparable to the walk-off length, each domain in the crystal contributes a half cycle to the radiated THz field. Similar to the above DFG approach, in this case, high material absorption to THz waves will be still the major reason for the poor generation efficiency. Apparently, either a significant improvement on the material's transparency over those THz wavelengths or a new device design able to significantly minimize the THz absorption issue will be pressingly in demand in order to bring such devices to the more practical side of the potential THz applications.

In this article, a new device design relying on the multicladding nonlinear fiber format (MCNF) will be discussed for potential efficient THz generation application. This design has the potential to solve the nonlinear material's absorption issue over those generated THz waves, and it maintains the high conversion efficiency that a strongly confined optical fiber may provide. To realize such new multicladding fiber designs, efficient fabrication of the poled nonlinear optical fibers will be the first and major step, and this will be discussed with details in Section 3 after introducing the device design. In Section 4, those reversed domain structures are nondestructively revealed by both crossly polarized optical microscope (CPOM) and confocal scanning optical microscope (CSOM).

2. The Multicore Nonlinear Fiber Design

Figure 1 shows the schematic of the multicladding nonlinear fiber. The main core inside the design can be a domain-inverted lithium niobate single-crystal fiber (1), while the first (2), the second (3), and the third (4) claddings can be made from the polyamide matrix materials with their refractive indices changed by certain dopants. The refractive index requirements for such designs are as follows: for the optical wave, $n_{\mathrm{O1}} > n_{\mathrm{O2}}$, n_{O3}, and n_{O4}; and for the THz wave, $n_{\mathrm{T3}} > n_{\mathrm{T2}}$ and $n_{\mathrm{T3}} > n_{\mathrm{T4}}$. In this case, the pumping optical wave will be confined inside the main core (1), and the generated THz wave will be coupled into and propagates in cladding 3. Geometrically, cladding 2 should be thin, which should allow the generated THz wave losslessly side-emitted into cladding 3. In the THz frequency range, LN crystal has a refractive index around 5.5, and that of those polyamide materials is normally around 2.1. For the two materials in optical frequencies, their refractive indices are around 2.2 and 1.4, respectively. Apparently, the use of such MCNF design has the potential to fully eliminate the nonlinear optical material absorption issue discussed before by separating the generated THz beam from the optical beam into a different path of propagation. Those cladding materials to be selected, such as the polyamide materials discussed here, should be highly transparent for a wide THz frequency range.

The energy and the momentum conversion laws for generating the THz frequencies via the DFG, for example, can be described as

$$\begin{aligned} E_{\omega 1} &= E_{\omega 2} + E_{\omega \mathrm{THz}}, \\ \vec{K}_{\omega 1} &= \vec{K}_{\omega 2} + \vec{K}_{\omega \mathrm{THz}} + \vec{K}_{\Lambda}, \end{aligned} \tag{1}$$

where E is the photon energy, K is the wave vector at each frequency, and K_Λ is the grating's reciprocal vector. The generated THz frequency can be then determined by

$$\omega_{\mathrm{THz}} = \frac{c}{\Lambda} \cdot \frac{1}{|n_{\mathrm{O}} - n_{\mathrm{THz}} \cdot \sin\Phi|}, \tag{2}$$

where Λ is the domain-poled period, n_{O} and n_{THz} are refractive indices for optical and THz waves, respectively, and Φ is the internal direction of the generated THz emission, which will be a key parameter when designing the device for realizing efficient coupling of the generated THz wave from the main core into cladding 3, as shown in Figure 2 before.

Figure 3 shows the calculated dependence of forward and backward THz frequencies on the poled domain periods (Λ) when using lithium niobate single crystals. Listed K_p, K_s, and K_{THz} are wave vectors for the pump (ω_1), the signal (ω_2), and the generated THz wave, respectively. Aside each curve, schematic of the corresponding wave-vector diagram is also shown. Inset inside Figure 3 shows a relationship of THz frequency versus the internal emission angle (Φ) at a fixed poling period around 50 μm using the $LiNbO_3$ crystal. Combining with the general waveguide theories of optical fibers, simulation results obtained here can be further used to design the device including both material selection and the dimensional determination of claddings and the main core. However, this is a separate research effort that will be published in somewhere else. In the following sections, we mainly report the fabrication of a periodically poled $LiNbO_3$ single-crystal fiber, which is the key to further make the MCNF device.

3. Poling the LN Single-Crystal Fiber

The *a*-axis-oriented LN single-crystal fibers having cross-section dimensions ranging from 100 μm to 130 μm and lengths from 10 mm to 50 mm were grown using the LHPG method [5]. Normally, an *a*-axis LN single-crystal fiber has an elliptical cross-section with two ridges as shown in Figure 4(a). Its *c*-axis orientation is determined along the short axis of the ellipse and the *b*-axis along its long axis. This natural configuration makes it convenient to use contacting electrodes to electrically pole the fiber, simply for the reason that the applied electric field is required to be aligned parallel to the *c*-axis (the polarization direction). During the poling, the fiber is placed on top of a copper block and a gold grating is slightly pressed onto the fiber. The gold grating, which has the predetermined structures, was made on a Φ2" sapphire wafer using a standard photolithographic process (Figure 4(b)). Listed d_1 and d_2 inside the inset are

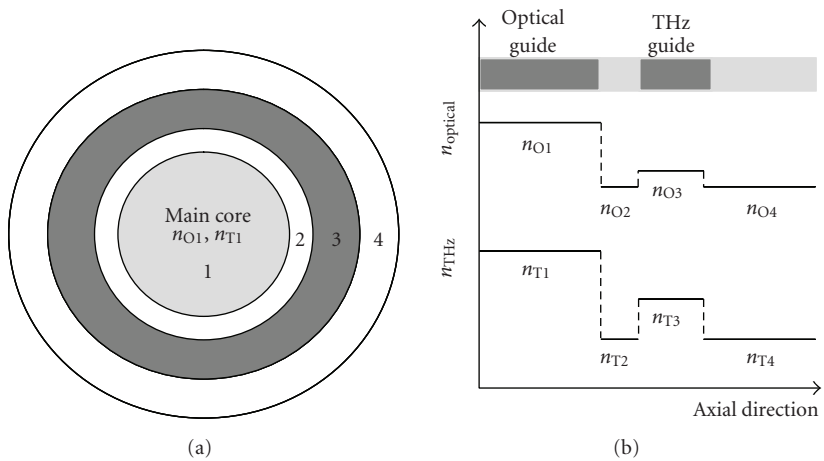

Figure 1: Schematic of the multicladding nonlinear fiber design. (a): the cross-section view, and (b): the axial index profile.

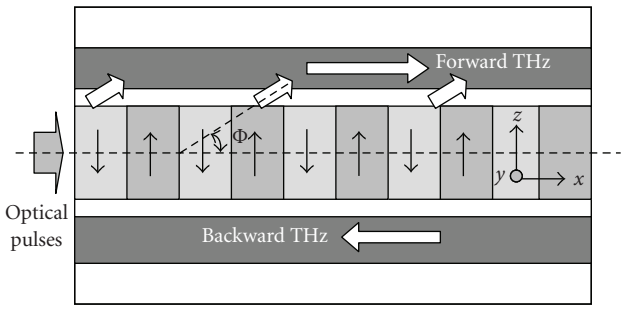

Figure 2: Schematic of the domain-reversed nonlinear core, the generated THz wave coupling, and both forward and backward propagation THz waves.

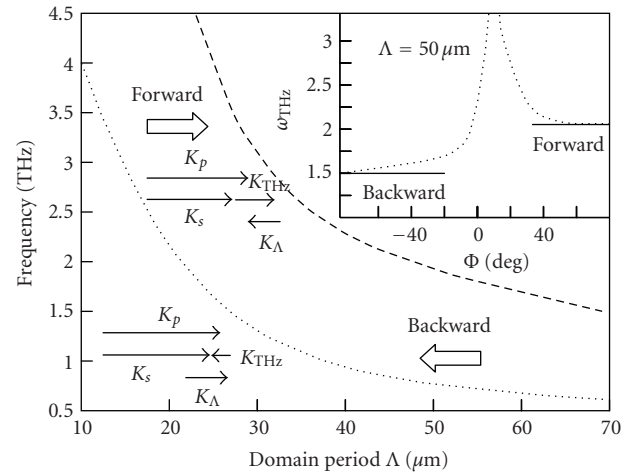

Figure 3: The generated THz frequency versus the domain period in $LiNbO_3$ crystal for both forward and backward propagation schemes. K_p, K_s, K_{THz}, K_Λ, are wave vectors for the pump (ω_1), the signal (ω_2), the generated THz wave, and the reciprocal vector of the grating, respectively. Inset shows the relationship between the generated THz frequency and the internal emission angle (this angle is to be used for further coupling the THz wave out from the main core).

gold electrode widths, which are changeable by designing, in order to adjust the poled domain period duty cycle. The copper block and gold grating are connected to each polarity of a high-voltage power supply. LN crystals have a coercive field approximately 22 kV/mm. For an LN fiber with a dimension of 120 μm along the c-axis, the applied voltage should be close to 4 kV. In our experiments, special measures such as filling with Teflon coatings were taken to prevent the breakdown of air, simply because of the short electrode space and high voltage (this is different from puling bulk crystal wafers). Most as-grown single-crystal fibers present a single-domain structure. However, it is difficult to discriminate between the $+c$ or $-c$ surfaces without using destructive methods such as wet etching. In our case, simply switching the applied electrical field's polarity and observing the sudden current change during poling can find the right polarization arrangement.

Periodic domain structure inside the LN fiber was then revealed using both a crossly polarized optical microscope (CPOM) and a confocal scanning optical microscope (CSOM) [6]. The main reason to use the two methods is because of their nature of being nondestructive to samples under the measurement. When using the CPOM, the poled LN fiber was simply put between a crossly polarized light. The method can disclose periodic domains in a relatively larger view field. Because of this, in this research the CPOM was mainly used to evaluate both completeness and uniformity of the periodic domains along the length of the fiber, characteristics that can be regarded as the poling quality at macroscale level. The CSOM, on the other hand, provides a means for measuring the electro-optic response to a small *ac* electrical field modulation. With the use of lock-in amplification, the sensitivity of this method can be greatly enhanced, allowing one to obtain high-contrast ferroelectric images using a relatively small *ac* field. The linear relationship between the electro-optic coefficient and the ferroelectric polarization allows this technique to work

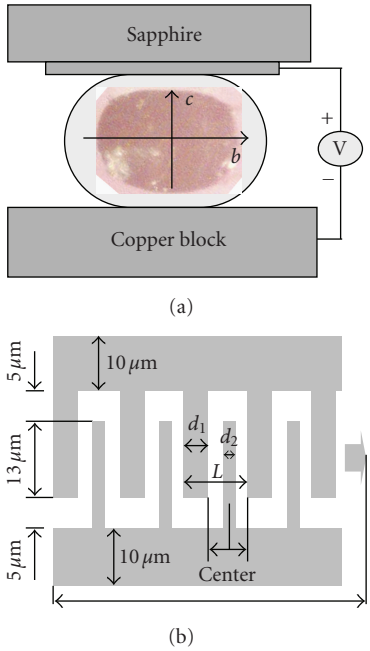

Figure 4: (a) The poling setup used for poling *a*-axis-grown lithium niobate single-crystal fiber (inset: the fiber's elliptic cross-section image). (b) One design of the top interdigital electrode. d_1 and d_2 inside the inset are gold electrodes' width, which are changeable by design in order to adjust the poled domain period duty cycle.

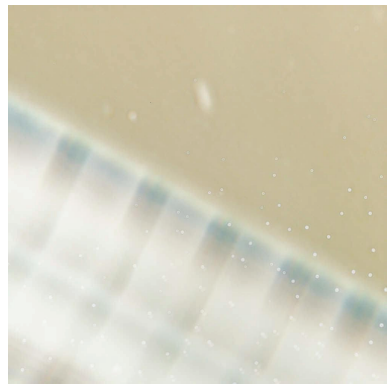

Figure 5: The periodic domains inside a 17 mm long LN single-crystal fiber revealed by a crossly polarized optical microscope.

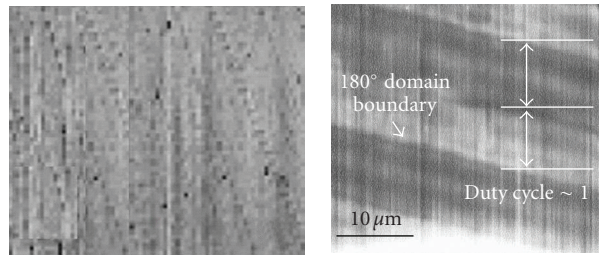

Figure 6: The confocal scanning optical microscope images under both *dc*-mode (a) and *ac*-mode (b). Uniformity of the period duty cycle across the fiber length is good.

over a broad range of field amplitudes, frequencies, and orientations of electric field, ferroelectric axis, and light polarization. The CSOM method was used because of its capability to nondestructively study the LN single-crystal fibers and to disclose the domain structure details including domain boundary or period duty circle inside the fibers, characteristics that can be regarded as the poling quality at the microscale level.

In the CSOM, a 632.0 nm HeNe laser is used as a light source. The beam then passes a linear polarizer and half-wave plate which provides a capability to select the beam's polarization direction. The light is focused to a diffraction-limited spot using a high NA objective. The fiber was mounted on a three-dimensional piezoelectric scanner. In the measurement, the LN fiber was tightly clamped by two silver-coated copper plates as electrodes. The soft silver coating was used for reaching better electric contact. The LN fiber was aligned with its *b*-axis normal to the plates. The *ac* voltage was applied onto the two electrodes variable from 0–100 V, and, therefore, the *ac* field can vary between $0 \sim 7$ kV/cm.

Figure 5 shows an image of the periodically poled ferroelectric domains inside the LN single-crystal fiber under a crossly polarized optical microscope. The periodicity of the structure was measured to be roughly 20 μm, which is very close to the designed value for further generating 2.5 THz wavelength. A typically scanned image of linearly polarized light reflected from the LN fiber's surface is shown in Figure 6(a). This is actually an optical image when observed using a conventional optical microscope. The stripes and dark dots are due to surface defects and possible surface contaminations. Using this operational mode, ferroelectric domains or boundaries are invisible. In Figure 5(b), a simultaneously acquired image of the *ac* field-modulated signal is presented. The dark and bright areas represent ferroelectric domains having $+c$ and $-c$ polarizations. The observed domain boundaries are thin and sharp, and are below the resolution of the CSOM. The image confirms the periodicity of ~20 μm and a period duty circle of about 1 : 1. Uniformity of the period duty cycle across the fiber length was examined to be quite good.

4. Conclusion

A new multicladding nonlinear fiber design was proposed to generate THz waves with the potential of reaching high efficiency. Inside the design, the main core of the fiber will be a domain-reversed nonlinear crystal such as periodically poled LN crystal and the multiple claddings are from those THz transparent materials such as polyamides. This design has the potential to reduce the common material absorption issue over the THz frequency and keeps the high efficiency when using the fiber format. As one of the major experimental efforts, periodic ferroelectric domain structures were successfully introduced into lithium niobate single-crystal fibers. The poling completeness and domain

uniformity were examined by using a crossly polarized optical microscope. The periodic domains' boundary and period duty circle were examined by a confocal scanning optical microscope.

References

[1] Q. Wu and X.-C. Zhang, "Ultrafast electro-optic field sensors," *Applied Physics Letters*, vol. 68, no. 12, pp. 1604–1606, 1996.

[2] Y.-L. Lu, L. Mao, S.-D. Cheng, N.-B. Ming, and Y.-T. Lu, "Second-harmonic generation of blue light in $LiNbO_3$ crystal with periodic ferroelectric domain structures," *Applied Physics Letters*, vol. 59, no. 5, pp. 516–518, 1991.

[3] R. Guo, K. Akiyama, H. Minamide, and H. Ito, "All-solid-state, narrow linewidth, wavelength-agile terahertz-wave generator," *Applied Physics Letters*, vol. 88, no. 9, Article ID 091120, 3 pages, 2006.

[4] Y.-S. Lee, T. Meade, V. Perlin, H. Winful, T. B. Norris, and A. Galvanauskas, "Generation of narrow-band terahertz radiation via optical rectification of femtosecond pulses in periodically poled lithium niobate," *Applied Physics Letters*, vol. 76, no. 18, pp. 2505–2507, 2000.

[5] M. M. Fejer, J. L. Nightingale, G. A. Magel, and R. L. Byer, "Laser-heated miniature pedestal growth apparatus for single-crystal optical fibers," *Review of Scientific Instruments*, vol. 55, no. 11, pp. 1791–1796, 1984.

[6] C. Hubert and J. Levy, "Nanometer-scale imaging of domains in ferroelectric thin films using apertureless near-field scanning optical microscopy," *Applied Physics Letters*, vol. 73, no. 22, pp. 3229–3231, 1998.

Hindawi Publishing Corporation
Advances in OptoElectronics
Volume 2008, Article ID 948614, 4 pages
doi:10.1155/2008/948614

Research Article

Negative Refraction Using Frequency-Tuned Oxide Multilayer Structure

Yalin Lu,[1] Gail J. Brown,[2] and Kitt Reinhardt[3]

[1] *Laser and Optics Research Center (LORC), Department of Physics, U.S. Air Force Academy, CO 80840, USA*
[2] *AFRL/ RXPSO, Wright-Patterson Air Force Base, Building 651, 3005 Hobson Way, OH 45433, USA*
[3] *AFOSR/NE, Suite 326, 875 North Randolph Street, Arlington, VA 22203, USA*

Correspondence should be addressed to Yalin Lu, yalin.lu@usafa.edu

Received 14 May 2008; Accepted 31 August 2008

Recommended by Hiroshi Murata

An oxide-based multilayer structure was proposed to realize negative refraction. The multilayer composes of alternative layers having negative permittivity and negative permeability, respectively. In order to realize negative refraction, their dielectric and magnetic resonances of layers will be tuned to the frequency as close as possibly via changing their temperature, composition, structure, and so forth. Such oxide-based NIMs are attractive for their potential applications as optical super lenses, imagers, optical cloaking, sensors, and so forth, those are required with low-loss, low-cost, and good fabrication flexibility.

1. Introduction

Negative index materials (NIMs) have attracted extensive attention in recent years since the first observation of negative refraction in those artificially made metamaterials consisting of arrays of metallic rings/rods [1]. Majority of such NIMs use metallic split ring resonance (SRR), surface plasmonic resonance, or a combination of magnetic and metallic materials with naturally occurring negative permeability (μ) or negative permittivity (ε). Very unique properties of such metamaterials, including negative refraction, have been previously demonstrated mainly for operation in microwave frequencies. A new trend of current NIM research is toward the optical frequency. For example, a lossless negative index slab material could act as a "superlens" or a "perfect lens," which could image object with a high resolution far below the conventional optical diffraction limit, and are attractive to those applications including data storage, medical imaging, biophysics, and so forth. In addition to those metamaterials, negative refraction has also been found in other material formats including planar transmission lines, photonic crystals, and so forth. However, all such NIMs use complicated artificial structures requiring high-precision nanofabrication and can hardly be rigorously considered as uniform materials, since the size of their structural elements is usually greater than one tenth of the operation wavelength. In addition, certain polarization and incident angle of an electromagnetic (EM) field must be maintained in order to realize such negative refraction.

Considering the fact that an SRR in a metamaterial produces $-\varepsilon\psi$ and $-\mu\psi$, respectively [2], such a metamaterial will be similar to a multilayer composed by alternating $-\varepsilon\psi$ and $-\mu\psi$ layers—the later will be much easier to realize as a natural material. It is also well known that some natural materials have inherent $-\varepsilon\psi$ or $-\mu$, which will be useful for multilayer NIM fabrications. For example, certain ferrites have $-\mu$ in microwave frequencies, and many conducting materials have $-\varepsilon$ below the plasma frequency. Studies toward this direction have been performed, mostly by simulations, in stacked ferrite-dielectric waveguides, ferrite-metal, ferromagnetic-superconductor, and ferrite-semiconductor multilayers [3]. However, the use of conductive materials may excite surface waves at their interfaces, which in turn change their electromagnetic characters, and more seriously, result in a significant high-loss concern. Apparently, an NIM composing of nonconductive optical materials will be promising.

Availability of the frequency tunability to an optical NIM will provide a much bigger freedom in exploring its potential applications as sensors, modulators, switches, and

so forth. Variable electromagnetic response when changing a metamaterial's structure is not a practical way of frequency tuning. External tuning via filling liquid crystals and photoconductive materials to metamaterials will work for some frequencies. It is normally slow and has concern on both reliability and stability of performances.

This manuscript intends to discuss one possible mechanism potential able to realize negative refraction using all oxide-base materials in the format of multilayer. Such oxide-based negative index multilayers are expected to potentially have low optical losses, against to those existing designs using conductive materials, and are potentially frequency-tunable if the NIM's composing materials are dielectrically tunable by external fields including electric, optical, and microwave. Tunable dielectrics are easily realizable in many piezoelectric and piezomagnetic complex oxides. Therefore, the impact of such NIMs to their potential applications such as super lenses, optical cloaking, optoelectronics, and sensing can be significant.

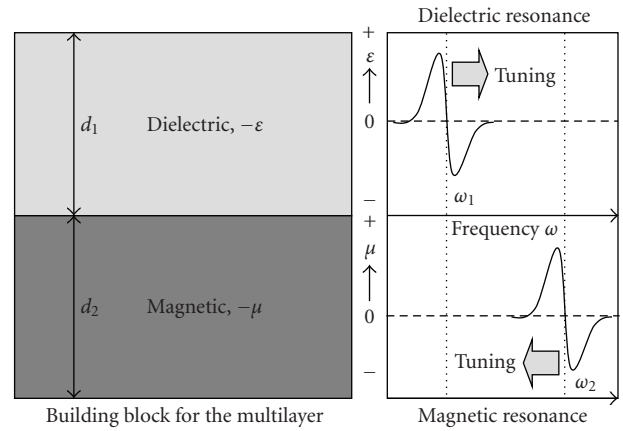

Figure 1: Schematic of a negative permittivity and negative permeability double layer (the building block for multilayer, the left side of the figure) and tuning of their resonance frequencies to concurrence-occur to the same frequency (inset at the right side).

2. Oxide Multilayer NIMs

The mechanism to build the oxide multilayer NIM to be discussed is a resonance-tuned multilayer (RTM) composing of alternative dielectric and magnetic oxide layers having naturally occurring $-\varepsilon\psi$ or $-\mu$, respectively, and having their resonance frequencies finely tuned to concurrence via both structural and compositional engineering to both used materials.

The RTM mechanism considers the nonlattice-matched multilayer case and the two alternative oxide layers as the multilayer have $-\mu$ or $-\varepsilon$, respectively. For example, the oxide multilayer can be represented as $(A/B)_m$, and "A" has an intrinsic dielectric resonance, and "B" represents a material with an intrinsic magnetic resonance. The RTM approach will be used to fine-tune the two resonance frequencies concurrence together, and realize the negative refraction immediately after the merged resonance frequency. Fine-tuning to each oxide material can be realized by changing composition, structure, temperature, magnetic field, and so forth. Schematic of the RTM NIM is shown in Figure 1. In Figure 1, only two adjacent laminas (one dielectric and the other magnetic) having thickness of d_1 and d_2, respectively, are shown. They will be the building block for further making into the multilayer structure. The insets on the right side schematically show the frequency spectra of both permittivity and permeability around the resonance frequencies. Arrows indicate the directions of frequency tuning to make two resonance frequencies concurrence. Figure 2 shows the schematic multilayer structure and the concurrence-occurred frequency spectra showing the frequency region with both negative permittivity and negative permeability.

In order to achieve a concurrence of both dielectric and magnetic resonances in dielectric and magnetic oxide materials, different origins of dielectric and magnetic responses have to be considered for different frequencies ranging from the UV/visible, far-infrared (including the major terahertz band), to microwave. For the UV to visible spectrum, for example, the dielectric response is primarily from the electronic polarization modes and the magnetic response from the magnetic dipoles. In the far-IR range, ionic polarization modes, and antiferromagnetic resonances (AFMRs) are mainly responsible for dielectric and magnetic responses, respectively. Similarly, for those microwave frequencies, electronic dipole reorientation (domain wall moving) and ferromagnetic resonances (FMRs) are the main causes.

Other than the resonance frequency of the concerning materials, both degree of damping and amplitude of dielectric and magnetic responses will also play the key rule. For example, in optical frequencies, direct magnetic dipole response is orders of magnitude weaker than electronic dipole response. The above-discussed SCS mechanism actually provides an indirect coupling of the magnetic dipole response to a strong electronic dipole resonance via the phonon resonance, yielding both negative permeability and negative permittivity after the phonon resonance frequency.

The dielectric dispersion due to the electronic dipole polarization can be fitted to the following empirical expression:

$$\frac{\varepsilon^*(\omega)-\varepsilon_{\infty 1}}{\varepsilon_0-\varepsilon_{\infty 1}}=\sum_{i=1}^{n} g_i\left[\frac{1}{(1+i\omega\tau_i)}\right], \tag{1}$$

where $\varepsilon_{\infty 1}$ is the permittivity due to the ionic polarization, ε_0 is the low-frequency permittivity, ω is the angular frequency, and g_i is the distribution of relaxation time (τ_i). On the other hand, the dielectric dispersion due to the ionic polarization can be fitted to the following four-parameter semiquantum model [4]:

$$\varepsilon^*(\omega)=\varepsilon_{\infty 2}\prod_{j=1}^{n}\frac{\omega_{j\mathrm{LO}}^2-\omega^2+i\gamma_{j\mathrm{LO}}\omega}{\omega_{j\mathrm{TO}}^2-\omega^2+i\gamma_{j\mathrm{TO}}\omega}, \tag{2}$$

where $\varepsilon_{\infty 2}$ is the permittivity due to the electronic polarization, n is the number of optical phonon mode, γ is the damping factor, and TO and LO represent transverse

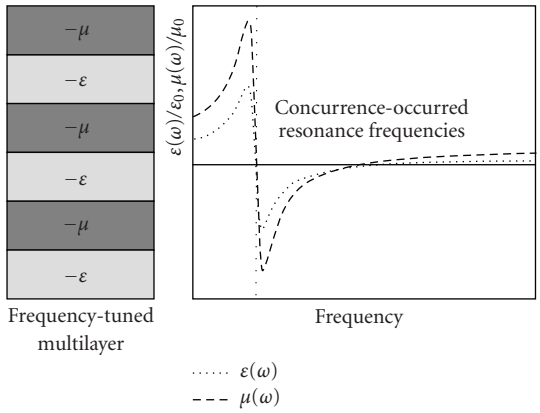

Figure 2: Schematic of the frequency-tuned multilayer structure (left) and the concurrence-occurred resonances on both permittivity and permeability (right). After the concurrence-occurred resonance frequency, both negative permittivity and negative permeability will occur, which indicates negative optical refraction.

and longitudinal optical phonon modes, respectively. The relationship between the ε^* and IR reflectivity $R(\omega)$ can be given by

$$R(\omega) = \left| \frac{(\sqrt{\varepsilon^*(\omega)} - 1)}{(\sqrt{\varepsilon^*(\omega)} + 1)} \right|. \tag{3}$$

Equations (1), (2), and (3) permit a direct identification of the dielectric spectra and resonance frequencies via the experimental IR reflectivity measurement on a specific dielectric material system. Contribution from domain wall relaxation is usually masked by electronic and ionic relaxations, unless the temperature is close to the material's Curie temperature or phase transition temperature. It has been usually reported at above 100 kHz frequencies, will be minor to those optical frequencies of our current discussion interest.

Magnetic resonances can be identified from recording the complex permeability spectra on those magnetic oxide materials of interests. Accordingly, the complex permeability can be expressed as a superposition of two contributions, $\mu(\omega) = 1 + \tilde{\chi}_{\mathrm{dw}}(\omega) + \tilde{\chi}_{\mathrm{rot}}(\omega)$, namely, the domain wall component $\tilde{\chi}_{\mathrm{dw}}(\omega)$ and the magnetic moment rotation $\tilde{\chi}_{\mathrm{rot}}(\omega)$:

$$\begin{aligned} \tilde{\chi}_{\mathrm{dw}}(\omega) &= \frac{\chi_{\mathrm{dw}}\omega_{\mathrm{dw}}^2}{\omega_{\mathrm{dw}}^2 - \omega^2 + j(\beta/m_{\mathrm{dw}})\omega}, \\ \tilde{\chi}_{\mathrm{rot}} &= \frac{(\omega_{\mathrm{rot}} + j\alpha\omega)\chi_{\mathrm{rot}}\omega_{\mathrm{rot}}}{(\omega_{\mathrm{rot}} + j\alpha\omega)^2 - \omega^2}, \end{aligned} \tag{4}$$

where χ_{dw} and χ_{rot} are static (or low frequency) susceptibilities for domain wall (DW) and magnetic moment rotation (ROT) motions, ω_{dw} and ω_{rot} are resonance frequencies of DW and ROT components, β and α are corresponding damping factors, m_{dw} is the effective mass of wall, and ω is the frequency of the driving *ac* magnetic field. Description of magnetic moment motions will be highly dependent on materials. For simplicity, we consider both AFMR and FMR cases which will be similar in theory.

In a magnetic material having a uniaxial anisotropy and the magnetic field is applied parallel to the easy axis, the AFMR frequency ω_{AFMR} at low temperature (below Néel temperature) is given by

$$\begin{aligned} \frac{2\pi\omega_{\mathrm{AFMR}}}{\gamma} &= \sqrt{2H_E H_A} \pm H, \quad (H < H_{\mathrm{SF}}), \\ \frac{2\pi\omega_{\mathrm{AFMR}}}{\gamma} &= \sqrt{H^2 - 2H_E H_A}, \quad (H > H_{\mathrm{SF}}), \end{aligned} \tag{5}$$

where $\gamma(\equiv g\mu_B/\hbar)$ is the magnetomechanical ratio, H_E is the exchange field, H_A is the anisotropy field, and H_{SF} is the spin-flop field. When H is applied perpendicular to the easy axis, then the ω_{AFMR} is given by

$$\frac{2\pi\omega_{\mathrm{AFMR}}}{\gamma} = \sqrt{H^2 + 2H_E H_A}. \tag{6}$$

For FMR, a simple expression about the ω_{FMR} is Kittel's equation

$$\frac{\omega_{\mathrm{FMR}}}{\gamma} = \sqrt{(H_{A,\mathrm{eff}} + H_E)4\pi M_s}, \tag{7}$$

where $H_{A,\mathrm{eff}}$ is the effective anisotropy field, and $4\pi M_s$ the saturation magnetization. For both AFMR and FMR cases and when for qualitative analyses, it can be simplified to $\omega \propto \sqrt{H_A H_E}$.

Depending on the material selection for such multilayer, the above equations provide the way to measure their resonance frequencies via a variety of approaches including optical reflection, time-domain terahertz (THz) transmission, magnetic analysis, and so forth. The above equations also theoretically provide the direction to realize the efficient frequency tuning in order to achieve concurrence of both dielectric and magnetic resonance frequencies.

3. Frequency Tuning

Tuning both dielectric and magnetic resonance frequencies may follow a few different ways. In certain ferroelectric materials, optical mode of the lattice (phonon) is dependent on both temperature (T) and the material's Curie temperature (T_c), roughly following an empirical relation: $\omega^2 \propto (T - T_c)$ as an example. As an example, Figure 3 shows the dependence of relative dielectric constant on the composition. The dielectric maximum occurs at $x_{\mathrm{Ba}} \sim 0.7$ [at where the ferroelectric-paraelectric boundary (FPB) occurs], and it Curie temperature changes from 415 K ($x_{\mathrm{Ba}} \sim 1$) to about 40 K ($x_{\mathrm{Ba}} \sim 0$) almost linearly [5]. Similarly, tuning by changing both temperature and material composition is also applicable to some magnetic oxide materials. Inset in Figure 2 show a general frequency tuning schematic via changing the temperature, in order to reach a concurrence at the same frequency for both dielectric and magnetic resonances. Apparently, tuning their compositions to reach a room temperature operation of the NIMs will be the most attractive, simply because of the practicability for applications.

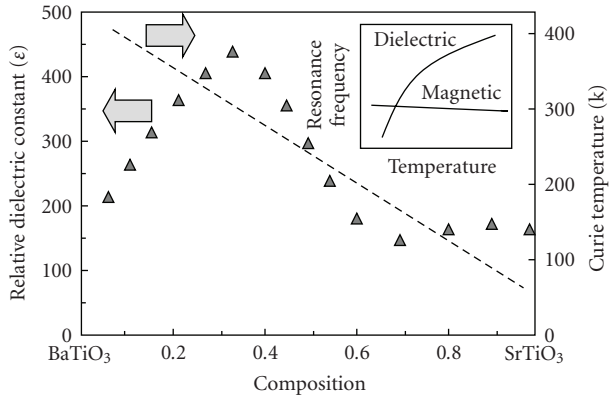

Figure 3: Dependence of the dielectric constant and Curie temperature of $(Ba,Sr)TiO_3$ on its composition. Inset shows a possible frequency tuning by changing the temperature for reaching the concurrence of both dielectric and magnetic resonance frequencies.

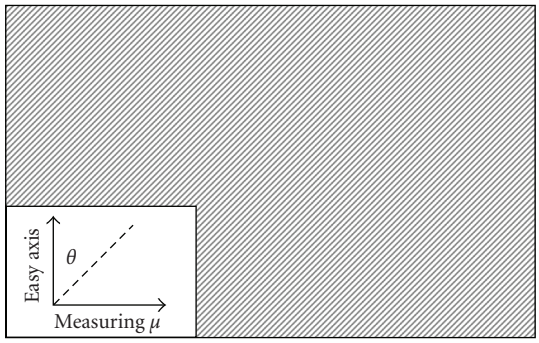

Figure 4: Schematic of the multilayer structure alignment required for possibly tuning the FMR resonance frequency via changing the structural parameters—width, period, duty cycle, and the orientation angle.

An alternative way of possibly tuning the magnetic resonance frequency is by changing the magnetic layer's alignment inside the multilayer structure. Figure 4 shows the schematic of such a structure in which the FMR frequency will be tuned by changing either the orientation angle θ or the layer thickness, following the rewritten Kittel's formula involving both uniaxial anisotropy field (H_u) and the additional shape anisotropy field ($H_{k,\text{eff}}$) into the total effective anisotropy field ($H_{A,\text{eff}}$)

$$H_{A,\text{eff}} = H_u + H_{k,\text{eff}} \cos\theta,$$
$$\frac{2\pi\omega_{\text{AFMR}}}{\gamma} = \sqrt{4\pi M_s H_{A,\text{eff}}}. \tag{8}$$

In Figure 4, the main picture shows the parallel strait structure to be made in the magnetic layer inside the superlattice, via selective etching the as-fabricated magnetic layer or mask-shielding growth, and so forth. The inset shows that when one measures the permeability horizontally, the result will be actually tunable by changing the strait's size (both period and width) or by changing the angle respective to the easy axis of the magnetic material. The multilayer structure itself to be discussed in this theory actually provides the great easiness to reach such frequency tuning for the magnetic part inside the multilayer. Structural parameters that can be varied when designing include the layer thickness, periodic duty cycle, and magnetic orientation, and so forth. An efficient way to optimize material compositions and structural parameters may follow the combinatorial strategy [6]. Effort toward efficient material selection, simulation for frequency tuning, and the multilayer fabrication is ongoing and will be published separately.

4. Conclusion

One possible physical mechanism toward realizing negative refraction in a fully oxide-based multilayer was theoretically discussed. Inside the multilayer structure, such negative refraction may be achieved by tuning their resonances to the same frequency via changing temperature, layer composition, structural parameter, and so forth. Such oxide-based NIMs are attractive for their potential applications as optical super lenses, imagers, sensors, and so forth, that are potential with low-loss, cost-effectiveness, and good fabrication flexibility.

References

[1] R. A. Shelby, D. R. Smith, and S. Schultz, "Experimental verification of a negative index of refraction," *Science*, vol. 292, no. 5514, pp. 77–79, 2001.

[2] D. R. Smith, S. Schultz, P. Markoš, and C. M. Soukoulis, "Determination of effective permittivity and permeability of metamaterials from reflection and transmission coefficients," *Physical Review B*, vol. 65, no. 19, Article ID 195104, 5 pages, 2002.

[3] R. H. Tarkanyan and D. G. Niarchos, "Effective negative refractive index in ferromagnet-semiconductor superlattices," *Optics Express*, vol. 14, no. 12, pp. 5433–5444, 2006.

[4] F. Gervais, "High-temperature infrared reflectivity spectroscopy by scanning interferometry," in *Infrared and Millimeter Waves*, K. J. Button, Ed., vol. 8, pp. 279–339, Academic Press, New York, NY, USA, 1983.

[5] J. Li, F. Duewer, C. Gao, H. Chang, X.-D. Xiang, and Y. Lu, "Electro-optic measurements of the ferroelectric-paraelectric boundary in $Ba_{1-x}Sr_xTiO_3$ materials chips," *Applied Physics Letters*, vol. 76, no. 6, pp. 769–771, 2000.

[6] Y. Lu, "The structural engineering strategy for photonic material research and device development," *Active and Passive Electronic Components*, vol. 2007, Article ID 17692, 7 pages, 2007.